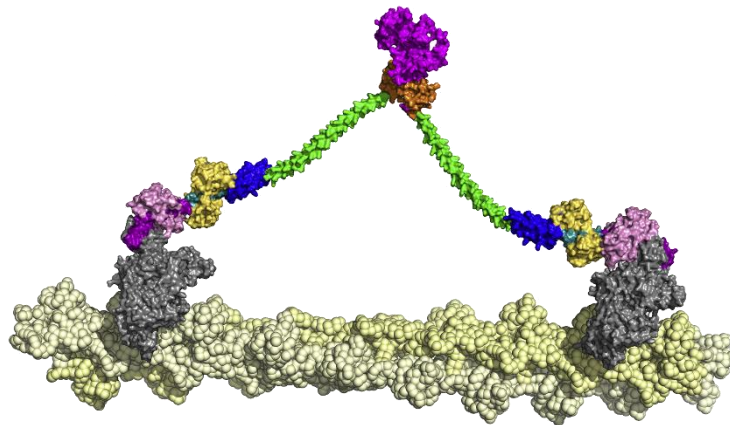


Dissertation

Investigating the functions of myosin VI in
genome stability and ageing



attaining the academic degree

Doctor rerum naturalium



Johannes Gutenberg-Universität Mainz



submitted by Kristine Hauschulte

Mainz, 15.07.2023

Investigating the functions of myosin VI in
genome stability and ageing

Dissertation

Institute of Molecular Biology
Group of Helle Ulrich

attaining the academic degree
Doctor rerum naturalium

Johannes Gutenberg-Universität Mainz

submitted by Kristine Hauschulte
born 14.08.1997 in Eupen, Belgium
matriculation number: 2726179

Mainz, 15.07.2023

Dean: Prof. Dr. Eckhard Thines

1. Examiner: [REDACTED]

2. Examiner: [REDACTED]

Table of Contents

Table of Contents

Acknowledgements	III
Table of Contents	V
Abstract	IX
Zusammenfassung	X
1. Introduction	1
1.1 Myosins	1
1.1.1 Myosin VI	3
1.1.2 Nuclear Myosin VI	5
1.2 Genome stability	6
1.3 Replication stress response	6
1.4 Double strand break repair	6
1.4.1 Repair pathway choice	7
1.4.2 Non Homologous End Joining	9
1.4.1 Homology directed Repair	9
1.4.2 Drugs to investigate on DSBs	12
1.5 F-Actin involvement in DSB repair	12
1.6 Biological consequences	13
1.6.1 Senescence	14
1.7 Previous research	17
2. Materials & Methods	19
2.1 Equipment & Material	19
2.2 Computer programs	19
2.3 Reagents	19
2.3.1 Chemicals	19
2.3.2 Antibodies	21
2.3.3 siRNAs	22

Table of Contents

2.3.4	Plasmids	22
2.4	Media and buffer solutions.....	23
2.5	Mammalian cell lines	23
2.6	Mammalian cell culture.....	24
2.6.1	Cell passaging, counting and harvesting.....	24
2.7	Treatments.....	24
2.8	Transfections	24
2.8.1	Lipofectamine RNAiMAX.....	24
2.8.2	PEI transfection.....	25
2.8.3	Cell lysis and Bradford assay.....	25
2.9	Colony Formation Assay.....	25
2.10	Immunofluorescence staining	26
2.11	Senescence staining (β -Gal, p16, p21).....	26
2.12	β -Gal Quantification.....	26
2.13	β -Gal staining	27
2.14	Resection Assay	27
2.15	Flow Cytometry for cell cycle characterization	27
2.16	Generation of stable cell lines	27
2.17	SDS-Gel and Western Blotting	28
2.18	Chromatin bound protein pre-extraction.....	28
2.19	Microscopy imaging.....	28
2.19.1	Image processing with FIJI	29
2.20	Statistical Analysis	30
3.	Results	31
3.1	Characterization of Myo6 in Homology Directed Repair.....	31
3.2	Confirmation of RPA phenotype due to Myo6 loss.....	35
3.3	RPA phenotype upon actin polymerization inhibition.....	36
3.4	Cell cycle analysis.....	38

Table of Contents

3.4.1	Myo6 KO show no cell cycle slow down upon DNA damage	38
3.4.2	Tracking CPT damaged cells to the next cell cycle phase	39
3.5	Degradation Systems for Myo6.....	41
3.5.1	Single cell clone characterization for 2-RING system.....	41
3.5.2	Single cell clone characterization for SPOP system	44
3.5.3	Nuclear vs Cytoplasmic Myo6 (SPOP, 2-RING, NLS).....	46
3.6	Further characterization of Myo6 role in HDR.....	49
3.6.1	Myo6 role in chromatin remodeling.....	49
3.6.2	Myo6 role in KU70/80 removal	50
3.7	KU70/80 staining optimization	51
3.8	Myo6 involvement in KU70/80 removal	54
3.9	Biological consequences in form of Senescence.....	56
3.9.1	Generation of inducible Myo6 depletion stable cell lines.....	56
3.9.2	Characterization of senescence markers upon Myo6 depletion	56
3.9.3	Characterization of damage marker upon Myo6 depletion.....	58
4.	Discussion	61
4.1	Myo6 depletion results in a survival defect	61
4.2	Myo6-depleted cells show less cell cycle slow down upon DNA damage	62
4.3	Myo6 characterisation in HDR	62
4.4	Myo6's role in HDR.....	64
4.5	Myo6's role in replication stress	66
4.6	Myo6's role in senescence	67
4.7	Summary and Outlook	69
5.	List of Tables.....	73
6.	List of Figures	73
7.	Abbreviations	74
8.	Eigenständigkeitserklärung	77
9.	References	79

Table of Contents

10.	Appendix	87
10.1	Supplementary figures.....	87
10.2	Shi <i>et al.</i> , Nature Communications (2023).....	95

Abstract

The cytoskeleton is crucial for cell mechanics and intracellular transport. It consists of filamentous-actin (F-actin), microtubules, and intermediate filaments. Moving along F-actin, myosins act as molecular motors and are responsible for short distance cargo transport of e.g., proteins, vesicles, and organelles. Even though this interplay, between F-actin and myosins, is well studied in the cytoplasm, its functions are poorly understood in the context of nuclear biology. Recent publications revealed an involvement of F-actin in double strand break (DSB) repair, more specifically in the homology-directed repair (HDR) pathway. Similarly, first evidence for a role of a myosin (Myo6) in the HDR pathway in human cells was shown in my master thesis. Impairment of DSB repair can lead to DNA damage-induced senescence or even cell death. Therefore, the aim of this work is to gain a functional understanding of Myo6 in the HDR of DSBs.

Immunofluorescence (IF)-based microscopy assays were employed to characterize the recruitment of key marker proteins of the HDR and general DNA damage response (DDR) to chromatin in a Myo6 depletion background in human cells. Knockout or knockdown of Myo6 resulted in a reduction of HDR marker presence on chromatin, whereas DDR was unaffected upon DNA damage. The entire HDR cascade was affected, up to and including impairment of KU80 removal from chromatin. Survival defects shown in Myo6 depleted cells and cell cycle analysis by flow cytometry complemented the analysis and highlight the importance of Myo6 for survival and cell cycle slowdown after DNA damage. Various Myo6 degradation approaches were utilized to investigate whether nuclear or cytoplasmic Myo6 is responsible for the observed defects. Thus, it was demonstrated that the nuclear pool was responsible for the HDR defects. Finally, the induction of senescence after Myo6 depletion was investigated using senescence marker proteins in an imaging-based assay. In primary cell lines, Myo6 depletion resulted in an accumulation of DSBs and an increase of β -galactosidase activity, which is a hallmark of senescence.

Overall, this study revealed that Myo6, a molecular motor acting on F-actin, is involved in one of the major DSB repair pathways, HDR. It likely promotes removal of KU70/80 from chromatin. In addition and as a biological consequence of the DSB repair defect, an accumulation of DNA damage and a senescence-like phenotype was observed in primary cell lines. Taken together, the results of this study provide first insight into the mechanisms of Myo6 and nuclear F-actin in HDR-mediated DSB repair. This work is therefore right in the centre of an emerging field of research into the role of cytoskeletal proteins in nuclear biology and how these could be exploited as new targets in drug discovery.

Zusammenfassung

Das Zytoskelett ist von zentraler Bedeutung für die Zellmechanik und den intrazellulären Transport. Es besteht aus filamentösem Aktin (F-Aktin), Mikrotubuli und Intermediärfilamenten. Myosine, die sich entlang des F-Aktins fortbewegen, fungieren als molekulare Motoren und sind für den Kurzstreckentransport von z. B. Proteinen, Vesikeln und Organellen verantwortlich. Obwohl dieses Zusammenspiel zwischen F-Aktin und Myosinen im Zytoplasma gut untersucht ist, sind seine Funktionen im Zellkern nur wenig bekannt. Aktuelle Veröffentlichungen demonstrieren, dass F-Aktin an der Reparatur von Doppelstrangbrüchen (DSB) beteiligt ist, genauer gesagt an der homologen Rekombination (HR). Zudem wurden in meiner Masterarbeit erste Beweise für die Rolle eines Myosins (Myo6) im HR-Prozess in menschlichen Zellen erbracht. Eine Beeinträchtigung der DSB-Reparatur kann zu einer durch DNA-Schäden induzierten Seneszenz oder sogar zum Zelltod führen. Ziel dieser Arbeit ist es daher, ein funktionelles Verständnis von Myo6 in der HR von DSB zu erlangen.

Immunfluoreszenz (IF)-basierte Mikroskopie-Assays wurden eingesetzt, um die Rekrutierung von HR- und der generellen DNA-Schadensreaktion (DDR)-Markerproteinen zum Chromatin in einem Myo6-Depletionshintergrund zu charakterisieren. *Knockout* oder *Knockdown* von Myo6 führte zu einer Verringerung von HR-Markern am Chromatin, während die DDR bei DNA-Schäden unbeeinflusst blieb. Die gesamte HR-Kaskade war betroffen, bis hin zur Beeinträchtigung der KU80-Ablösung vom Chromatin. Überlebensdefekte in Myo6-depletierten Zellen und Zellzyklusanalysen mittels Durchflusszytometrie ergänzten die Analyse und unterstrichen die Bedeutung von Myo6 für das Überleben nach DNA-Schäden. Mittels verschiedener Depletierungsansätze von Myo6 konnte gezeigt werden, dass der nukleäre Pool für die HR-Defekte verantwortlich ist und nicht der zytoplasmatische. Schließlich wurde die Induktion von Seneszenz nach der Deletion von Myo6 mit Hilfe von Seneszenzmarkerproteinen untersucht. In primären Zelllinien führte die Deletion von Myo6 zu einer Anhäufung von DSB und einem Anstieg der β -Galaktosidase-Aktivität, was ein Merkmal der Seneszenz ist.

Zusammengefasst zeigt diese Studie, dass Myo6, ein F-Aktin basierter molekularer Motor an einem der wichtigsten DSB-Reparaturwege, der HR, beteiligt ist. Er fördert vermutlich die Ablösung von KU70/80 vom Chromatin. Zusätzlich und als biologische Folge des DSB-Reparaturdefekts wurde in primären Zelllinien eine Anhäufung von DNA-Schäden und ein seneszenzähnlicher Phänotyp beobachtet. Insgesamt geben die Ergebnisse dieser Studie einen ersten Einblick in die Mechanismen von Myo6 und nukleärem F-Aktin bei der HR-vermittelten DSB-Reparatur. Diese Arbeit steht daher im Mittelpunkt eines neuen Forschungsgebiets, das sich mit der Rolle von Zytoskelettproteinen in der Kernbiologie befasst und mit der Frage, wie diese als neue Ziele bei der Entwicklung von Medikamenten genutzt werden könnten.

1. Introduction

The Cytoskeleton is a three dimensional, highly structured and at the same time dynamic network. It is involved in processes such as cell division, force transmission, intra-cellular transport, endocytosis and many others. This functionally versatile structure consists mainly out of three classical cytoskeletal filament types: microtubules, actin filaments (F-Actin) and intermediate filaments¹. Kinesin, dynein and myosins act as molecular motors on the filaments and are thus involved in long- and short-distance transport. Microtubules serve as a track for kinesin and dynein, while myosins move on F-actin.

1.1 Myosins

Myosins are actin based mechanoenzymes and are also described as actin-activated Mg^{2+} ATPase². According to variations in amino acid sequence of the motor domain, there are 18 classes of myosins encoded by 40 genes in the human genome³. All myosins show three common domains: the N-terminal motor domain, the neck domain or lever arm and the tail domain. The N-terminal design allows myosins to function as motor proteins on F-actin or as monomeric non-processive anchors, fixing other proteins to chromatin or F-actin⁴⁻⁶.

Myosins are further divided into two groups. The conventional myosins (which were discovered first) and the unconventional myosins^{5,7,8}. Conventional myosins form bipolar thick filaments that are essential for muscle and cytokine contraction. They contain a long coiled-coil domain to perform tail-directed multimerisation⁷. This group includes all muscle-related myosins and non-muscle myosin II. In contrast, the other two-thirds of myosin genes in humans encode for unconventional myosins. They are important for intracellular trafficking, adhesion, mobility of the cell and more^{5,8}. In the following, the focus is on the unconventional myosins.

To perform their functions, the N-terminal domain contains an actin-binding site, a nucleotide-binding site and an ATP-binding site. While movement, the association and the dissociation of myosin on F-actin leads to conformational changes. This process is driven by the ATPase cycle⁹. When ATP or ADP are bound to the catalytic domain, myosins show a low affinity for actin. With the release of P_i , the affinity increases (Figure 1). This P_i release, associated with the converter rotation, is the basis of all movement along F-actin. Attached to the motor domain is the neck domain. It is needed to convert the conformational changes in the motor domain into power-stroke motions. The name lever arm derives from its function as a lever that rotates or tilts, thereby amplifying the force. By the length of the lever arm the step size of the myosin is defined¹⁰. Additionally, the lever arm includes IQ motifs for calmodulin or calmodulin-like

Introduction

protein binding. The last of the three common domains is the c-terminal tail domain. In this domain, there are substantial differences between the various myosins in terms of their specific binding sites for different cargoes. There can be direct interaction with cargo or indirect interaction via adaptor proteins¹¹. Another special characteristic is that myosins can be single-headed or two-headed. However, they usually form a coiled coil of two myosin heavy-chain α -helices. Through this linkage, some myosins are able to move in a “hand over hand” manner along F-actin (Figure 1).

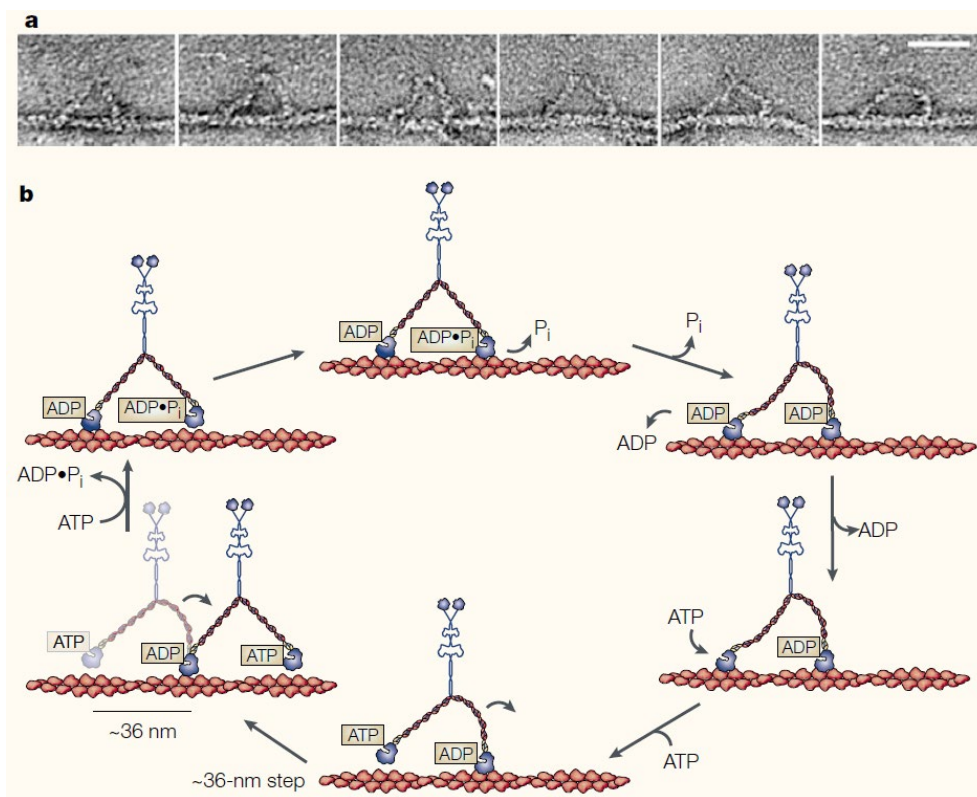


Figure 1: Processive stepping of myosin V along actin filament

(a) Electron micrograph images of myosin V bound to the actin filament. Scale bar: 36 nm (b) Model for myosin V stepping. Upon P_i and ADP release, affinity of myosin towards actin decreases and one motor domain detaches from actin. Upon ATP binding the motor domain has a high affinity towards actin and attaches again. Adapted from Spudich, 2001¹²

Introduction

Myosins are involved in many critical processes in the cell such as migration, cell expansion, endocytosis, cell division, force transmission and more¹¹. It is therefore not surprising that human diseases are related to mutations in myosins. One example is Griscelli syndrome, characterized by defects in pigmentation and neuronal malfunction and is associated with mutations in the *Myo5a* gene¹³. Another example is a mutation in *Myo5b* gene associated with microvillus inclusion disease, an impairment in transport of apical endosomes in brush border cells. Myosin dysfunction is also associated with hypertrophic cardiomyopathy. However, the best known syndrome related with myosin mutations is Usher syndrome. It results in genetic deaf-blindness and is associated with mutations in myosin Ia, IIc, IIIa, VI, VIIa and XV^{7,14}. Many of these diseases are caused by a problem in transporting proteins to their correct location¹⁴. For their transport function, myosins require F-actin, along which they move. Monomeric actin can form filaments, which are then used by myosin as a track. These filaments have a barbed or a plus end and a pointed or minus end where the filament assembles or disassembles¹⁵. All classes of myosin move toward the plus end of F-actin. With the exception of myosin VI, which has a special orientation and moves toward the minus end. This unique orientation suggests that myosin VI may also have unique functions in the cell.

1.1.1 Myosin VI

Myosin VI, like all myosins, consists of a motor domain, the lever arm and the tail domain (Figure 2). The unique orientation of myosin VI (*Myo6*) is due to the so-called reverse gear (or insert 2 domain), which is connected to the N-terminal motor domain^{16,17}. This insert 2 is a 53 amino acid sequence that directs the effective lever arm toward the minus end of F-actin. It also contains a calmodulin-binding site. Attached to the reverse gear is the IQ motif which is the consensus binding site for calmodulin and calmodulin-related light chains¹⁷. Next, the tail domain follows with its proximal tail (lever arm extension), medial tail and distal tail. The c-terminal global cargo binding domain (CBD) includes different ligand interaction surfaces. It contains a Motif binding endocytic adaptors RRL (Arg-Arg-Leu) or a WWY (Trp-Trp-Tyr) motif, binding the endocytic adaptor protein (Dab-2) and the ESCRT-0 component Tom1. Additionally, there are two ubiquitin interacting domains: the motif interacting with ubiquitin (MIU) and the myosin VI ubiquitin-binding domain (MyUb) which binds preferentially K63 linked ubiquitin chains^{18,19}.

Introduction

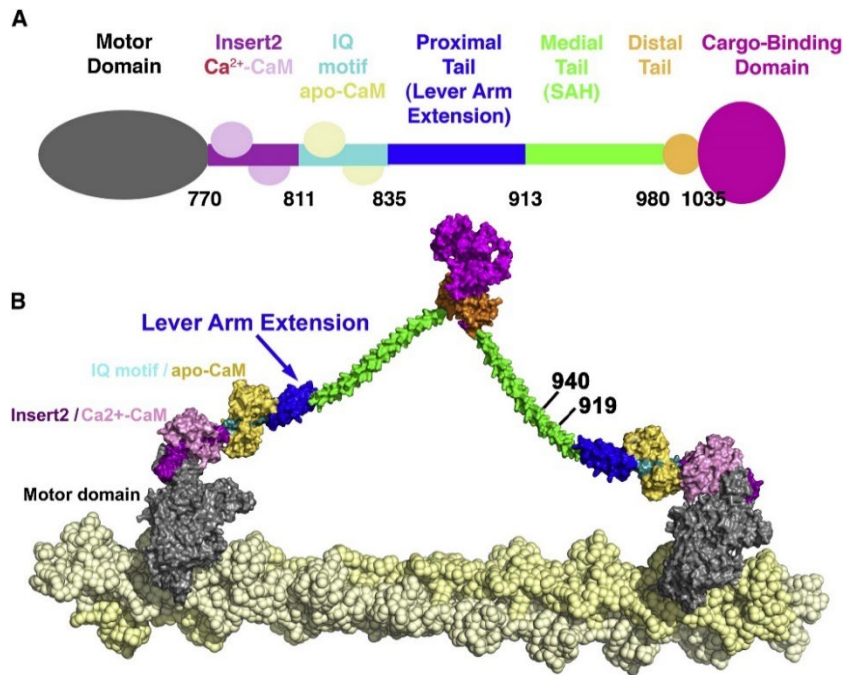


Figure 2: Schematic of Full-Length Myosin VI

(A) Domain organisation of myosin VI; Insert 2 owns a calmodulin (CaM) binding site and the medial tail contains a single alpha helix (SAH) (B) Model of dimeric myosin VI proposed by Spink *et al.* (2008)^{20,21}; leverarm extensions are shown as single alpha helices

Presented in K. Hauschulte, Characterisation of the functions of myosin VI within the cellular response to DNA replication stress, Master-Thesis 2020; Figure adapted from Mukherjea *et al.*, 2009¹⁹

Due to alternative splicing, there are three isoforms in human cells, isoform 1 and 3, collectively referred to as myosin VI_{long} and isoform 2, referred to as myosin VI_{short}^{11,18}. The long form has an alternatively spliced region located between the MyUb and MIU domain. Due to conformational changes, the alternative splice linker masks the RRL motif, resulting in a decreased ability to bind K63-linked ubiquitin chains and RRL-mediated interactors in general¹¹. On the other hand, myosin VI_{long} receives an additional clathrin binding site. The versatility of Myo6 binding sites and its tissue-specific expression pattern indicates its diverse functions in different cellular compartments.

Myo6 is involved in vesicular membrane traffic, to transport and cluster transmembrane receptors in the area of clathrin-coated pit, in endocytosis, in maintenance of Golgi morphology, in facilitating fusion of secretory vesicle at the plasma membrane, in membrane ruffling and many more¹⁷. In general, it is crucial for clathrin-mediated endocytosis and is also stabilizing actin during spermatid individualization. With so many critical tasks to perform, it is not unexpected that defects in Myo6 can result in disease. As mentioned before, one form of deafness is associated with Myo6 mutations, but Myo6 defects in particular are also associated

Introduction

with oncogenesis. The motor protein is constantly overexpressed in prostate and high grade ovarian cancer and there is a link between expression of Myo6 and aggressiveness of ovarian cancer^{22,23}. Furthermore, mutations in Myo6 can lead to hypertrophic cardiomyopathy and neurodegeneration²⁴.

However, even though the cytoplasmic Myo6 is well characterized, a new field of research on nuclear Myo6 has opened up.

1.1.2 Nuclear Myosin VI

The presence of F-actin and myosins in the nucleus was for a long time discussed highly controversial. But there are classes of myosins described in the nucleus and since 2015 the presence of F-actin in the nucleus is indisputable¹⁵. Myo6 is one of the classes described in the nucleus and it has a well-studied role in transcription^{25,26}. There it co-localizes with newly transcribed mRNA and RNA polymerase II (RNAPII). During elongation process, Myo6 modulates RNAPII-dependent transcription and prevents the disruption of organisation at the transcription initiating site. Depletion of Myo6 leads to increased mobility of the transcriptional complex, which can lead to impaired transcription and consequently to reduced transcription^{27,28}.

Myo6 is also described in chromatin regulation. The CBD of Myo6 can bind DNA upon unfolding of its tail domain and thus affect chromatin movement. It can interact directly with nuclear receptors, such as oestrogen²⁵ or androgen²⁹ receptor, and with nuclear lamina. By recruitment to promoter and intragenic regions Myo6 drives expression of target genes.

Another interesting interaction partner of Myo6 is p53³⁰. Jung and colleagues observed that transcription of Myo6 is induced by DNA damage and regulated by p53. In addition, p53 induces relocalisation of Myo6 to the Golgi complex, perinuclear membrane and into the nucleus³⁰. They also observed more DNA damage-triggered apoptotic events in cells upon Myo6 depletion and conclude that Myo6 may be a mediator of the p53 pro-survival pathway³⁰. Furthermore, a role of Myo6 in replication stress response has recently been demonstrated, by my colleagues and me³¹.

1.2 Genome stability

Genome stability is precisely balanced to leave enough room for genome diversification on the one hand, but also to pass genetic material from generation to generation on the other. To achieve genome integrity, there has to be mostly error-free replication of DNA and the repair of replication mistakes or damaged DNA. External and internal factors can affect the stability of the genome and lead to diseases such as cancer. To prevent too many mutations in the genome and protect the organism from disease-promoting ones, there are DNA repair strategies.

1.3 Replication stress response

One of this strategies is the replication stress response. This part of my thesis is published as Shi *et al.*, 2023 Nature Communications³¹.

1.4 Double strand break repair

Double strand breaks (DSBs) are one of the most dangerous lesions in the cell. They create a great risk of genomic rearrangements. Loss of large chromosomal regions or disruption of gene structure and function may result. Due to this drastic interference with genome stability, DSBs are often the primary transformation step in cancer³². DSBs can arise from physiological processes such as errors in replication or incidental action by nuclear enzymes, but can also be caused by external sources such as ionizing radiation (IR) or reactive oxygen species (ROS). The causes of DSBs are just as diverse as their types. They range from staggered 3' or 5' overhangs to blunt DNA ends to single ended DSBs (seDSBs). In order to correctly repair this multitude of different DSBs, there are just as many different repair mechanisms available.

However, before a repair pathway can be chosen, DSBs must be recognized by the cell. For this purpose, DSBs trigger an extensive chromatin response. This process is called DNA damage response (DDR) and an early event in this cascade is the activation of Ataxia telangiectasia mutate (ATM) through auto-phosphorylation³³. Once active, NBS1 interaction triggers the recruitment of ATM to the DSB site. There, it phosphorylates RSF1 to reveal chromatin around the break by inducing nucleosome sliding. The variant H2AX histones thus exposed get phosphorylated by ATM, Ataxia telangiectasia and Rad3 related (ATR) and DNA-dependent protein kinase catalytic subunit (DNA-PKcs)³⁴. Subsequently, chromatin near the DSB is processed with a complex ubiquitin code by RING finger protein 8 (RNF8), RING finger protein 168 (RNF168) as E3 ubiquitin ligases, and the breast cancer type 1-receptor associated protein 80 (BRCA1-RAP80) complex with deubiquitinating functions³⁵⁻³⁷. Following, repair

pathway selection begins with the major players 53BP1, which negatively regulates resection in G1, and BRCA1, which promotes 53BP1 removal from DSB sites³⁸.

1.4.1 Repair pathway choice

The selection process, to find the appropriate repair pathway is triggered by many factors, such as the stage of the cell cycle, the type of lesion, the local chromatin environment, and more. After DSB-induction, the ends must be edited by nucleosome remodelling to make them accessible to repair proteins if they were not accessible to them from the beginning (Figure 3). Following, the heterodimer KU70/80 binds the DSB ends rapidly and very tightly. The next step depends on whether the cell and chromatin context favours or prevents DNA resection³⁹. At the G1 and early G2 cell cycle stage, cells preferentially use classical non-homologous end joining (cNHEJ) pathway to repair DSBs, which is initiated when resection does not occur. Thus, in a resection non-permissive environment, the cells prefer cNHEJ. This pathway may or may not process DNA ends to make them ligatable. Through this branch of the decision tree, the lesion would be repaired with cNHEJ.

Back to the branch, whether or not there is a resection environment. At the late G2 and S cell cycle stage, cells mostly use homologous recombination (HR). After short range resection by MRE11 and CTIP, KU70/80 needs to be removed from DSB ends^{40,41}. After its extraction, there is enough space for long range resection by EXO1, BLM and DNA2. In general, with functioning Rad51, cells would progress with HR. But when Rad51 is defective, the cell still has the option to use alternative end joining (aEJ) or single strand annealing (SSA)⁴².

Introduction

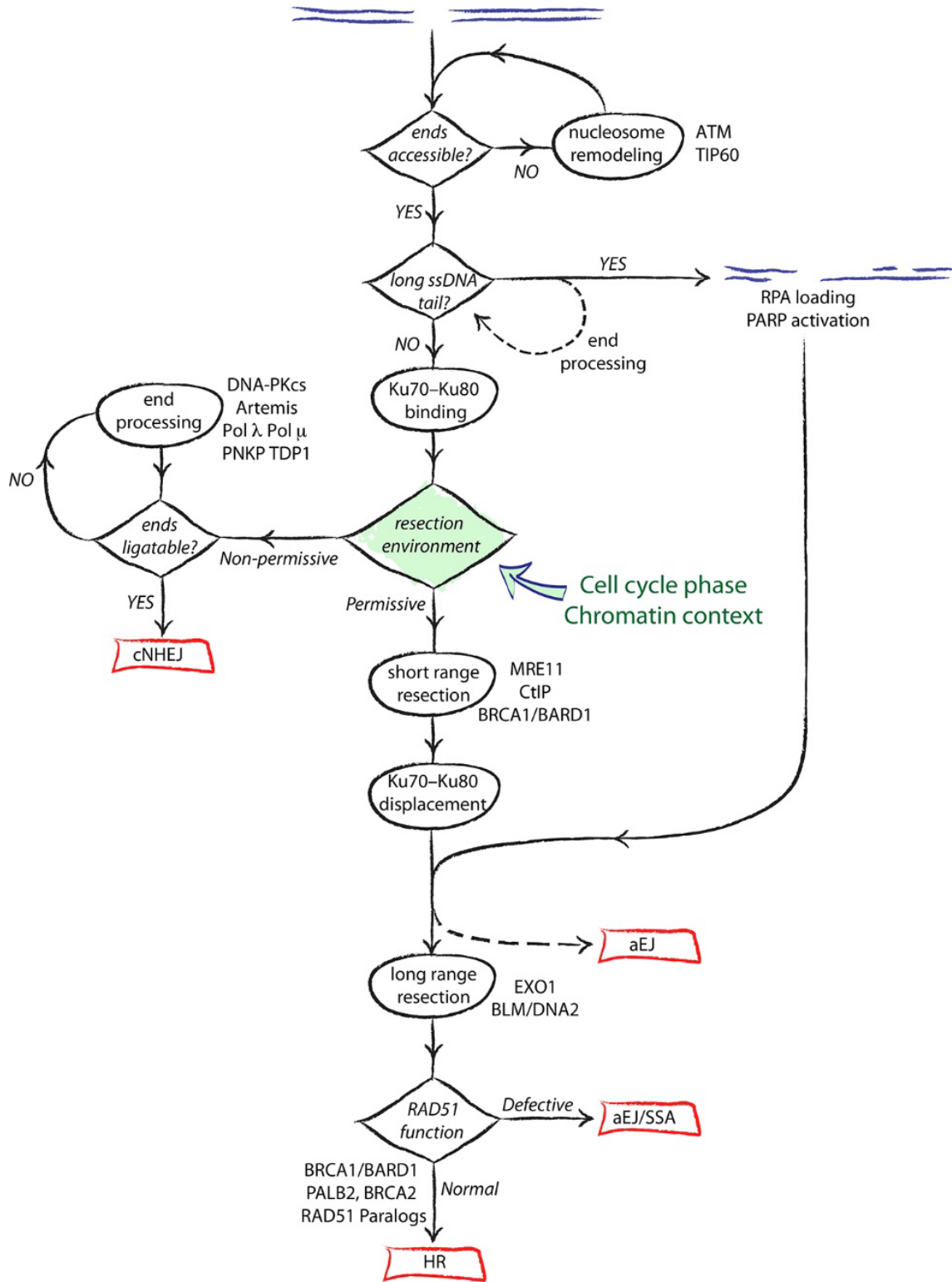


Figure 3: A decision tree of DNA double strand break repair

The repair pathway is primarily determined by DNA end resection. If the cell is at a cell cycle stage, which does not favour resection, KU70/80 will remain at the DNA end and initialize NHEJ. However, if resection is initiated, KU70/80 is removed and homologous recombination (HR) is initialized. Alternative pathways such as alternative end joining (aEJ) or single strand annealing (SSA) can be used opportunistically, as a complement to the commonly used NHEJ and HR. Adapted from Scully *et al.*, 2019⁴²

1.4.2 Non Homologous End Joining

cNHEJ is the major DSB repair pathway in mammalian somatic cells. It is active throughout the cell cycle, with the exception of M phase. Approximately 75 % - 85 % of IR-induced DSBs in G2 and G1 are repaired with cNHEJ⁴³. When the cell is at a state where it forms a non-permissive resection environment, cNHEJ is initiated. It is a resection independent pathway, but can perform very limited resection if necessary. Up to 5 nucleotides can be resected to achieve micro-homologies and re-ligate DSB ends back together⁴⁴.

After the general DDR in form of H2AX phosphorylation, KU70/80 heterodimer binds each DNA end of the DSB⁴⁵ (Figure 4). Subsequently, KU70/80 recruits DNA-PKcs and the nuclease Artemis, which form the Artemis-DNA-PK complex. DNA polymerases Pol μ and Pol λ are completing this primary nuclease complex, which is responsible for minimal end processing. In a template-dependent or template-independent manner, the polymerases can also incorporate nucleotides at DSB ends. This represents the first-stage of long-range synapsis of the two DSB ends⁴⁶. In the second step, of the two-stage mechanism, KU70/80 recruits DNA ligase IV (LIG4), XRCC4, XRCC4-like factor (XLF) and paralogue of XRCC4 and XLF (PAXX)^{47,48}. These factors result in closely aligned DSB ends that eventually are re-ligated back together³⁴.

When there is a non-permissive resection environment, but cNHEJ is not suitable for DSB repair, there are sub-pathways such as aEJ and MMEJ. They are most likely used opportunistically for cNHEJ, scavenging on the products of aborted or incomplete cNHEJ^{42,49,50}.

1.4.1 Homology directed Repair

The second most used pathway is HDR. It is restricted to late G2 and S-phase because it requires sister chromatids for proper DSB repair. HDR is a resection dependent pathway and involves two steps of resection. First, short range resection is carried out by MRE11, RAD50 and NBS1 which build the MRN complex. MRE11 initiates the ssDNA nick using its endonuclease activity (Figure 4). Following, with its exonuclease activity, it produces 3' ssDNA through digestion towards the DSB end in a 3' 5' direction⁵¹. During short range resection, KU70/80 gets modified with K48-linked ubiquitin chains by SCFFbx112, RNF8 and RNF138^{37,52-54}. This ubiquitination pattern recruits Valosin-containing protein (VCP)/p97 to the DSB site. The hexameric AAA+-type ATPase removes KU70/80 from the DNA, using the energy of ATP hydrolysis, for subsequent downstream degradation by the proteasome⁵⁵. KU70/80 needs to be removed, because it blocks the second resection step at DSB ends, long range resection⁵⁶. After

Introduction

the extraction of KU70/80 the long range resection can start. During this process, Exonuclease 1 (EXO1), Bloom syndrome protein (BLM) and endonuclease DNA2 act together to unwind and digest the DNA 5' strand to create long 3' overhangs. This ssDNA overhangs range between a few hundreds of nucleotides to tens of kilobases⁵⁷. To protect the ssDNA, it is rapidly coated with replication protein A (RPA). After phosphorylation of RPA, it gets replaced by RAD51 and forms filaments. This filament is a dynamic structure and is physiologically regulated to optimize HDR efficiency. Homology search, which defines HDR, is mediated by recombinase Rad51 bound ssDNA. It invades duplex DNA molecules and facilitates base pairing with complementary homologous DNA sequences⁴². The BRCA1-BARD1 complex enhances the recombinase activity of RAD51 to supports the intermediate DNA joint formation⁵⁸. Other factors such as BRCA2 and RAD52 also play important roles for homology search and strand invasion. When a homologous sequence is found on a sister chromatid, the strand exchange starts and a double holiday junction is formed. During this step RAD51 filaments are disassembled⁵⁹. In the last step the new complementary DNA gets synthesized by polymerase δ and after dissolving the double holiday junction, the DSB ends are re-ligated back together. This process can result in crossing over between recombining DNA and can be detected as sister chromatid exchange⁶⁰. Through the use of this large homology stretches, the HDR pathway is considered error-free and very accurate.

Subpathways for HDR are for example synthesis-dependent strand annealing (SDSA) or single strand annealing (SSA). SDSA is identical with HDR until the step of nascent strand synthesis. This pathway uses strand displacement annealing instead of double holiday junction. Thus, rather than both strands being attached to DNA, only one end of the DSB becomes invasive by RAD51, while the other strand remains passive⁶¹. This explains why only non-crossover products are formed during SDSA. The other sub-pathway SSA is used when the 3' overhang, created during resection, contains highly homologous direct repeats. Most likely, SSA is only used as a backup for HDR because it is error-prone due to the loss of one annealed repeat in the DNA sequence⁶².

Introduction

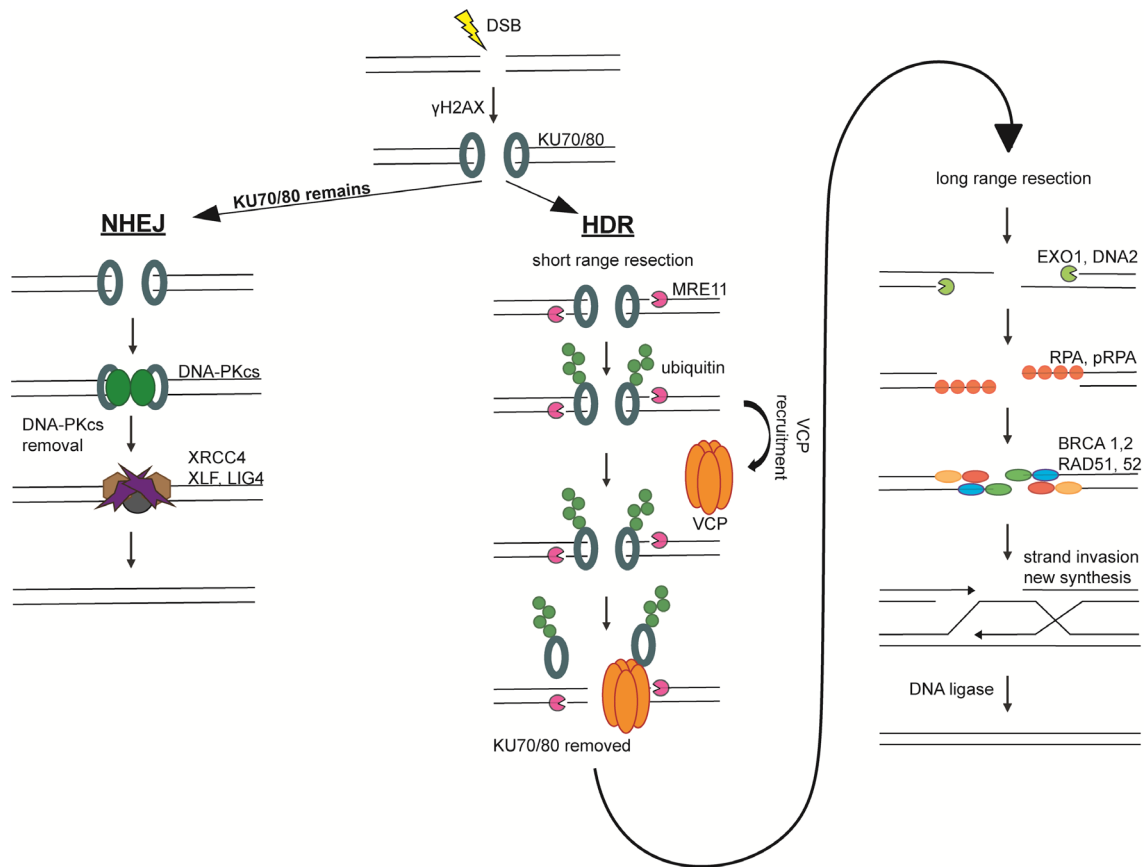


Figure 4: NHEJ and HDR - the two main DSB repair mechanisms

After the Double strand break (DSB) Histone variant H2AX gets phosphorylated (γ H2AX). KU70/80 heteromer is directly binding both DSB ends. IF KU70/80 remains at the DSB ends, non homologous end joining (NHEJ) is initialised. DNA-dependent protein kinase catalytic subunit (DNA-PKcs) is recruited to DSB and perform minimal end processing. After removal of DNA-PKcs, XRCC4, XRCC4-like factor (XLF) and ligase 4 (LIG4) are ligating the DSB ends back together. Homology directed repair (HDR) is initialised by short-range resection carried out by MRE11. Subsequently, KU70/80 gets ubiquitinated, recruiting valosin containing protein (VCP), which removes KU70/80 from the DSB ends. After long range resection by exonuclease 1 (EXO1) and endonuclease DNA2, ssDNA is rapidly bound by replication protein A (RPA). This gets subsequently phosphorylated (pRPA) and then replaced by RAD51 / Rad 52. With the help of BRCA1 and BRCA2 strand invasion takes place in form of a double Holliday junction and synthesis of nascent DNA. In the final step, the DNA is ligated by polymerase δ .

1.4.2 Drugs to investigate on DSBs

There are many ways in which DSBs are generated in cells. Endogenous DNA damage occurs during replication, incidental action by nuclear enzymes, breaks during V(D)J recombination or immunoglobulin heavy chain (IgH) class switch recombination. To create controlled conditions and better investigate on DSBs, there are also external sources that can generate DSBs. The exposure of cells to ultraviolet radiation (UV) (mainly UV-B: 280–315 nm) creates 6-4 photoproducts, cyclobutane-pyrimidine dimers and DNA strand breaks⁶³. Through creating also other DNA lesions, it is often used to investigate on base excision repair, nucleotide excision repair or mismatch repair. Ionising radiation (IR) leads to DNA single-strand breaks (SSBs), DSBs and base lesions⁶⁴. It is a well-known tool to investigate on DSB repair pathway choice and DSB repair mechanisms. In literature, neocarzinostatin (NCS) is often used as analogue to IR, because it is creating similar lesion patterns. It is obtained from cultures of *Streptomyces carzinostaticus*. The radiomimetic reagent induces reactive oxygen species (ROS) which following damage the DNA and induce SSBs and DSBs^{65,66}. Another agent to investigate specifically on single-ended DSBs (se-DSBs) is camptothecin (CPT). It stabilizes topoisomerase I at the DNA so that the DNA cannot be re-ligated after cutting (in form of a SSB)⁶⁷. This creates a se-DSB during replication, which explains why CPT only creates DSBs during S phase. CPT is often used to investigate on HDR, because this pathway is also restricted to late G2 and S phase. Another topoisomerase inhibitor is etoposide (ETO). It stabilizes topoisomerase II at the DNA and prevents re-ligation after cutting in form of a DSB⁶⁸. In this way, DSBs are formed during S phase independently of replication.

1.5 F-Actin involvement in DSB repair

The research area of the actin cytoskeleton being active in the nucleus has been controversial for a long time. There was no convincing proof, that F-actin (for example) is present in the nucleus. By further developing the research methods, it was finally possible in 2015 to make F-actin visible in the nucleus using a nuclear actin-chromobody¹⁵. Already before this discovery, researchers were investigating on nuclear F-actin. Andrin *et al.* demonstrated that disruption of F-actin leads to an inhibition of DSB repair *in vitro* and *in vivo*⁶⁹. Further they hypothesized about a role of F-actin in stabilizing KU70/80 at the DSB ends. Based on their observations that KU80 retention of DSB ends was impaired when they expressed an actin mutant that cannot polymerize or when actin filament formation was inhibited⁶⁹.

In 2018, Schrank *et al.* and Caridi *et al.* used new techniques, such as the nuclear chromobody, to demonstrate beyond doubt that F-actin is involved in DSB repair^{20,21}. Caridi and colleagues

Introduction

have shown that in *Drosophila* and mouse cells, F-actin and myosins are critical for the transport of DSB to the nuclear periphery. The ARP2/3 complex polymerizes F-actin at DSB repair sites and thereby promotes the re-localization process of the DSB. The repair foci are shown to migrate along F-actin and a direct role for directional re-localization is demonstrated. Furthermore, it is shown that class 1 and class 5 myosins, the molecular motors on F-actin, are recruited to DSB repair sites. In summary, Caridi and colleagues demonstrated that the Arp2/3 complex, F-actin, and myosins are critical for re-localization of DSBs to the nuclear periphery. The importance of this mechanism is highlighted by the fact that this pathway is highly conserved in *Drosophila* and mouse cells²¹.

The second paper published in 2018 by Schrank and colleagues used observations in *Xenopus laevis* cell-free extracts and mammalian cells to show the involvement of nuclear F-actin, WASP and Arp2/3 in clustering DNA breaks for the HDR pathway²⁰. DSBs repaired by HDR have to be organized in sub-nuclear clusters and Schrank *et al.* postulate that actin-based mobility shapes this chromatin reorganisation. The enrichment of Arp2/3 and F-actin at DNA DSB foci repaired by HDR was demonstrated. Furthermore, inactivation of ARP2/3 showed a reduction in DSB movement. Using the small molecule inhibitor CK666, which inhibits ARP2/3, actin filament formation mediated by ARP2/3 is disrupted. They took advantage of this to investigate the role of ARP2/3 in more detail. They observed that DSB end resection was impaired after the addition of CK666. In contrast to the accumulation of ARP2/3 in DSB repaired by HDR, no accumulation was observed in DSB repaired by NHEJ. Taken together they showed a role of F-actin in resection, during HDR, and in generating repair domains for DSBs²⁰.

1.6 Biological consequences

The biological consequences of DNA damage when DNA repair mechanisms are impaired are fatal for the cell. Unrepaired DNA damage leads to mutations. If these occur in crucial genes, they can lead to cancer or many other diseases⁷⁰. To avoid these disease-promoting consequences, cells have important safety mechanisms to stop cells with damaged DNA from proliferating. During replication, there are several checkpoints that ensure that the cells only continue replication with undamaged DNA⁷¹. In the case of other DNA damage, the cell also activates checkpoints and a general DNA damage response. If too much DNA damage in a cell remains unrepaired, the cell can initiate controlled cell death⁷². This process is called apoptosis. An alternative, rather than driving the cell into controlled death, is senescence, a controlled state of stable growth arrest⁷³.

1.6.1 Senescence

In the first place, senescence is a very potent tumor suppressor mechanism⁷⁴. It is characterized as stable and in general reversible cell cycle arrest in G1 and S phase. When cells accumulate unrepaired DNA damage, they can induce senescence. This prevents the cell from propagation of corrupted genetic material to daughter cells. DDR triggers checkpoint activation and cell cycle arrest, until the damage is repaired. When this signalling cascade becomes chronic, it can result in proliferative arrest in form of cellular senescence⁷⁵. For the regulation of senescence, the activation of p53 is crucial (Figure 5). A stable p53 leads to cell cycle arrest by inducing expression of the CDK2 inhibitor p21^{WAF1/Cip1}, which suppresses phosphorylation of pRB. This process is supported by overexpression of the CDK4/6 inhibitor p16^{INK4A}, which inhibits the activity of E2F protein members⁷³. P21 is activated upon initialization of senescence. P16 is activated downstream, most likely to maintain the senescence phenotype⁷⁶.

Other common features of senescent cells include profound alterations in the (epi-) genetic landscape and gene expression, impaired metabolism, macromolecular damage and a hypersecretory phenotype. Senescent cells display morphological and metabolic changes such as dramatically enlarged cell size or senescence-associated- β -galactosidase (SA- β -gal) accumulation (Figure 5). They also show oxidative damage by increased reactive oxygen species (ROS). During senescence, transcriptional activation of a senescence associated secretory phenotype (SASP) program characterized by cytokines, chemokines, growth factors, and extracellular matrix (ECM) proteases is established⁷³. This may enhance senescence itself or affect the local tissue microenvironment of senescent cells and potentially the whole organism. Activation of SASP is a dynamic process that accompanies the development of senescence. Depending on the trigger and the cell type, SASP composition varies a lot. However, in general, the secretions consist of pro inflammatory interleukin-6 (IL-6), CXC chemokine ligand 8 (CXCL8, hereafter named IL-8) and monocyte chemoattractant protein 1 (MCP1; also known as CCL2)⁷⁷. It also includes matrix metalloproteinases (MMPs), serine/cysteine proteinase inhibitors (SERPINs) and tissue inhibitors of metalloproteinases (TIMPs)⁷⁸⁻⁸⁰. All this components can be classified into four classes: extracellular matrix/cytoskeleton/cell junctions, metabolic processes, ox-redox factors and regulators of gene expression⁸⁰.

Senescence is initiated by a chronic DNA damage response (DDR), but this can have different causes. DDR can be triggered by direct DNA damage (caused e.g. by IR or UV) or for example by shortened telomeres. Another source can be oncogene activation, which for instance results

Introduction

in replication stress after severe mitochondrial damage by ROS and subsequently also triggers DDR (Figure 5).

Even though senescence has important roles during development and in reducing tumor progression, it is often associated with age-related diseases⁸¹. During aging, senescent cells accumulate, triggering low-grade chronic inflammation and thereby contributing to age-related dysfunction⁸¹. Through this contribution, senescence is classified as a central hallmark of aging.

Introduction

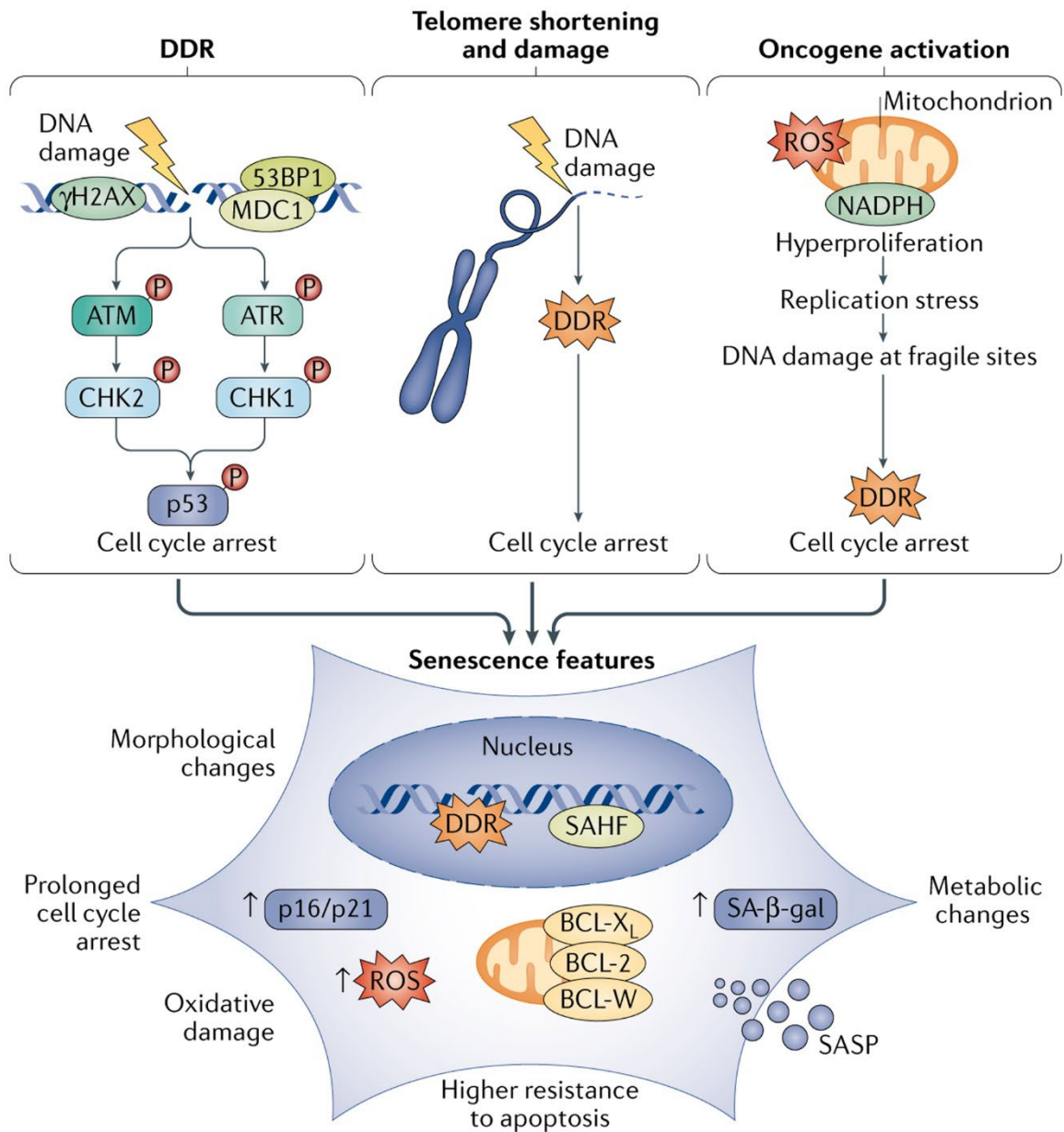


Figure 5: Senescence drivers and phenotypes

The DNA damage response (DDR) can be triggered by direct DNA damage, by telomere shortening or damage, or by activation of oncogenes. The DDR includes phosphorylation of H2AX (γ H2AX), recruitment of 53BP1 and MDC1 to the damage site. Next, Ataxia telangiectasia mutated (ATM), Ataxia-telangiectasia mutated and Rad3-related (ATR), Checkpoint kinase 2 (CHK2) and Checkpoint kinase 1 (CHK1) are phosphorylated, resulting in p53 phosphorylation, which in turn causes cell cycle arrest. Upon too much unrepaired DNA damage the cell can go into senescence. Senescence features are morphological changes such as enlarging of cell size, metabolic changes, senescence-associated- β -galactosidase (SA- β -gal) accumulation, senescence-associated heterochromatin foci (SAHF) and senescence-associated secretory phenotype (SASP). In addition, p16 and p21 are upregulated and increased levels of reactive oxygen species (ROS) result in oxidative damage. However, the main feature of senescence is reversible, prolonged cell cycle arrest and higher resistance to apoptosis. Adapted from Di Micco *et al.*, 2021⁸²

1.7 Previous research

After showing that components of the cytoskeleton are involved in DSB repair, the burning question arose whether other components may play a role as well. My supervisor focussed on myosins, as molecular motors on F-actin. A mass spectrometry experiment revealed interaction of Myo6 with DNA repair factors³¹ and a traffic light reporter assay showed an impairment of HDR efficiency upon Myo6 *knockdown*. Checkpoint activation assays in which level of phosphorylated RPA was verified by Western blot confirmed the previous results and showed a decrease of pRPA in Myo6 KO cells. In my master thesis, I was characterising Myo6 involvement in HDR pathway. Using various immunofluorescence (IF) microscopy assays, I demonstrated that all marker proteins tested of HDR showed a reduction in Myo6 KO cells upon CPT treatment. It was compared γ H2AX (as general DNA damage marker), RPA foci, and pRPA intensity in A549 WT and Myo6 KO cells. The kinetics with these damage / repair marker showed no delay in Myo6 KO cells in comparison to WT cells upon CPT. Furthermore, colony formation assays revealed a survival defect in Myo6 KO cells upon CPT treatment.

As a possible consequence of impaired DSB repair mechanisms, it was an exciting approach to also investigate Myo6 in senescence. There are several indications that it may play a role in stable cell cycle arrest. Myo6 interacts with p53 (a key factor in senescence induction), it is involved in secretion (a very important process during SASP) and Myo6 is involved in transcription, which is responsible for the establishment and maintenance of SASP.

In initial experiments, it was observed that RPE-hTERT and MCF10A cells displayed cell cycle arrest in G1 and typical phenotypes associated with senescence such as a dramatic increase in cell size upon Myo6 depletion. The same phenotype upon Myo6 depletion was recently published by Magistrati *et al.*⁸³. They observed a cell cycle arrest in hTERT-RPE1 and BJ-hTERT cells upon Myo6 knockdown. Interestingly, this phenotype could be rescued by co-depletion of p53, which is an important tumor suppressor protein and plays a key role in inducing senescence.

Based on all these literature research and data I wanted to get a deeper insight into Myo6 role in HDR pathway. To understand better in which step exactly it is involved in and through which mechanism it is supporting DSB repair. It was also very interesting for me to investigate its role in senescence and probably also to find a link between Myo6 role in DNA repair and senescence induction.

Introduction

2. Materials & Methods

2.1 Equipment & Material

Table 1: Lab devices and equipment

Equipment	Product type	Source company
Automated Cell Counter	TC20™	Bio-Rad
BD LSRFortessa SORP	Flow Cytometer	BD
CO2-Incubator	FORMA STERI-CULT CO2-Incubator	Thermo SCIENTIFIC
Faxitron CellRad	Cell Irradiator	CellRad
Fusion FX7	Imaging System	Vilber Lourmat S.A
Incubator	B6200	Thermo Scientific
Incubator (37°C)	HERATHERM Incubator	Thermo SCIENTIFIC
Microscope	AF7000	Leica
Microscopy	Leica DMIL LED	Leica
Shaker (incubator)	- Multitron Standard - The Belly Dancer (Shaker)	- Infos-HT - STOVALL Life Science
Table centrifuge Centrifuge	- HERAUS-FRESCO 21 - HERAUES-Multifugex3R	- Thermo SCIENTIFIC - Thermo SCIENTIFIC
Tecan Spark 20M	Microplate reader	Tecan
Thermomixer	Thermomixer comfort	Eppendorf
Vacuumpump	Mini-Vac power	Axonlab
Vortexer	RS-WA 20	PHOENIX Instruments

2.2 Computer programs

Table 2: Software

Program	Source company	Application
Adobe Illustrator V27.3.1	Adobe	Graphic design
FIJI	Freeware	Image Analysis
FlowJo V7	BD Biosciences	Flow Cytometry data
GraphPad Prism 7™	GraphPad	Graphic analysis, Statistical analysis
ImageJ	Freeware	Image Analysis
Microsoft Excel	Microsoft Corporation	Data analysis

2.3 Reagents

2.3.1 Chemicals

Table 3: Chemicals

Chemical	Source	Identifier
Albumin (bovine serum albumin, BSA)	Merck	Cat#A7906
Amersham ECL Prime Western Blotting Detection Reagent	Thermo Fisher Scientific	Cat#12994780
Amersham ECL Select Western Blotting Detection Reagent	Thermo Fisher Scientific	Cat#RPN2235
CK-666	Sigma-Aldrich	SML0006-25MG

Materials & Methods

Chemical	Source	Identifier
cOmplete Protease Inhibitor Cocktail	Roche	Cat#5056489001
Dimethyl sulfoxide, DMSO	Sigma-Aldrich	Cat#D8418
Crystal violet solution 1 %	Sigma-Aldrich	Cat#V5265-500ML
DMEM, high glucose, pyruvate, no glutamine	Thermo Fisher Scientific	Cat#21969035
Doxycycline hydrochloride	Merck	Cat#D3447
FuGENE® HD Transfection Reagent	Promega	Cat#E2311
Glycine	Merck	Cat#G7126
Hoechst 33342	Thermo Fisher Scientific	Cat#11534886
Hygromycin B Gold	Invivogen	Cat#ant-hg-1
L-Glutamine (200 mM)	Thermo Fisher Scientific	
Lipofectamine® 2000	Thermo Fisher Scientific	Cat#11668019
Lipofectamine® RNAiMAX	Thermo Fisher Scientific	Cat#13778150
Methanol	Thermo Fisher Scientific	Cat#15654570
Milk powder, skim milk	Merck	Cat#70166
NMS-873	Sigma-Aldrich	Cat#SML1128-5MG
NuPAGE LDS Sample Buffer (4X)	Thermo Fisher Scientific	Cat#11559166
PageRuler Prestained Protein Ladder	Thermo Fisher Scientific	Cat#11822124
Paraformaldehyde	Merck	Cat#P6148
Penicillin-Streptomycin (10,000 U/mL)	Thermo Fisher Scientific	Cat#15140122
Ponceau S	Merck	Cat#P3504
ProLong™ Diamond Antifade Mountant	Thermo Fisher Scientific	Cat#15205739
SDS, 20%, Sodium dodecyl sulfate	Merck	Cat#05030
SIGMAFAST protease inhibitor cocktail	Merck	Cat#S8830
Sodium deoxycholate	Merck	Cat#D6750
Triton X-100	Merck	Cat#T9284
Trypsin, MS-approved	Serva	Cat# 37286
Tween-20	Merck	Cat#P7949
IGEPAL	Sigma-Aldrich	Cat#I8896
Click-iT® Plus EdU Alexa Fluor® 647 imaging kit	Fisher Scientific	Cat#15224959
DAPI; 4',6-Diamidino-2'-phenylindole dihydrochloride	Sigma-Aldrich	Cat#D9542
EdU (5-ethynyl-2'-deoxyuridine)	Life Technologies	Cat#E10187
MG132 (Proteasome inhibitor)	Enzo Life Sciences	Cat# BML-PI102-0025

Materials & Methods

Chemical	Source	Identifier
RNase A	Sigma-Aldrich	Cat# 10109169001
Senescence β-Galactosidase Staining Kit	MERCK	Cat#9860S
Beta Galactosidase (β-Gal) Activity Assay Kit (Fluorometric)	BioVision	Cat#K821
Formaldehyde solution, 36.5-38% in H₂O	Merck	Cat#F8775
Trypsin-EDTA (0.05%), phenol red	Thermo Fisher Scientific	Cat#25300054
4-15% Criterion™ TGX Stain-Free™ Protein Gel, 26 well, 15 μl	Bio-Rad Laboratories	Cat#567-8085
Mini-PROTEAN TGX Stain Free Gels, 4-15%, 15-well	Bio-Rad Laboratories	Cat#456-8086

2.3.2 Antibodies

Table 4: Antibodies

Antibody	Source	Identifier	dilution
Goat anti-Mouse IgG (H+L) Cross-Adsorbed Secondary Antibody, Alexa Fluor™ 488	Thermo Fisher Scientific	Cat#A-11001 RRID: AB_2534069	1:500 (IF)
Goat anti-Mouse IgG (H+L) Secondary Antibody, Alexa Fluor 647	Thermo Fisher Scientific	Cat#A-21236 RRID: AB_2535805	1:500 (IF)
Goat anti-Rabbit IgG (H+L) Cross-Adsorbed, Alexa Fluor 647	Thermo Fisher Scientific	Cat#A-21244 RRID: AB_2535812	1:500 (IF)
Mouse monoclonal anti- RPA2 (clone 9H8)	Thermo Fisher Scientific	Cat# MA1-26418 RRID: AB_795362	1:2000 (IF)
Mouse monoclonal anti-BrdU (B44)	BD Biosciences	Cat#347580 RRID: AB_400326	1:100 (IF)
Mouse monoclonal anti-KU70 (N3H10)	Santa Cruz	Cat#sc-56129 RRID: AB_794205	1:100 (IF)
Mouse monoclonal anti-KU80 (111)	Invitrogen	Cat#MA5-12933 RRID: AB_10983840	1:100 (IF)
Mouse monoclonal anti-phospho-Histone H2A.X (Ser139) (clone JBW301)	Millipore	Cat# 05-636; RRID: AB_309864	1:1000 (IF)
Rabbit monoclonal anti- Rad51 (DAB10)	Cell Signaling Technology	Cat#8875 RRID: AB_2721109	1:100 (IF)
Mouse monoclonal anti-P16 (F-12)	Santa Cruz	Cat#sc-1661 RRID: AB_628067	1:100 (IF)
Mouse monoclonal anti-P21 (F-5)	Santa Cruz	Cat#sc-6246 RRID: AB_628073	1:100 (IF)

Materials & Methods

Antibody	Source	Identifier	dilution
Rabbit polyclonal anti-53BP1	Novus	Cat#NB100-304 RRID: AB_1659864	1:1000 (IF)
Rabbit polyclonal anti- phosphor RPA32 (S33)	Biomol	Cat# A300-246A-T RRID: AB_2180847	1:1000 (IF)
Mixture of two monoclonal Mouse anti-GFP (7.1 und 13.1)	Roche	Cat#11814460001 RRID: AB_390913	1:10.000 (WB)
Rabbit polyclonal anti-Myosin VI	Wollscheid <i>et al.</i> ¹⁸	n/a	1:1000 (WB)
Mouse monoclonal anti-P53	Santa Cruz	Cat#sc-126 RRID: AB_628082	1:1000 (WB)

2.3.3 siRNAs

Table 5: siRNAs

siRNA	Source	Identifier
Allstars Negative control siRNA	Qiagen	Cat#SI03650318
Hs_MYO6_5 FlexiTube siRNA	Qiagen	Cat#SI03142692
Hs_MYO6_7 FlexiTube siRNA	Qiagen	Cat#SI04243351
Hs_MYO6_8 FlexiTube siRNA	Qiagen	Cat#SI04370737
Hs_MYO6_10 FlexiTube siRNA	Qiagen	Cat#SI04998749
Arid-1A siRNA		

2.3.4 Plasmids

Table 6: Plasmids

Plasmid	Application	Source
pLENTI-GFP-SPOP-M6G4	Stable cell lines	Hans-Peter Wollscheid
pLENTI-GFP-SPOP-E3_5	Stable cell lines	Hans-Peter Wollscheid
pLENTICMV_GFP_M6G4_2RING	Stable cell lines	Hans-Peter Wollscheid
pLENTICMV_GFP_E3_5_2RING	Stable cell lines	Hans-Peter Wollscheid
pMDLgIpRRE (P21 = packaging plasmid with Gag & Pol)	Stable cell lines	Vassilis Roukos / IMB
pRSV-Rev (P22 = packaging plasmid with Rev)	Stable cell lines	Vassilis Roukos / IMB
pMD2.G (VCV-G envelope expressing plasmid)	Stable cell lines	Vassilis Roukos / IMB
pSLIKHYGRO	Stable cell lines	Simona Polo / IFOM
pSLIKHYGRO-UTR4-shMyo6	Stable cell lines	Simona Polo / IFOM
pSLIKHYGRO-ORF9-shMyo6	Stable cell lines	Simona Polo / IFOM

2.4 Media and buffer solutions

Table 7: Media and buffer solutions

Buffers	Source / Content
10xPBS	Media Laboratory, IMB
PBST solution	Phosphate-buffered saline 0.1% Triton
Gibco DMEM	Thermo Fisher Scientific
Gibco DPBS	Thermo Fisher Scientific
Gibco Trypsin	Thermo Fisher Scientific
1x PBS	Media Lab, IMB
Blocking Solution	3 % BSA in PBS
CSK A buffer	100 mM PIPES pH 6.8; 1 mM EGTA; 100 mM NaCl; 300 mM Sucrose; 0.5 % Triton
CSK B buffer	10 mM PIPES, 100 mM NaCl, 300 mM sucrose, 3 mM MgCl ₂ , 1 % Triton-X, 0.3 mg/ml RNaseA
Resection-Assay-Buffer	100 mM PIPES pH 6.8, 1 mM EGTA, 100 mM NaCl, 300 mM Sucrose, 0.5 % Triton
RIPA buffer	50 mM Tris pH 7.5, 150 mM NaCl, 2.5 mM MgCl ₂ , 1% IGEPAL, 0.5% Sodiumdeoxycholate, 0.1% SDS, 10 mM DTT, 1 tablet Phosphatase inhibitor I (for 10ml buffer), 200 µl Protease inhibitor (dissolve 1 tablet in 2 ml H ₂ O)

2.5 Mammalian cell lines

Table 8: Mammalian cell lines

Cell line	Cell type / tissue	Source
A549	Lung epithelia	Simona Polo / IFOM
A549 Myo6 KO	Lung epithelia	Simona Polo / IFOM
A549 TETon GFP-E3_5-SPOP	Lung epithelia	This Thesis
A549 TETon GFP-M6G4-SPOP	Lung epithelia	This Thesis
A549 TETon GFP-E3_5-NLS	Lung epithelia	This Thesis
A549 TETon GFP-M6G4-NLS	Lung epithelia	This Thesis
A549 TETon GFP-E3_5-2RING	Lung epithelia	This Thesis
A549 TETon GFP-M6G4-2RING	Lung epithelia	This Thesis
HeLa	Cervix, epithelia	Hans-Peter Wollscheid / IMB Mainz
HeLa Myo6 KO	Cervix, epithelia	Hans-Peter Wollscheid / IMB Mainz
BJ	Skin, foreskin	Marco Demaria / ERIBA
BJ-pSLIKHYGRO-EV	Skin, foreskin	This Thesis
BJ-pSLIKHYGRO-ORF9-shMyo6	Skin, foreskin	This Thesis
BJ-pSLIKHYGRO-UTR4-shMyo6	Skin, foreskin	This Thesis
WI-38	Lung, fibroblast	Marco Demaria / ERIBA
IMR-90	Lung, fibroblast	Falk Butter / IMB Mainz
IMR90-pSLIKHYGRO-ORF-shMyo6	Lung, fibroblast	This Thesis
IMR90-pSLIKHYGRO-UTR-shMyo6	Lung, fibroblast	This Thesis

CRISPR-Cas9 generated A549 Myo6 *knockout* cells were generated by Simona Polo (IFMO, Milan) and CRISPR-Cas9 generated HeLa Myo6 *knockout* cells were generated by Hans-Peter Wollscheid (IMB Mainz) and kindly provided to me.

2.6 Mammalian cell culture

All cell lines were cultured in Dulbecco's Modified Eagle Medium (DMEM). As additional ingredients 2 mM L-glutamine, 100 U/ml penicillin, 100 µg/ml streptomycin and 10 % (v/v) Fetal bovine serum (FBS) were added. All cell lines were cultured at 37°C in the FORMA STERIL-CULT CO₂ incubator (Thermo SCIENTIFIC) with 5 % CO₂ and operations took place under the sterile hood.

2.6.1 Cell passaging, counting and harvesting

After each 3-4 days, when the cells were about 80 % confluent, they were split. The confluence was checked with a Leica DMIL LED microscope. First, the old medium was removed and then the cells were washed with PBS. To detach the cells, they were incubated with trypsin (0.05 %)-EDTA-phenol red (Gibco) for about 5 minutes at 37°C and then the trypsin was neutralised by adding 2-fold excess of DMEM medium. The cell suspension was then transferred to a new culture plate at a ratio of 1:5 to 1:15.

If an accurate cell count was required, it was determined using the TC20 Automated Cell Counter (Bio Rad). Cells were harvested as previously described and mixed with trypan blue in a 1:1 ratio. The suspension was placed on cell counting slides and counted with the TC20 Automated Cell Counter.

2.7 Treatments

Treatments were performed using 1 µM camptothecin (CPT), 0.5 µg/ml neocarzinostatin (NCS) for 1 h or with 30 min of pre incubation 5 µM NMS-873 (Sigma Aldrich) or 100 µM CK666 (Sigma Aldrich). As a control for inhibitors dissolved in DMSO, 0.1 % DMSO was added to the non inhibitor treated cells.

2.8 Transfections

2.8.1 Lipofectamine RNAiMAX

Transfections were carried out with Lipofectamine™ RNAiMAX transfection reagent. In the control KD, the Myo6 KD and ARID-1A KD cells were transfected before a three day recovery period. Cells were seeded with a confluence of 80 % - 90 % in a 10 cm petri dish. At the next day, 500µl OPTIMEM was mixed with 25 µl Lipofectamine 2000 and incubated for 5 minutes. 500µl OPTIMEM was also mixed with 5 µg siRNA and incubated for 5 minutes. After 5 minutes both, OPTIMEM with Lipofectamine and OPTIMEM with DNA, were mixed and incubated again for 20 minutes. Then cells were washed with PBS and 4 ml of OPTIMEM was

added. After 20 minutes incubation of OPTIMEM-Lipofectamine-DNA-mix, one ml of this mix was added to 4 ml OPTIMEM in each 10 cm dish. This reaction mix was incubated on the cells approximately four to six hours and then replaced by DMEM. To achieve best results for *Myo6 knockdown*, cells were recovered for 48h after transduction. In

Figure S 4 representative western blots for knockdown efficiency are show.

2.8.2 PEI transfection

Cells were seeded on 10 cm petri dish with a confluence of 60 % - 80 %. At the next day, indicated quantities of DNA were added to 2 ml DMEM (without FBS). Following, 50 µl PEI was added and vortexed for 10 seconds. After incubation of 10 minutes, 6 ml of DMEM (with FBS) were added and vortexed. In the last step, medium on the cells was replaced by reaction mix and the cells were brought to S2 lab. After 4 h – 6 h reaction mix was replaced by DMEM.

2.8.3 Cell lysis and Bradford assay

For cell lysis, cells were harvested first by scratching them from the petri dish surface. Following they were washed three times with PBS, to get rid of any medium residues. Next, they were incubated for at least 30 minutes in RIPA buffer on ice. Then lysate was spun at maximal speed to get the supernatant clear of all cell debris. The supernatant was transferred to a clean tube and then the total protein concentration was measured using a Bradford test.

For Bradford assay, 2 µl of cell lysate is mixed with 200 µl Bradford reagent (Sigma-Aldrich). Following 100 µl are transferred into a 96-well plate in duplicates. This 96-well-plate with cell lysate is following measured using the Tecan Spark 20M. With the help of the measured emission at 595 nm, the protein concentrations can then be adjusted.

2.9 Colony Formation Assay

Colony formation assays were performed to examine the viability and the growth of cell lines. Therefore, A549 WT and KO cells were seeded with a confluence of ~ 80 % in 6-well-plates. After recovery overnight, cells were treated with different concentrations of CPT or NCS for 1 h and then harvested. 300 cells were reseeded in 10 cm dishes (in triplicates) and were cultured for 14 days. Using Crystal Violet Blue (Sigma Aldrich) cells were stained for 30 minutes at RT and subsequently washed with deionized water. Following they were dried overnight at RT and counted manually at the next day.

2.10 Immunofluorescence staining

For Immunofluorescence analysis, A549 and HeLa cells were seeded with a confluence of ~ 90 % on coverslips. After indicated treatments, cells were fixed with 4% paraformaldehyde (PFA) (Merck) for 10 min and permeabilized for 10 min at room temperature with 0.3% Triton X-100. Subsequently, cells were blocked with 3% BSA in PBS and then incubated with primary antibodies overnight at 4°C. Next, coverslips were 3 x 5 min washed with PBS and incubation with secondary antibodies and Hoechst (Thermo Fisher Scientific) was performed for 1h at room temperature. After 3 x 5 min wash in PBS, coverslips were mounted with ProLong™ Diamond Antifade Mountant (Thermo Fisher Scientific). Images were acquired with a Leica AF-7000 widefield microscope and analyzed with FIJI.

For RPA and Rad51 staining, cells were pre extracted with 0.3 % IGEPAL for 5 min on ice, twice washed in PBS and then fixed. For BrdU staining, cells were pre extracted with CSK A buffer (100 mM PIPES pH 6.8; 1 mM EGTA; 100 mM NaCl; 300 mM Sucrose; 0,5% Triton) for 5 min on ice, twice washed in PBS and then fixed. For KU80 staining, cells were pre extracted with CSK B buffer (10 mM PIPES, 100 mM NaCl, 300 mM succrose, 3 mM MaCl₂, 1% Triton-X, 0.3 mg/ml RNaseA) for 5 min at RT, twice washed in PBS and then fixed.

2.11 Senescence staining (β-Gal, p16, p21)

Cells were seeded in 10 cm petri dishes to a confluence of about 70 %. Next day, the *knockdowns* using Lipofectamine 2000 were performed (siCTRL, siMyo6). After three days of recovery, the cells were treated - / + 10 Gy IR and were kept in culture for 10 days. Following, cells were three times washed in PBS, fixed with 4 % PFA for 10 minutes at RT and permeabilized in 0.3 % Triton-X in PBS. Staining and analysis was performed according to 2.10 with indicated specific antibodies and with Hoechst or with β-Gal kit (2.12 and 2.13).

2.12 β-Gal Quantification

β-Galactosidase quantification was performed according to Beta Galactosidase (β-Gal) Activity Assay Kit (Fluorometric) (BioVision).

2.13 β -Gal staining

β -Galactosidase activity staining was performed according to Senescence β -Galactosidase Staining Kit (MERCK). The assay was analyzed by eye. The percentage of cells showing β -galactosidase activity was determined.

2.14 Resection Assay

Cells were seeded with a confluence of about 90% on coverslips. Following, the cells were treated with 10 ng/ml BrdU for 24h. After treatment with 1 μ M CPT or 0.5 μ g/ml NCS, cells were pre-extracted with Resection-Assay-Buffer (100 mM PIPES pH 6.8, 1 mM EGTA, 100 mM NaCl, 300 mM Sucrose, 0.5% Triton), washed with PBS and fixed in 4 % PFA for 10 minutes at RT. Permeabilization was carried out using 0.3 % Triton-X. After blocking with 3 % BSA in PBS, cells were incubated over night at 4°C with BrdU specific primary antibodies. On the next day, cells were washed three times with PBS for 5 minutes and then incubated for 1 h with matching secondary antibodies and Hoechst at RT. After 3 x 5 min wash in PBS, coverslips were mounted with ProLong™ Diamond Antifade Mountant (Thermo Fisher Scientific). Images were acquired using a Leica AF-7000 widefield microscope and analyzed with ImageJ.

2.15 Flow Cytometry for cell cycle characterization

Cells were seeded with a confluence of 90 % on 10 cm dishes. On the next day, they were treated for 30 / 60 minutes with 10 μ M EdU and following with or without DNA damaging agent. Then they were harvested by using Trypsin and washed two times in PBS, before fixing in 4 % PFA for 10 minutes at RT. After fixing, cells were permeabilized with 0.1 % Triton-X for 10 minutes at RT, washed two times in PBS and then the click reaction was performed. The click reaction was performed according to manufacturer's protocol of Click-iT® Plus EdU Alexa Fluor® 647 imaging kit. Next, 10 μ g / ml DAPI was added to the cells and they were directly measured at the BD LSRFortessa SORP using indicated lasers.

2.16 Generation of stable cell lines

Stable cell lines were created using lentiviral transduction. HEK293T, as donor cells, were plated with a confluence of 60 % - 80 % on a 10 cm dish. At the next day, HEK293T cells were PEI transfected with 2.5 μ g of plasmids packaging and expressing the DNA of interest (pMDLgIpRRE (P21 = packaging plasmid with Gag & Pol); pRSV-Rev (P22 = packaging

plasmid with Rev); pMD2.G (VCV-G envelope expressing plasmid)). Additionally, 4 µg of the DNA of interest was PEI transfected in the same step. At the next day, supernatant of the HEK293T cells was collected and filtered with a syringe and a 0.45 µm filter to get rid of HEK debris. The target cells were seeded the day before in order to achieve a confluence of 80 % - 90 % on that day. The filtered HEK293T supernatant was then mixed with 8 µg/ml polybrene and added to target cells. 24 h later, the medium of the target cells can be changed and Hygromycine selection with 100 µg/ml started. After a few weeks (depending on the survival rate of the cells) the newly generated cell lines were single cell sorted using flow cytometry. This procedure was performed for A549 WT with 2-RING, SPOP, NLS-DAPRin construct. Also for BJ, IMR-90 and WI-38 with Myo6-ORF depletion, Myo6-UTR depletion and an empty vector construct.

2.17 SDS-Gel and Western Blotting

Proteins to be separated were first mixed with loading dye and boiled at 95°C for 5 minutes. Next they got separated by RunBlue SDS Gel 4-12% upon 170 V for 45 minutes. Using a Trans-Blot Turbo Transfer System gels were blotted on a nitrocellulose membrane and blocked in 5% milk/PBS/0.1% TWEEN-20. After incubation with indicated primary antibodies overnight at 4°C, membrane was washed 3 times in PBS-T and incubated with HRP-coupled secondary antibodies for 1 h at RT and again washed 3 times with PBS-T. The chemiluminescence was detected using a Fusion FX (Vilber Lourmat) instrument.

2.18 Chromatin bound protein pre-extraction

To visualize only chromatin bound KU70/80 the cells were two times pre-extracted with CSK B buffer before lysis. After harvesting, the cells were 5 min pre-extracted and following fresh pre-extraction buffer was added to them. After 3 times 5 minutes of washing in PBS, cells were lysed and analysed by Western blot.

2.19 Microscopy imaging

Microscopy was performed with the AF7000 inverted wide field microscope (Leica) with a 64x / 1.4 oil objective (Leica). The exposure time for IF was 50 ms for Hoechst and 200 ms for 647 nm and 488 nm channel. LAS AF software was used for capturing images and they were further processed with the FIJI software.

2.19.1 Image processing with FIJI

The image processing was made using the free software FIJI. The nuclei were determined first and a mask was created from the Hoechst staining and overlaid to the other IF-channels. For this reason, only staining in the nuclei could be measured.

For intensity measures, this FIJI script was used:

```
//This macro is used for quantifying intensity within the nuclear masks
image = getTitle();
roiManager("reset");
run("Clear Results");
run("Split Channels");
selectWindow("C1-"+image);
waitForUser("Please adjust brightness and contrast");
run("Median...", "radius=10");
setAutoThreshold("Mean dark");
run("Convert to Mask");
run("Watershed");
run("Analyze Particles...", "size=50-Infinity display exclude clear add");
selectWindow("C2-"+image);
run("Set Measurements...", "area integrated redirect=None decimal=3");
run("Clear Results");
roiManager("deselect");
roiManager("Measure");
waitForUser("Please copy data from the result table for nuclear intensity");
run("Close All");
print("finish analyzing "+image);
```

For foci count, this FIJI script was used:

```
//This macro is used for quantifying number of foci within the nuclear masks
image = getTitle();
roiManager("reset");
run("Clear Results");
run("Split Channels");
selectWindow("C1-"+image);
waitForUser("Please adjust brightness and contrast");
```

Materials & Methods

```
run("Median...", "radius=5");
setAutoThreshold("Default dark");
//setThreshold(54, 255);
run("Convert to Mask", "method=Default background=Dark black");
setOption("BlackBackground", true);
run("Convert to Mask");
run("Fill Holes");
run("Watershed");
run("Analyze Particles...", "size=50-Infinity display exclude clear add");
selectWindow("C2-"+image);
run("Duplicate...", "title=foci");
run("Threshold...");
waitForUser("Please select appropriate threshold for RPA foci");
run("Find Maxima...", "prominence=10 output=[Single Points]");
run("Clear Results");
roiManager("deselect");
roiManager("Measure");
waitForUser("Please copy data from the result table for number of foci");
run("Close All");
print("finish analyzing "+image);
```

2.20 Statistical Analysis

Statistical analysis was performed using GraphPad Prism 7TM. For microscopy assays where staining intensity per cell was measured, a Mann-Whitney test of at least 100 nuclei was performed. This test is used to compare distributions of populations. For microscopy assays where foci number per cell was measured, a Student's t-test of at least 100 nuclei was performed. This test is specific to compare medians of two populations.

3. Results

This work focuses on the more detailed characterization of Myo6 in the DNA repair pathway HDR and the resulting biological consequences upon loss of Myo6. Throughout this thesis, all characterization is based on A549 *wildtype* cells, abbreviated as WT, A549 Myo6 *knockout* cells, abbreviated as KO, HeLa *wildtype* cells, abbreviated as HeLa WT, and HeLa Myo6 *knockout* cells, abbreviated as HeLa KO. *Knockdowns* are also performed in both cell lines, abbreviated as A549 KD or HeLa KD.

In my master-thesis all experiments were carried out upon CPT as DNA damaging agent. CPT is inhibiting topoisomerase I and therefore also creating replication stress. To strictly distinguish the work on DSBs from our work on replication stress, all previous experiments were repeated with NCS as damaging agent. NCS is creating DSBs through ROS and can be used as analogue to IR. All following experiments were performed once with NCS and once with CPT.

3.1 Characterization of Myo6 in Homology Directed Repair

To confirm the survival defect upon Myo6 depletion is dependent on DSBs and not on replication stress, a colony formation assay (CFA) upon a 1 h treatment of 5 µg/ml and 50 µg/ml NCS was performed.

In the literature, there are two forms of CFA where cells are treated either before or after plating. Thereafter, the procedure is identical, the cells are kept in culture for approximately two weeks and the ability to form colonies is visualized after staining with crystal violet. The technique of plating out before treatment was the one used in my master's thesis and is mainly applied to the general survival of cells after DNA damage^{84,85}. Whereas the plating after treatment technique is mainly used to observe DNA repair and subsequent survival. It is applied to study lethal- and sub-lethal damage repair. By re-plating after damage, cells have time to repair the DNA damage, but if repair mechanisms are disrupted, this can lead to cell death and thus, less colony formation on the plate⁸⁴. Since my question was related to DSB repair, I chose this method of colony formation assay in which the cells are first treated and then plated. The result is shown in Figure 6A. A549 KO cells show a clear reduction in survival compared to WT cells. This means that upon Myo6 depletion and after DNA damage, a smaller number of cells survive. With this different version of the assay, the experiment was also performed using different concentrations of CPT and the same phenotype was observed (Figure S1). This demonstrates that the survival defect in Myo6 KO cells is not caused by replication stress but by direct DNA damage, such as DSB formation.

Results

For F-actin, it was shown that it has a role in DSB mobility, shown by RAD52 foci mobility assays²⁰. To validate if Myo6 is also involved in this very late step of HDR, I started to investigate Rad51 as a marker protein.

The first step was to establish immunofluorescence (IF) staining with RAD51 specific antibodies. The final protocol included the steps of treatment with 1 μ M CPT or 0.5 μ g/ml NCS for 1 h, pre-extraction (to wash away unbound protein), and fixation. Cells were then incubated with primary RAD51 antibody followed by the corresponding secondary antibody and Hoechst. The evaluation was, after acquiring the microscopy images, performed with FIJI (Fiji is just imageJ). In order to include only the foci in the nucleus in the evaluation, a nucleic mask was created using the Hoechst staining which was then overlaid to the RAD51 channel. To tell the software which spot is a focus and which staining is just background, I set a threshold that remained constant for each experiment. This analysis is shown as a dot plot in Figure 6B. Each dot represents the RAD51 foci number of one nucleus. In this experiment, untreated WT and KO cells were compared to cells treated with 0.5 μ g/ml NCS for 1 h and then recovered for 8 h. In the untreated condition, the number of foci per nucleus was very low and there was no difference between WT and KO cells. Whereas KO cells had a significantly lower number of RAD51 foci per cell than WT cells in the NCS condition. Some exemplary cells are shown in the representative images to the right of the graph. This phenotype was also observed in cells treated with 1 μ M CPT (Figure S1). From these experiments, it can be concluded that Myo6 depletion, similar to actin polymerization inhibition, impaired the late stage of HDR pathway. In order to find the step of HDR in which Myo6 is involved, marker proteins upstream in the cascade were investigated. One step further upstream is phosphorylation of RPA (Figure 4). After 1h of 0.5 μ g/ml NCS treatment, total nuclear pRPA (S33) signal was analysed (Figure 6C). Damage-induced pRPA intensity was significantly lower in KO cells, compared to WT cells. This is also shown in the representative images, next to the graph. That means that HDR is already impaired in the step of RPA phosphorylation when Myo6 is depleted and upon CPT or NCS treatment.

One step further upstream in the pathway is RPA loading onto ssDNA (Figure 4). To investigate on RPA loading, another IF approach was performed with a similar protocol as for Rad51. An adjustment was made for pre-extraction buffer and RPA specific antibodies were used (Figure 6D). After NCS treatment, cells show a higher number of RPA foci, especially WT cells. In comparison, KO cells show a lower number of RPA foci per nucleus. This assay demonstrates that depletion of Myo6 leads to impaired HDR even at early stages.

Results

RPA foci are an indirect marker for resection, as RPA binds rapidly and with high affinity to ssDNA. However, to detect resection impairment, a more direct readout was performed. To visualize ssDNA after DNA damage induction, cells were treated for 24h with 10 ng/ml BrdU. Then, cells were treated with 0.5 $\mu\text{g/ml}$ NCS for 1 h, pre-extracted and fixed. To be then stained with BrdU specific antibodies (Figure 6C). Upon DSB induction, by NCS treatment, there is less BrdU intensity in Myo6 KO cells, compared to WT cells. This indicates that less ssDNA is exposed in KO cells compared to WT cells suggesting that deletion of Myo6 already negatively affects long-range resection during HDR.

To confirm this phenotype, the general DDR was also investigated in the form of phosphorylation of histone variant H2AX. These experiments were performed to test if the DDR in WT and KO cells is different. For this purpose, cells were treated for 1 h with 0.5 $\mu\text{g/ml}$ NCS, fixed and stained with γH2AX specific antibodies and Hoechst (Figure 6C). In contrast to all other markers previously tested, there was no difference between WT and KO cells after damage induction. This shows, that the general DDR is not impaired at the step of H2AX phosphorylation. Taken together (Figure 6A-F) I could demonstrate that HDR pathway is negatively affected by depletion of Myo6 during long-range resection and downstream. This was also shown upon inhibition of actin polymerisation^{19,20}.

To test if there was a delay in the kinetics of KO cells, kinetics of γH2AX and pRPA were performed (Figure 6G, H). Cells were treated for 1h with 0.5 $\mu\text{g/ml}$ NCS, then washed and released for indicated time points. After fixation, cells were stained with γH2AX or pRPA specific antibodies and Hoechst (Figure 6C, F).

Both kinetics show no difference in the time course of the build-up and resolution of the markers. However, in the pRPA kinetics, it can be noticed that the pRPA intensities per nucleus are lower in KO than in WT. This was already observed previously at the time point after one hour (Figure 6C).

In summary, there are no differences in kinetics between WT and KO cells, but the HDR repair markers show a reduction in KO cells compared to WT cells. This suggests no defect in overall repair of DSBs in Myo6 KO cells, but a defect specifically in markers for HDR. This indicates a reduced usage of HDR pathway upon Myo6 depletion.

Results

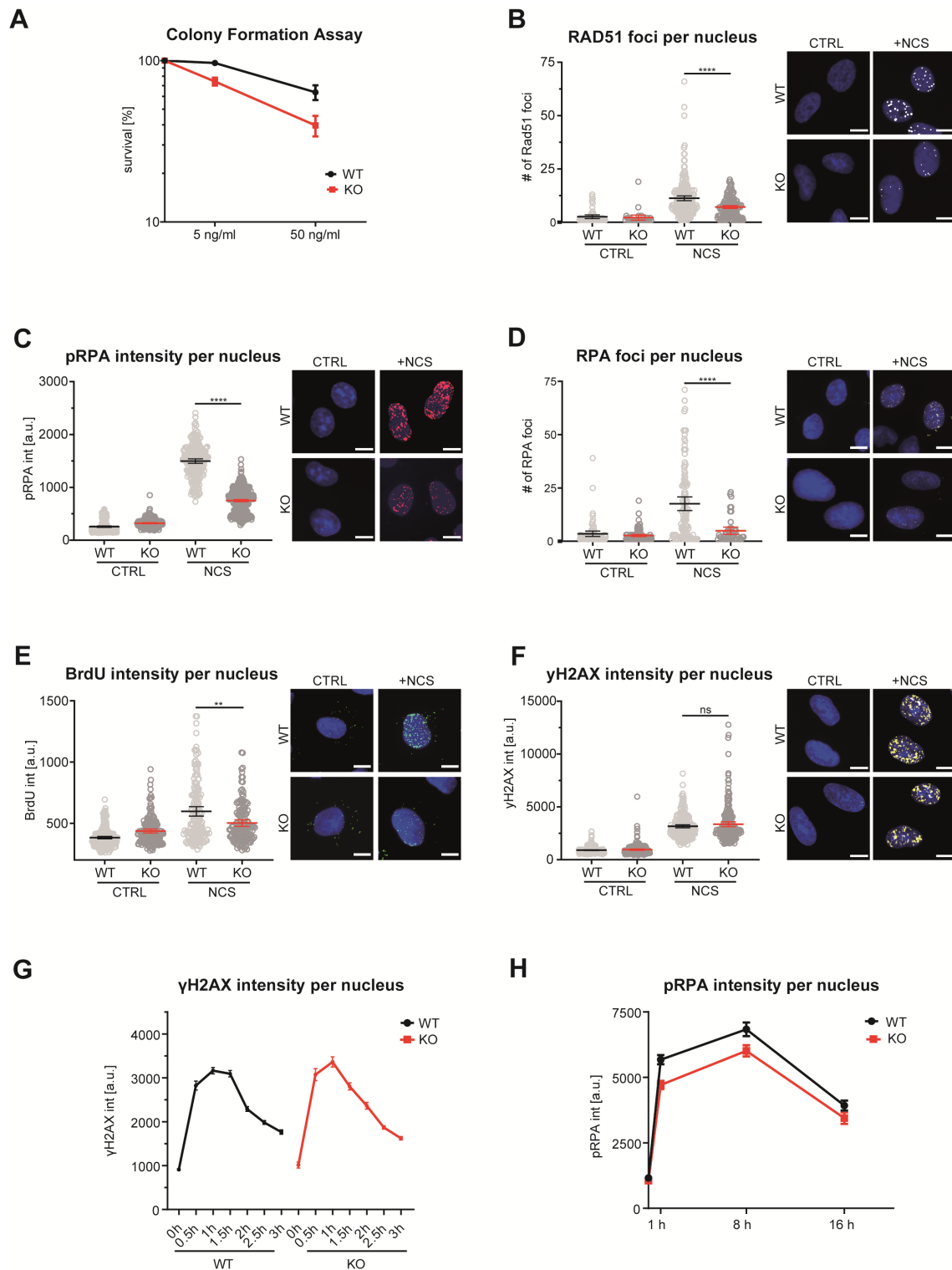


Figure 6: Knockout of Myo6 results in impaired survival and decreased HDR marker levels upon DNA damage

A549 wildtype (WT) and Myo6 knockout (KO) cells were treated with 0.5 mg/ml neocarzinostatin (NCS) for 1 h (A-H). All replicates are shown in Figure S2.

(A) Colony Formation Assay show lower survival in KO cells. Cells were treated with indicated concentrations of NCS and then reseeded (in triplicates) into 10 cm petri dishes. After 10 days, they were counted manually. The graph shows mean and standard error of the mean (SEM) of three independent experiments.

Results

(B) Rad51 immunofluorescence staining (IF) shows a lower foci number in KO cells. After treatment, cells recovered for 8 hours and were then stained with Rad51-specific antibodies. Left: dot plots of number of Rad51 foci per nucleus with mean values \pm 95% confidence intervals. Significance levels were calculated using the students t-test from at least 100 nuclei per sample (ns: non-significant, ****: $p < 0.0001$, ***: $p < 0.001$, *: $p < 0.05$). Right: representative images with Hoechst staining in blue and Rad51 signals in white. A representative experiment from three independent replicates is shown. Scale bar = 10 μ m

(C) pRPA (S33) IF shows lower pRPA intensity in KO cells. After treatment of 1h, cells were stained with pRPA (S33) specific antibodies. Left: dot plots of pRPA intensity per nucleus with mean values \pm 95% confidence intervals. Significance levels were calculated using the Mann-Whitney test from at least 100 nuclei per sample (ns: non-significant, ****: $p < 0.0001$, ***: $p < 0.001$, *: $p < 0.05$). Representative images with Hoechst staining in blue and pRPA signals in red are shown. A representative experiment from three independent replicates is shown. Scale bar = 10 μ m

(D) RPA IF shows less RPA foci in KO cells. IF staining was performed as shown in (C) with RPA specific antibodies. The properties of the graph are the same as in (B). Representative images with Hoechst staining in blue and RPA signals in orange. A representative experiment from three independent replicates is shown. Scale bar = 10 μ m

(E) BrdU IF shows less BrdU intensity in KO cells. After a 24 h pre-treatment with 10 ng/ml BrdU, cells were treated with NCS, pre-extracted and following stained with BrdU specific antibodies. The properties of the graph are the same as in (C). Representative images with Hoechst staining in blue and BrdU signals in green. A representative experiment from three independent replicates is shown. Scale bar = 10 μ m

(F) γ H2AX IF showed no difference between WT and KO cells. IF staining was performed as shown in (C) with γ H2AX specific antibodies. The properties of the graph are the same as in (C). Representative images with Hoechst staining in blue and γ H2AX signals in yellow. A representative experiment from three independent replicates is shown. Scale bar = 10 μ m

(G) γ H2AX IF kinetics show no differences between WT and KO cells. At 0 h timepoint, NCS was added and after 1h cells were washed and the γ H2AX foci resolution was monitored. The graph shows the mean with SEM. A representative experiment from two independent replicates is shown for each IF experiment.

(H) pRPA (S33) IF kinetics show no delay in KO cells, but a decrease in pRPA (S33) intensity. At 0 h timepoint, NCS was added and after 1 h it was removed and the decrease of pRPA (S33) was monitored. The graph shows the mean with SEM. A representative experiment from three independent replicates is shown for each IF experiment.

3.2 Confirmation of RPA phenotype due to Myo6 loss

To make sure that no artificial effects or signaling problems of a single cell clone cause the observed phenotype, RPA foci formation was tested in different cell lines and upon KO of Myo6 and KD. In addition, both NCS and CPT were used to induce DNA damage. All experiments in Figure 7 are performed using the same staining protocol and analytical methods as for the RPA foci in Figure 6.

In A549 cells, KD of Myo6 (siMyo6) led to reduced RPA foci per nucleus upon NCS (Figure 7A) and CPT (Figure 7B) treatments compared to control (siCTRL). The reduction of RPA foci upon Myo6 KD and KO after DNA damage could also be observed in HeLa cells (Figure 7C-F). These experiments show that the resection-impaired phenotype in Myo6 depleted cells was stable in both A549 and HeLa cell lines. Moreover, the phenotype was observed under KO and KD conditions and upon different types of DNA damage induction.

3.3 RPA phenotype upon actin polymerization inhibition

Next, it was addressed if Myo6 and F-actin are involved in the same pathway by epistasis analyses. Therefore, A549 WT and KO cells were pretreated with DMSO or CK666 for 30 minutes and subsequently treated with 0.5 $\mu\text{g/ml}$ NCS or 1 μM CPT. CK666 is a small molecule inhibitor that inhibits the ARP2/3 complex, which is important for actin filament formation. The staining protocol and evaluation were performed as before.

WT cells treated with DMSO show an increase in RPA foci per cell upon DNA damage compared with untreated cells (Figure 7G). Inhibition of actin polymerization by CK666 reduced NCS-induced RPA foci in WT cells. KO cells treated with DMSO show a reduction in RPA foci per nucleus compared to WT cells treated with DMSO. Inhibition of actin polymerization in KO cells resulted in no difference for RPA foci number compared with CK666 treated WT cells. This is neither the case for NCS nor for CPT (Figure 7G, H).

This experiment shows an epistatic effect between F-actin and Myo6, which indicates that both proteins act in the same pathway.

Results

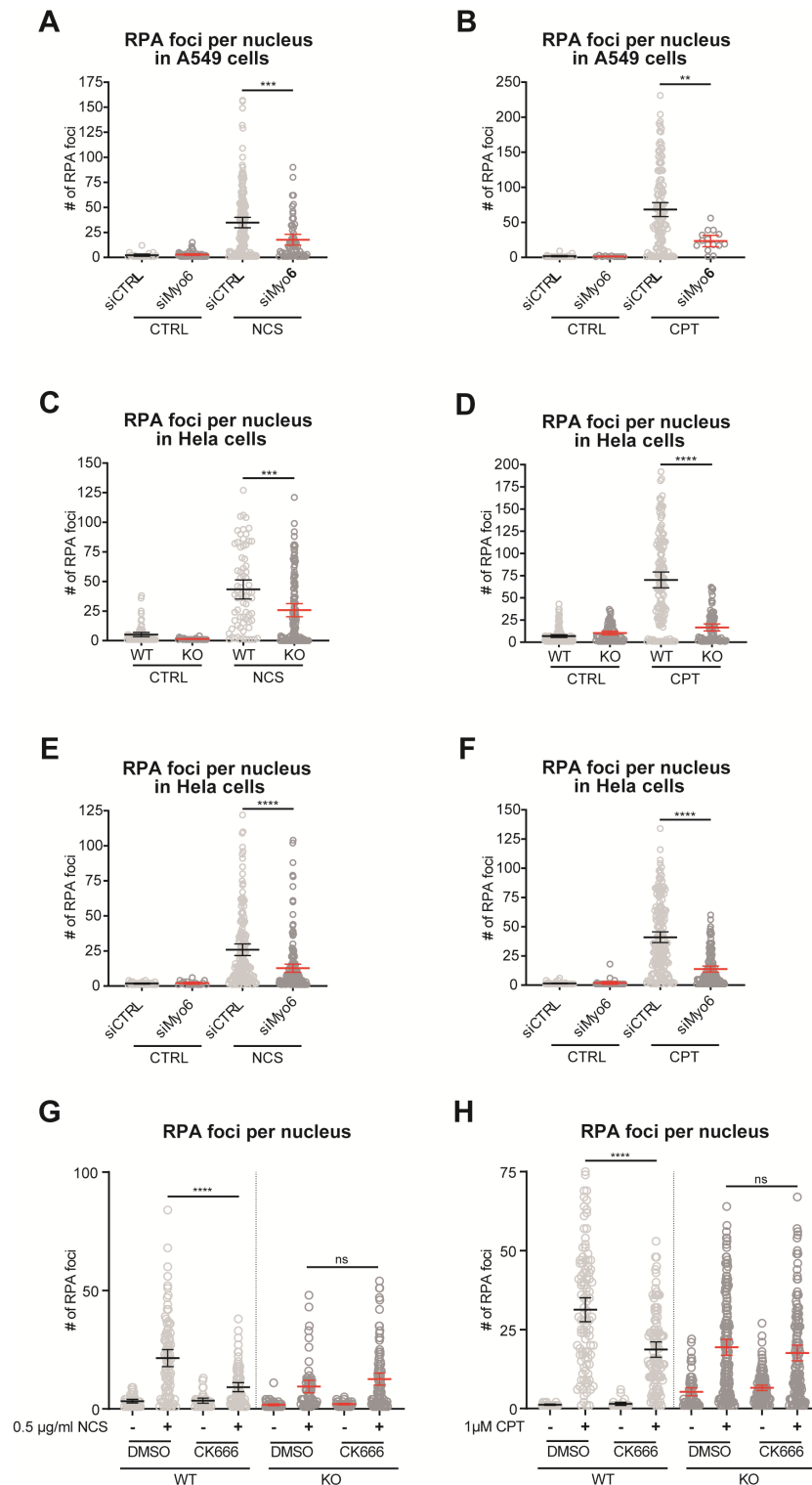


Figure 7: RPA phenotype is conserved in A549 / HeLa cells after KO or KD upon CPT and NCS
 (A-B) A549 WT cells show reduced RPA foci number after KD of Myo6 upon CPT and NCS. A549 WT cells were treated with siRNA control (siCTRL) and siRNA Myo6 (siMyo6). DNA damage was induced (as indicated) with NCS or CPT. After treatment of 1h, cells were pre-extracted, fixed and stained with RPA specific antibodies. Dot plots show number of RPA foci per nucleus with mean values \pm 95% confidence intervals. Significance levels were calculated using the students t-test from at least 100 nuclei per sample (ns: non-significant, ****: $p < 0.0001$, ***: $p < 0.001$, *: $p < 0.05$). A representative plot of three independent replicates is shown. Replicates are shown in Figure S3. KD efficiency is shown in Figure S 4.

Results

(C-D) HeLa cells show reduced number of RPA foci after Myo6 KO, upon NCS and CPT. DNA damage to HeLa WT and KO cells was induced (as indicated) with NCS or CPT. The staining and evaluation were performed as in (A-B). Replicates are shown in Figure S3.

(E-F) HeLa WT cells show reduced RPA foci number after KD of Myo6 upon CPT and NCS. HeLa WT cells were treated with siRNA control (siCTRL) and siRNA Myo6 (siMyo6). DNA damage was induced (as indicated) with NCS or CPT. The staining and evaluation were performed as in (A-B). Replicates are shown in Figure S3. KD efficiency is shown in Figure S 4.

(G-H) A549 cells show epistasis upon Myo6 KO and CK666 treatment after NCS or CPT treatment. A549 WT and KO cells were pre-treated with DMSO or CK666 for 30 minutes and then treated with CPT or NCS to induce DNA damage. The staining and evaluation were performed as in (A-B). Replicates are shown in Figure S5.

3.4 Cell cycle analysis

Now that Myo6 has been shown to be important for HDR and cell survival, we asked if Myo6 mediates these phenotypes through regulating the cell cycle. This part of the study focuses on cell cycle analysis of CPT damaged WT and KO cells by flow cytometry.

3.4.1 Myo6 KO show no cell cycle slow down upon DNA damage

To analyze the cell cycle progression of CPT damaged cells, cells were primary labeled with EdU. EdU is a base analogue that is only incorporated by S-phase cells. Thus, the EdU-positive cells are those that were in S phase at the time of labelling. Since CPT only causes DNA damage to cells in S phase, this means that the labeled cells are also the subsequently damaged cells.

In Figure 8A, the cell cycle profile of WT (blue) and KO (red) cells upon CPT treatment is shown. Cells were pre-treated with EdU for 30 min, treated with 1 μ M CPT for 1 hour, then fixed or released into CPT- and EdU-free medium for the indicated time points. After fixation of all time points, a click reaction with Click-iT® Plus EdU Alexa Fluor® 647 imaging kit (Invitrogen) was performed and the cells were additionally stained with DAPI.

The cell cycle profile in CTRL and 1 h were identical between WT and KO cells. However, 4 hours after treatment, KO cells showed a slightly greater number of cells in mid/late S phase than WT cells, which means that they progress faster. After 8 h and 16 h, this effect was no longer visible and the cell cycle profiles of WT and KO cells are again comparable. In Figure 8B and C the two-dimensional cell cycle profiles and the gating strategy are shown. The EdU positive cells are shown in a histogram diagram in Figure 8D. WT cells are shown in magenta and KO cells in purple. After 1 h CPT, both cell types displayed a similar distribution of S phase cells. After 4 h the KO cells continued to mid / late S phase, while WT cells slowed down cell cycle progression. This is a well-known phenotype in which damaged cells slow down the cell cycle to repair the damage before moving on to the next cell cycle phase. However, the checkpoints responsible for this slowdown, such as pRPA (shown in Figure 6C, H), were

Results

reduced in KO cells, which may explain why they did not slow down their cell cycle as much as WT cells. After 8 h and 16 h, the distribution of the S phase cells had aligned again between WT and KO.

3.4.2 Tracking CPT damaged cells to the next cell cycle phase

Another interesting technical aspect was to follow these labeled and damaged cells to next cell cycle. After observing the drastic survival defect in Myo6 depleted cells, it was interesting to see whether the cells could move on to the next cell cycle at all. This experimental approach, first had to be established with untreated cells in order to observe their behavior.

For establishment, cells were labeled with EdU, for indicated times, fixed and following stained with DAPI. After a 30-minute EdU pulse, the signal was clearly detectable in S-phase cells (Figure 8E). 4 h after the treatment the labeled cells moved on to late S and G2 phase. At the final time point, after 8 hours, only a few cells were still detectable in the G2 phase, but the signal from the majority of cells faded. This signal loss can be explained by cell division. When the cells have incorporated EdU and divide, the DNA and thus the EdU signal is divided in half. Thus, all cells entering the next cell cycle are no longer detectable by the EdU signal. This problem could not be solved by increasing concentration of EdU.

To solve this problem, it was tested to give a 1 h EdU pulse. Indeed, prolonged pre-incubation with EdU enabled us to follow the cells to the next G1 phase. This is shown in Figure 8E in the lower graph. The cells moved from S phase (30 min) to late S / G2 phase (4 h) and after 8 h half of the cells were still in G2, but the other half made it to next G1.

This approach would be very useful to track the labeled/damaged cells in WT and compare them with Myo6 depleted cells. It could answer the question of whether the cells die directly or whether they first go into cell cycle arrest.

Results

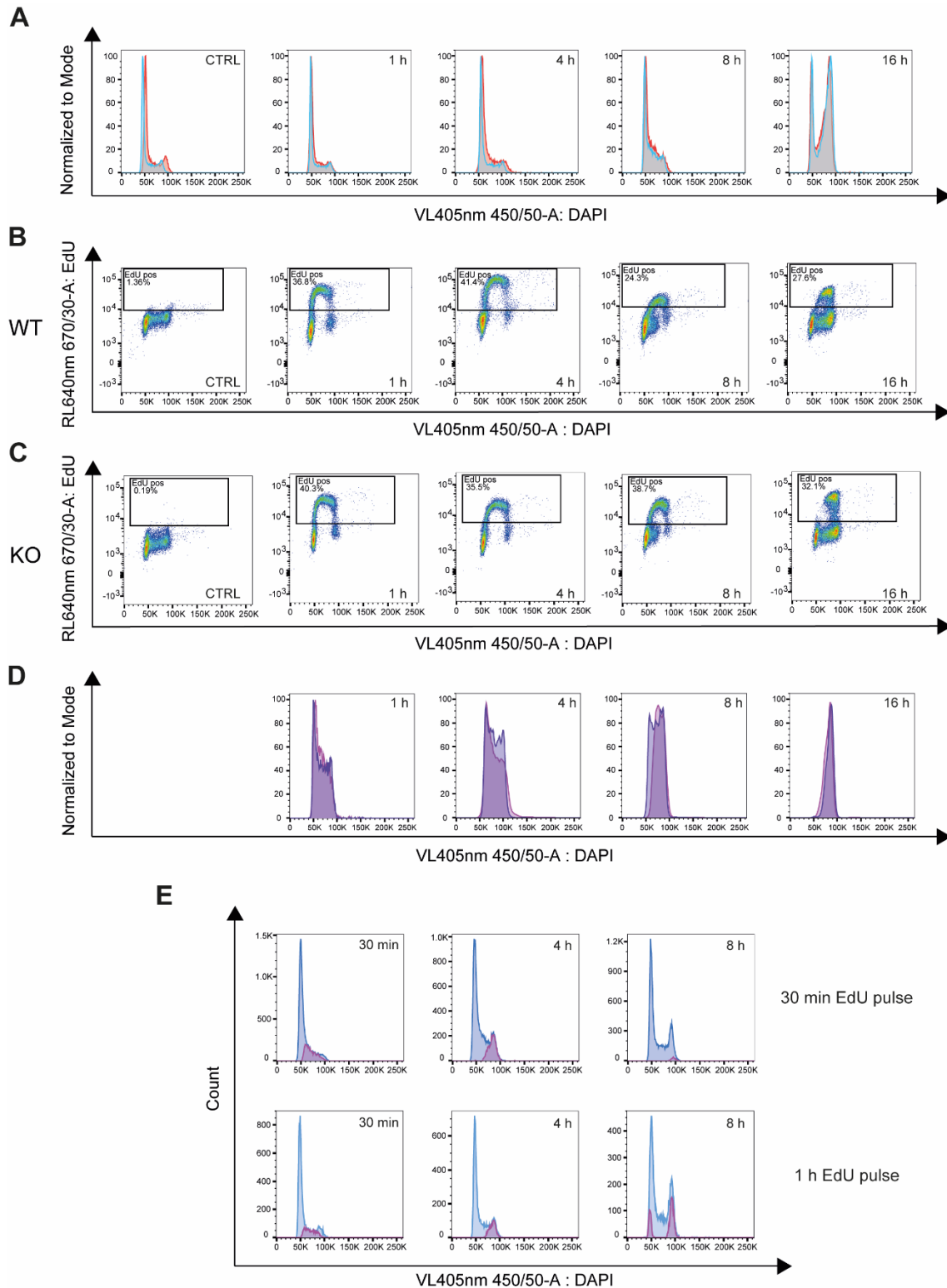


Figure 8: Myo6 depletion leads to different behaviour in cell cycle progression in A549 cells upon CPT treatment

A549 WT and KO cells were treated for 20 min with 10 μ M EdU, next 1 μ M of CPT was added for 1 h. Cells were then washed with PBS, harvested and fixed in PFA (1h) or released in fresh medium for 4h, 8h and 16h and harvested and fixed in PFA. Staining was performed using DAPI and EdU click reaction and evaluated using Flow cytometry. The number of WT and KO cells was adjusted to each other. Each plot shows one representative plot from three independent experiments. Replicates are shown in Figure S 6. (A-D)

(A) A549 KO cells show no cell cycle slow down upon CPT treatment. Cell cycle profile overlay of A549 WT (blue) and KO (red) cells at indicated timepoints.

Results

(B-C) Two dimensional cell cycle profile is shown. Plots are examples of the gating strategy for A549 WT EdU positive (B) and KO EdU positive (C) cells. At least 10,000 single cells were analyzed.

(D) Overlay of EdU positive WT (magenta) and EdU positive KO (purple) cells.

(E) After 1 h EdU pulse, it is possible to follow the S phase cells to the next cell cycle. The cell cycle profile of A549 WT cells, treated for indicated time with EdU. Cells were washed with PBS, harvested and fixed in PFA 30 minutes, 4 h or 8 h after treatment start. Staining were performed using DAPI and EdU click reaction and evaluated using Flow cytometry. The number of WT cells was adjusted to each other and at least 10,000 single cells were analyzed.

3.5 Degradation Systems for Myo6

Myo6 is predominantly present in the cytoplasm and only a very small pool is located in the nucleus. Due to this distribution of cytoskeletal proteins, it is always essential to study if the phenotype is triggered by the depletion of the nuclear pool. To adequately answer this question, different approaches were tested to deplete Myo6 in a compartment specific manner.

3.5.1 Single cell clone characterization for 2-RING system

To target Myo6 highly specific and with a high affinity in the cell Designed Ankyrin Repeat Proteins (DARPin) were used. These are specific binders that can bind a wide variety of proteins with high specificity. In this thesis I used a DARPin that specifically binds Myo6 (G4) and a non-binding control DARPin (E3_5)³¹.

The first approach was to test depletion of Myo6 by using a proteasomal degradation system. The ARMeD (Antibody RING-mediated destruction) degradation system can deplete the overall pool of the antibody targeted protein in the cell⁸⁶. The RING domain of RNF4 was fused to a DARPin targeting Myo6 (or a non-binding DARPin, E3_5, as control). Following, using lentiviral transduction, it was brought into A549 WT cells. After selection by hygromycin and single cell sorting, I tested the clones for doxycycline (DOX) inducible degradation of Myo6. The ARMeD plasmid also included a GFP tag, to check the expression levels of the construct. In the following, the ARMeD system is abbreviated as 2-RING.

Figure 9D shows a simplified schematic of the 2-RING system fused to different DARPins in the cell. Initially, construct expression was induced with DOX in approximately 50 clones and GFP levels were compared (representative clones shown in Figure 9A). A few clones from each expression level were selected to be evaluated in more detail. In the next step, the clones were still tested for GFP expression, but in addition also their Myo6 level - / + DOX (without / with construct expression) was compared. Here, only one Myo6-DARPin binding clone was found to display the desired behavior (Figure 9B). Clone #31 showed low (almost no) expression of

Results

the construct (as measured by GFP signal), which was expected since the construct would also be degraded during the Myo6 degradation process.

Addition of a proteasomal inhibitor (MG132) stabilized Myo6 level upon induction of the construct (+ DOX) (Figure 9C) suggesting that Myo6 is indeed degraded via the proteasome. For the non-binding control darpin (E3_5), clone #15 was chosen, with a medium-high expression level and no changes in Myo6 levels upon DOX induction.

Results

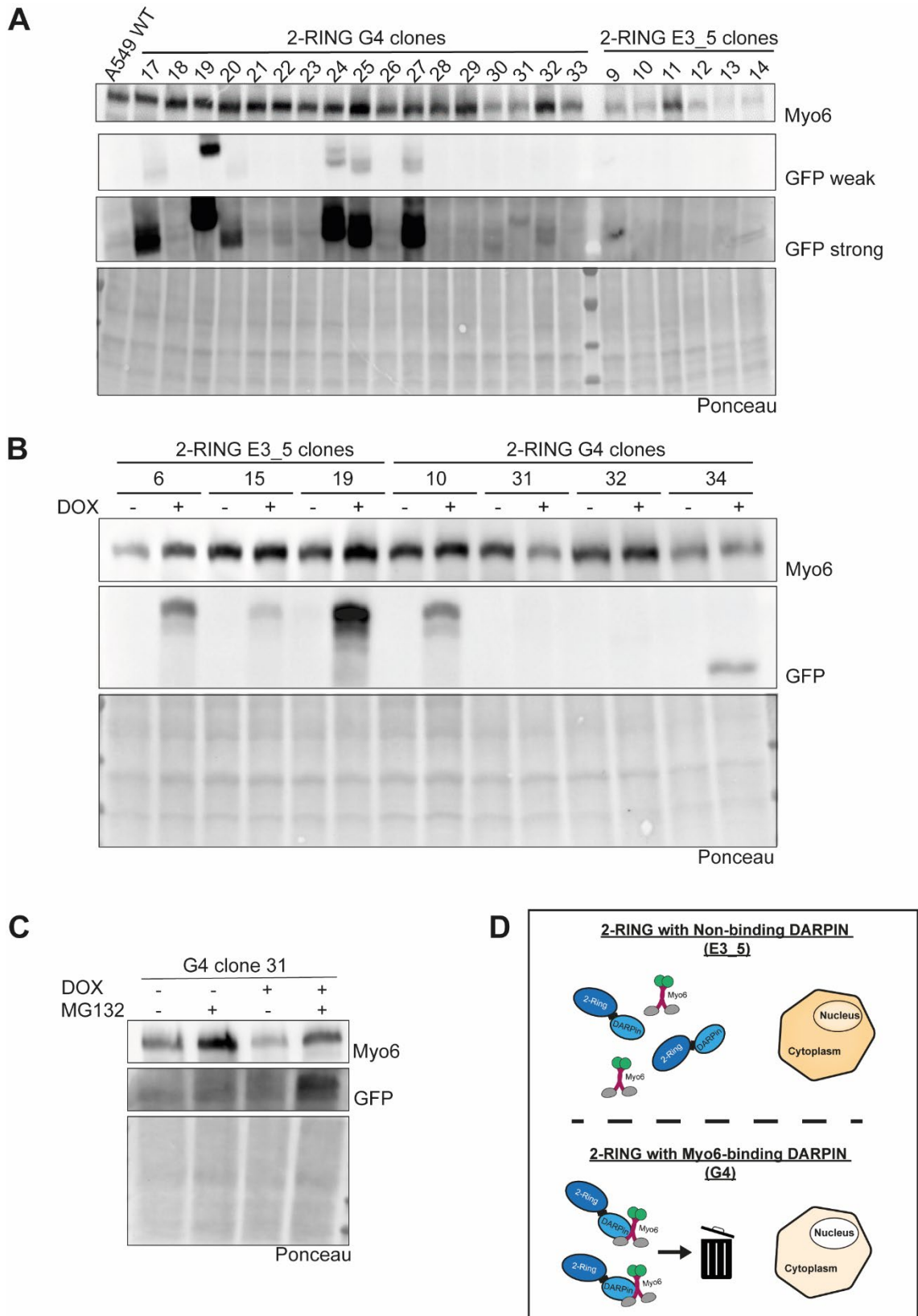


Figure 9: DARPin 2-RING-mediated destruction system testing for Myo6 depletion

To introduce the 2-RING into the cells, a lentiviral transduction was carried out in A549 WT cells with a non-binding control DARPin (E3_5) or a Myo6-binding DARPin (G4). After hygromycin selection single cell clones were generated and following tested for GFP expression level and Myo6 levels. (A-C)

Results

(A) Several 2-RING G4 clones show GFP expression, but E3_5 clones show none. 2-RING clones were incubated with 2 $\mu\text{g/ml}$ DOX for 16 h. Following, cells were lysed and analyzed by Western blotting using antibodies against GFP and Myo6. The membrane was additionally stained with Ponceau, as a loading control. Only one representative blot is shown here, about 30 clones each were tested.

(B) All 2-RING E3_5 clones show GFP expression upon 2 $\mu\text{g/ml}$ DOX treatment. Clone G4 #31 showed reduction of Myo6 level upon DOX induction. 2-RING clones were incubated - / + DOX for 16 h and following lysed and analysed by Western blot using GFP and Myo6 specific antibodies.

(C) Myo6 degradation in G4 clone #31 is proteasome dependent. SPOP G4 clone #31 was tested upon - / + MG132, as proteasomal inhibitor and - / + 2 $\mu\text{g/ml}$ DOX. DOX induction was for 16 h. Proteasomal inhibition, with 30 μM MG132 was started 4h before harvesting.

(D) Simplified schematic of 2-RING system in the cell.

3.5.2 Single cell clone characterization for SPOP system

Now that proteasomal degradation of Myo6 has been demonstrated using the 2-RING system, the next step was to degrade only the nuclear pool of Myo6 in a similar manner. For this purpose a SPOP (an adaptor protein of the Cullin-RING E3 ubiquitin ligase complex)⁸⁷ where the natural substrate binding domain was replaced with a Myo6 targeting DARPIn was used. This tool was used to demonstrate that our phenotype is caused by the depletion of the nuclear Myo6 pool. A simplified schematic is shown in Figure 10E. The cells were as well lentivirally transduced, selected by hygromycin and then single cell sorted. The GFP expression levels of about 50 clones were compared in the first step. Figure 10A, B shows examples of some of these G4 (Myo6-binding DARPIn) and E3_5 (non-binding DARPIn) clones. The selected clones, which were chosen based on their expression level, were tested using the RPA phenotype. Only a representative selection is shown in Figure 10C. The RPA foci number per cell was compared after 16 h of DOX induction for different clones - / + DOX and - / + CPT, as DNA damaging agent. Only clone #5 showed a reduction of damaged-induced RPA foci per cell upon SPOP induction. Once the phenotype was confirmed, clone #5 was examined by western blot for Myo6 levels after different lengths of induction with DOX (Figure 10D). A549 WT and KO Myo6 level were compared as well. After 16 h and 24 h of DOX induction, the cells showed a strong GFP signal, so the construct was expressed, but the overall Myo6 level was not changing. The latest time point, 48 h DOX induction, displayed an overall reduction of Myo6 level. This effect could be due to transport of Myo6 into the nucleus. In the literature, a recruitment of Myo6 into the nucleus after DNA damage has already been observed⁸⁸. After 48 h of degradation of Myo6 in the nucleus, cytoplasmic Myo6 could be recruited into the nucleus and also be degraded. Since this effect was not desired, as only the nuclear pool needed to be degraded, a DOX induction of 16 h was performed in following experiments. For the non-binding E3_5 DARPIn construct, clone #7 with similar expression level was chosen.

Results

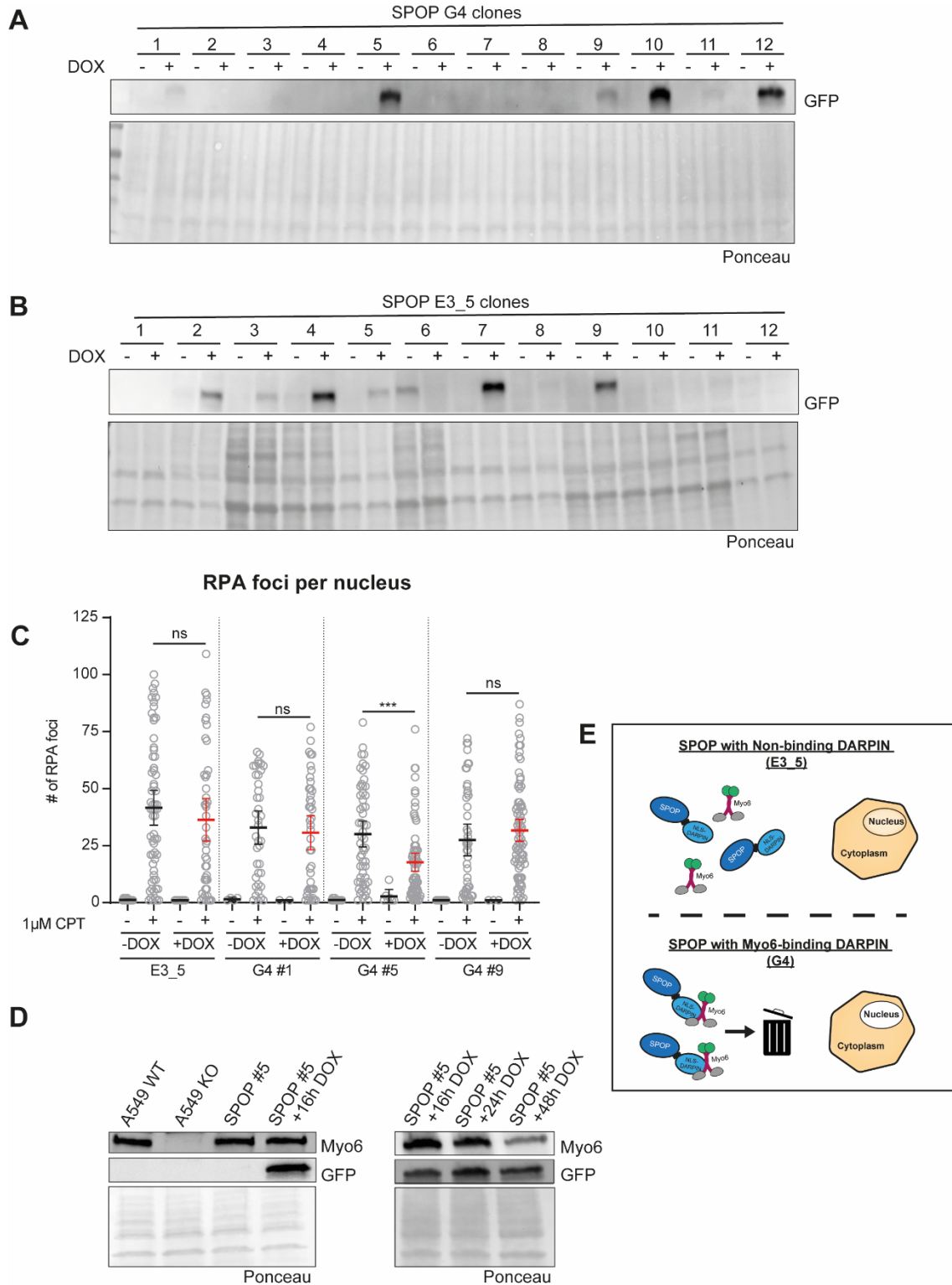


Figure 10: SPOP system for nuclear degradation of Myo6

To introduce the SPOP into the cells, a lentiviral transduction was carried out in A549 WT cells with a non-binding control DARPIN (E3_5) or a Myo6-binding DARPIN (G4). After hygromycin selection single cell clones were generated and following tested for expression level and RPA phenotype. (A-D)

(A) Clone #1, 5, 9, 10, 11, 12 show GFP expression of the construct. SPOP G4 clones were incubated - / + 2 μ g/ml DOX for 16 h to compare un-induced expression cells with induced ones. Following, cells were lysed and analyzed by Western blotting using antibodies against GFP. The membrane was additionally stained with Ponceau, as a loading control. Only one representative blot is shown here, about 30 clones were tested.

(B) Clone #2, 3, 4, 5, 7, 8, 11 display GFP expression of the construct. The procedure for SPOP E3_5 clones was the same as for SPOP G4 clones.

Results

(C) RPA foci per cell do not change in E3_5 clone after DOX induction, but decrease in clone #5. A549 clones were pre-treated with - / + 16 h 2 µg/ml DOX and treated next with - / + 1 µM CPT for 1 h. After treatment of 1h, cells were pre-extracted, fixed and stained with RPA specific antibodies. Dot plots show number of RPA foci per nucleus with mean values +/- 95% confidence intervals. Significance levels were calculated using the students t-test from at least 100 nuclei per sample (ns: non-significant, ****: p<0.0001, ***: p<0.001, *: p<0.05). A representative plot is shown.

(D) Induction of the SPOP system changes the total level of Myo6 only after 48 h. A549 WT, KO and SPOP clone #5 were evaluated here. A549 WT, KO and SPOP clone #5 were treated with 2 µg/ml DOX for indicated time points. Cells were lysed and analyzed by Western blotting using antibodies against GFP and Myo6. The membrane was additionally stained with Ponceau, as a loading control.

(E) Simplified schematic of SPOP system in the cell.

3.5.3 Nuclear vs Cytoplasmic Myo6 (SPOP, 2-RING, NLS)

Using selected clones for both the 2-RING and SPOP systems, final experiments were performed. These should validate that our phenotype is dependent on nuclear Myo6. In Figure 11A RPA foci number per nucleus in cells with the 2-RING system of non-binding DARPin (E3_5) or Myo6-binding DARPin (G4) is shown. The cells expressing 2-RING E3_5 showed no difference between - / + DOX upon CPT damage. The 2-RING G4 #31 clone displayed upon DOX induction a strong reduction of RPA foci in comparison to - DOX condition. That means, that upon proteasomal degradation of the Myo6 pool in the whole cell, RPA foci per nucleus were reduced. Thus the phenotype, observed before in KO cells (Figure 6D), was confirmed using a different degradation system. In Figure 11B RPA foci per nucleus are shown in SPOP system expressing cells. In the cells where SPOP is linked to E3_5, cells showed no significant difference upon - or + DOX treatment. The cells with a Myo6-binding DARPin displayed upon DOX induction a reduction of damaged-induced RPA foci per nucleus in comparison to un-induced cells. Since the SPOP system degrades only the nuclear pool and has no effect (after 16 h of induction) on the total Myo6 level in the cell, this indicates that the nuclear pool of Myo6 is responsible for the resection impaired phenotype.

As an alternative approach, it was examined whether depletion of the cytoplasmic Myo6 pool would influence the phenotype of RPA foci. For this purpose, an NLS-Myo6-binding DARPin (or the control DARPin E3_5) was expressed to relocate the cytoplasmic pool of Myo6 to the nucleus and thus deplete the cytoplasmic pool. This technique was also used in Shi *et al.*³¹ paper, but with U2OS cells. Without DOX induction, the U2OS cells showed a strong cytoplasmic Myo6 signal and almost no staining in the nucleus. After DOX induction, the U2OS cells showed predominantly signal in the nucleus and hardly any in the cytoplasm³¹. In A549 cells, however, the antibody displayed nonspecific binding in the nucleus in A549 cells already without DOX induction. Upon DOX induction most of the cytoplasmic Myo6 signal re-localized into the nucleus, but some Myo6 stayed cytoplasmic. That means that this construct

Results

was not able to localize the complete cytoplasmic pool of Myo6 into the nucleus (Figure 11E). In order to make more precise conclusions, the Myo6-DARPin NLS cell line would have to be further investigated in comparison to KD or KO cells, for example.

Nevertheless, in order to make a prediction with the help of the cell lines, several clones expressing the Myo6-DARPin-NLS construct were tested for RPA phenotype. In the experiment shown, the cells of the E3_5 cell line without DOX but with CPT treatment showed no increase of RPA foci per nucleus. However, this can only be attributed to this one experiment. In other experiments, the E3_5 cells without DOX with CPT treatment showed an increase in RPA foci per cell. In all of the tested clones of the Myo6-binding DARPin, no difference was seen between - and + DOX after CPT treatment (Figure 11C). As can be seen in Figure 11D, all cell lines expressed the construct. This Myo6 re-localization approach alone was not very strong evidence, as the localization of Myo6 was not complete. But, it is another indication that the phenotype after Myo6 depletion is not caused by the cytoplasmic loss of the protein.

In sum, all approaches in KO cells, in KD cells, in cells expressing the 2-RING construct and the final detection in cells expressing the SPOP construct, indicate strongly that the phenotype is due to the depletion of the nuclear pool of Myo6.

Results

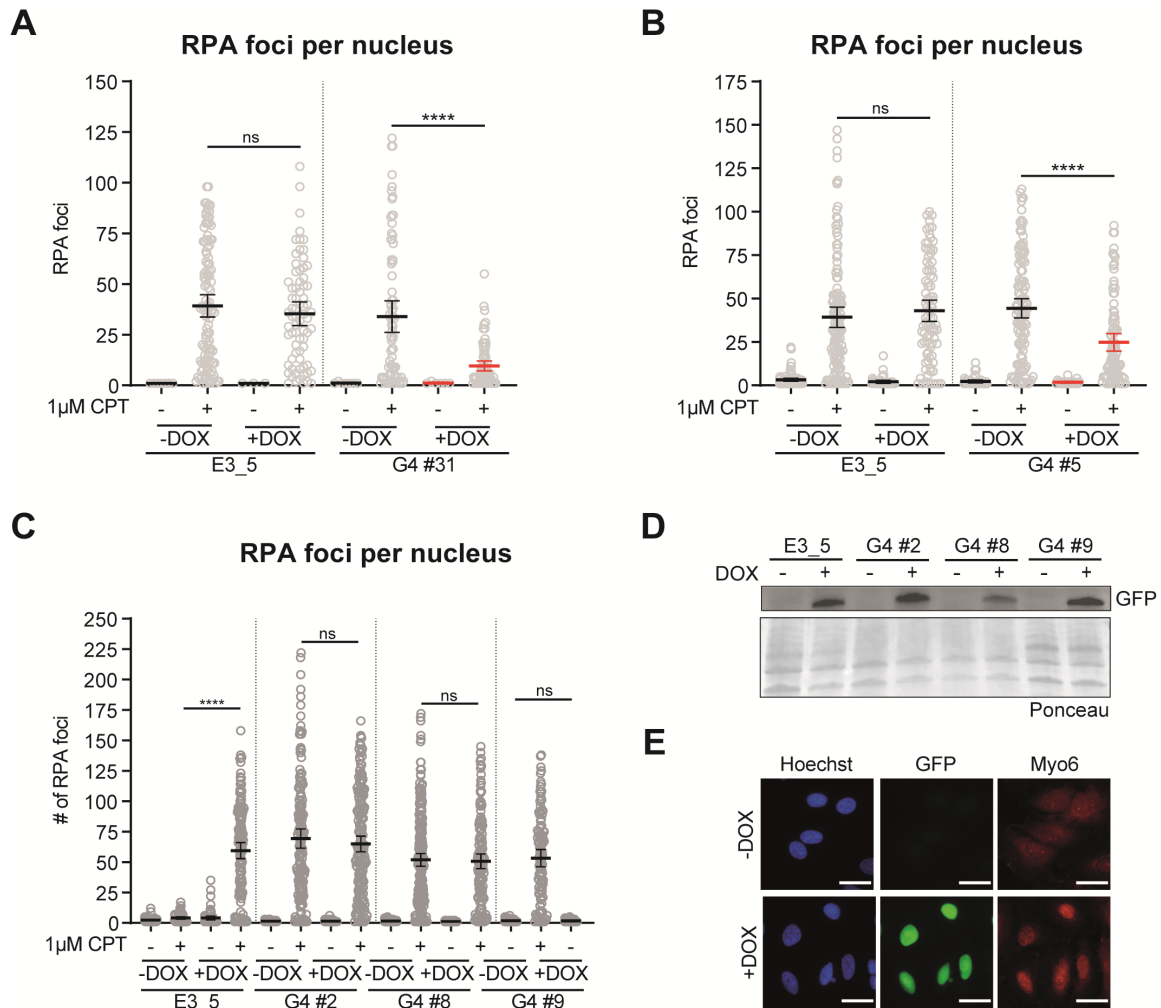


Figure 11: Different Myo6 degradation systems or re-localisation of Myo6

The constructs (2-RING, SPOP, NLS-DARPin) were brought into A549 WT cells using lentiviral transduction. For each cell line, a control DARPin (E3_5) and a Myo6 binding DARPin (G4) was transduced. Previously tested clones were pre-treated with -/+ 16 h 2 $\mu\text{g}/\text{ml}$ DOX and treated next with -/+ 1 μM CPT for 1 h. After treatment of 1h, cells were pre-extracted, fixed and stained with RPA specific antibodies. Dot plots show number of RPA foci per nucleus with mean values \pm 95% confidence intervals. Significance levels were calculated using the students t-test from at least 100 nuclei per sample (ns: non-significant, ****: $p < 0.0001$, ***: $p < 0.001$, *: $p < 0.05$). A representative plot of three independent experiments is shown. Replicates are shown in Figure S7. (A-C)

(A) 2-RING G4 clone #31 shows upon DOX, a significant decrease in RPA foci number per nucleus.

(B) SPOP G4 clone #5 shows upon DOX, a significant decrease in RPA foci number per nucleus.

(C) Myo6-NLS-DARPin cell lines show no difference in RPA foci upon DOX induction.

(D) All NLS-DARPin cell lines show GFP expression after 16 h DOX induction. Cells were treated for 16 h -/+ DOX, harvested and lysed. Next, they were analyzed using Western Blot with specific antibodies against GFP and stained with Ponceau as loading control.

(E) Representative images of Hoechst staining in blue, GFP signal in green and Myo6 signal in red of clone G4 #9. Scale bar = 25 μm

3.6 Further characterization of Myo6 role in HDR

Up to this point, I could show that Myo6 is involved in HDR. Its involvement is during resection or upstream of it. Our phenotype (of resection deficit) is very robust, also in different cell lines, and is most likely caused by depletion of the nuclear Myo6 pool.

This part of the thesis aimed to characterize Myo6 in the HDR pathway in more detail. In order to find new approaches for the involvement of Myo6, the previously performed mass spectrometry analysis were re-analyzed. Two groups of proteins that interact with Myo6 and are simultaneously involved in these early steps of HDR induction were identified. On the one hand, chromatin remodelers were found such as NAP1L1, RUVBL1/2, etc.³¹. During DSB repair the chromatin needs to be relaxed and remodeled to give access to repair proteins. This remodeling step is very important during resection and various chromatin remodelers are involved. On the other hand, KU70, KU80 and VCP were found³¹. These proteins are important for long-range resection, because KU70/80 needs to be removed by VCP before this process can start (Figure 4). In order to decide in which direction further research should be carried out (Figure 12A), initial experiments were performed.

3.6.1 Myo6 role in chromatin remodeling

To investigate the role of Myo6 in chromatin remodeling, KDs of a known chromatin remodeler were performed and then RPA phenotype was examined. This part of the project was carried out in collaboration with Katharina Spang from Dr. Sandra Schick laboratory from IMB. They provided me with siRNAs for subunits of the BRG1/BRM-associated factor (BAF) complex, which is a known chromatin remodeler. The two subunits investigated, SMARC-A4 and ARID-1A, are known to be involved in DNA end resection⁸⁹. Further, actin is an integral component of this complex and BAF can also bind F-actin⁹⁰. BAF subunits were not found in the mass spectrometry screen of Myo6 interactors, but since it is known to be involved in resection and interacts with F-actin, I decided to test this chromatin remodeling complex.

In the first step I tested KD efficiency of siSMARC-A4 and siArid-1A. Upon KD with siSMARC-A4 off-target effects were observed, so I decided to continue the experiments only with ARID-1A siRNA. In Figure 12B a control KD (siCTRL), a Myo6 KD (siMyo6), an ARID-1A KD (siArid-1A) and a double KD of Myo6 and ARID-1A were performed, to investigate if depletion of both proteins would have an additional effect on RPA foci per nucleus or if it would be an epistatic effect. In comparison to siCTRL, the individual KDs and the double-KD showed a significant reduction in RPA intensity. However, no significant difference was measured between the individual and double KD. This suggests Myo6 and ARID-1A were epistatic. Since

Results

it is known for the BAF complex to be involved in resection and I could show the same phenotype upon Myo6 depletion this is a further confirmation about Myo6 role in resection, potentially in interaction with the BAF complex or another chromatin remodeling complex.

3.6.2 Myo6 role in KU70/80 removal

The other approach was to investigate Myo6 in the process of KU70/80 removal. For this purpose, A549 WT and KO cells were treated with 10 Gy IR and harvested at indicated time points. Next, cells were pre-extracted, to only have chromatin bound proteins left, and analyzed by western blot. The Western blot showed clearly, that there was more bound KU70 at the chromatin in KO cells, compared to WT cells.

Due to this drastic effect I observed in the initial experiments of chromatin bound KU70/80, I decided to investigate if Myo6 is involved in KU70/80 removal from chromatin, potentially explaining its role in resection.

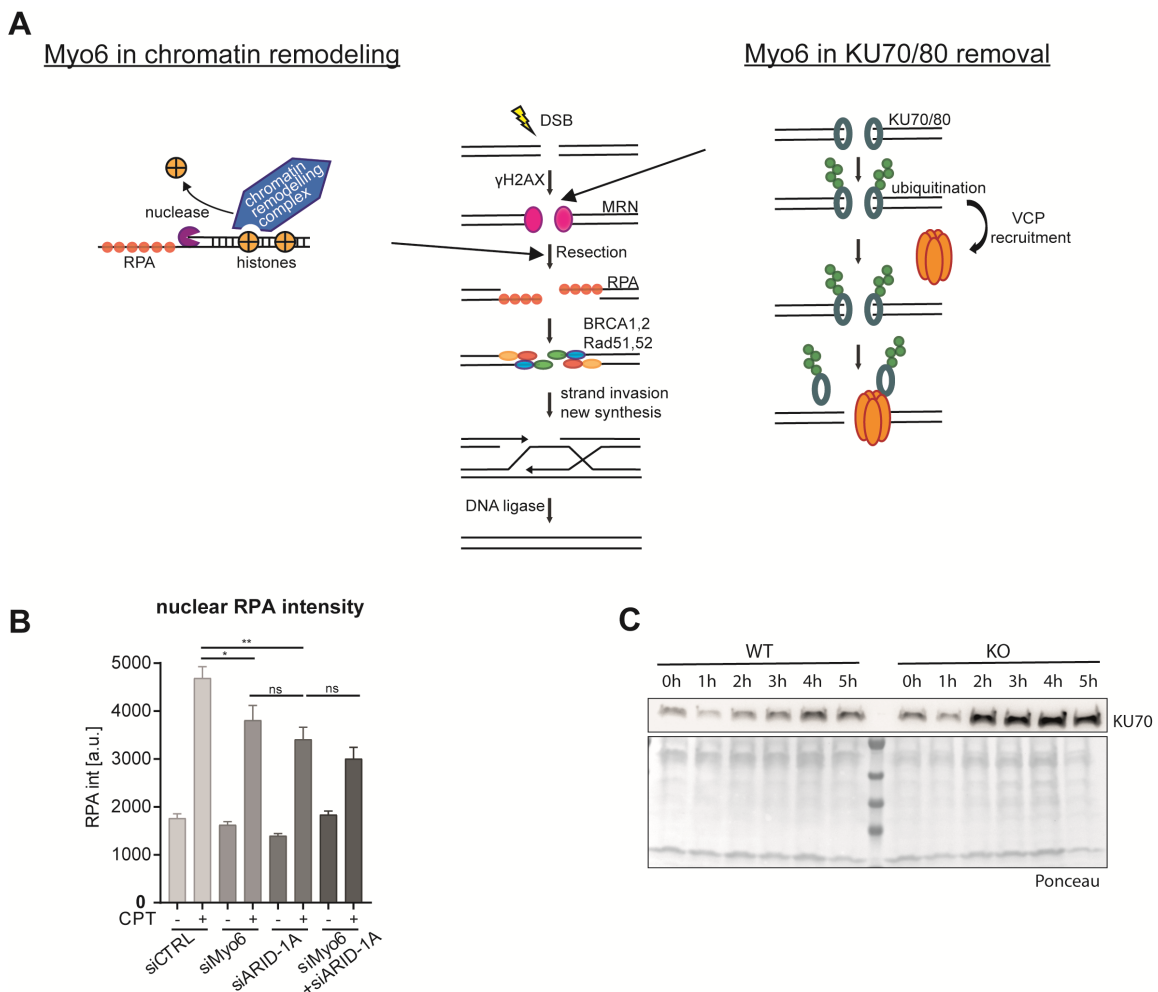


Figure 12: Myo6 in chromatin remodelling vs Myo6 in KU70/80 removal

Results

(A) Schematic representation of the HDR pathway with possible sites of Myo6 involvement. According to mass spectrometry data, one potential group of Myo6 interactors are chromatin remodelers, another group are proteins involved in KU70/80 removal from DSB sites.

(B) Double KD of Myo6 and ARID-1A shows no additional effect on RPA foci reduction. A549 WT cells were treated with siCTRL, siMyo6, siARID-1A or siMyo6 and siArid-1A. After that, DNA damage was induced using 1 μ M of CPT for 1 h or cells were left untreated. After pre-extraction and fixing, cells were stained with RPA specific antibodies and Hoechst. The bar diagram shows the RPA intensity per nucleus with mean values \pm 95% confidence intervals. Significance levels were calculated using the students t-test from at least 100 nuclei per sample (ns: non-significant, ****: $p < 0.0001$, ***: $p < 0.001$, *: $p < 0.05$).

(C) Chromatin bound KU70 is greatly enriched in Myo6 depleted cells. A549 WT and KO cells were treated with 10 Gy IR and then released to recover by the indicated time points. After collection of all timepoints, cells were pre-extracted with CSK B buffer and following lysed. Cell lysate was analyzed using Western blot with KU70 specific antibodies and Ponceau as loading control. Due to the pre-extraction, only chromatin-bound proteins remain.

3.7 KU70/80 staining optimization

A well-established and more quantitative approach than the western blot is to examine chromatin bound KU70/80 by performing microscopy assays with KU70/80 foci. The staining itself is quite complex as the foci are very fine, because there is only one complex at each DSB end. Due to these challenges in staining, the staining had to be optimized first in order to achieve reliable results in my hands.

Britton *et al.* published an often cited staining protocol for KU70 and KU80 foci⁴⁵. Initially, I tested the staining exactly according to the protocol and tried to reproduce the results. For this, cells were treated with 10 Gy IR, pre-extracted including RNase and then fixed. Next, the cells were stained with KU70 specific antibodies and Hoechst. In Figure 13A the total KU70 intensity per nucleus - / + 10 Gy IR and - / + RNase is shown. In the – RNase condition, the chromatin bound KU70 was highly enriched after IR treatment, which was expected. In comparison, the RNase treated samples showed lower values upon IR treatment. This can be explained by the fact that KU70/80 also binds to RNA in the cell. But since only chromatin-bound KU70/80 was of interest for this study, the RNase treatment was included in my protocol. By only looking at the nuclear KU70 intensity graphs, the results from Britton *et al.* were reproducible. But Figure 13B shows a section of cells with the corresponding KU70 staining. The KU70 antibody created an enormous background due to unspecific binding, which could falsify the evaluation.

To get rid of the background, another antibody specific for KU80 was tested with the same staining protocol as used before (+RNase). In Figure 13C the KU80 intensity per nucleus is displayed in a time course of the first hour after 10 Gy IR treatment. A small increase of chromatin bound KU80 was displayed up to 10 min and following a small decrease up to 1 h. Unfortunately, the background signal in the untreated cells was also very high, which almost

Results

masked the effect. This could be also observed in example images in Figure 13D. There were no fine, distinct foci, the staining was spread over a large area in the nucleus. Nevertheless, significantly less non-specific binding outside the nucleus was observed as with the KU70 antibody, which is why the following optimization was continued with the KU80 antibody.

In the next step, the staining protocol needed to be adapted to A549 cells. To reduce the background, first a double pre-extraction was tested. In the original protocol the cells were pre-extracted for 5 minutes, now it was tested if an additional 5 min pre-extraction with the same buffer after the first pre-extraction would reduce the background. The result is shown in Figure 13E. The background reduced upon this second pre-extraction step, but still there were no distinct foci.

Another approach to improve the staining was, to change the secondary antibody. In Figure 13F are example images for this test. The result was an increase of KU80 intensity, but still a lot of background staining in the nucleus.

The final test was to increase the Triton-X concentration from 0.7 % to 1 % to better permeabilize the cells and allow the pre-extraction buffer to enter the nucleus more easily. The result is shown in Figure 13G. This increase in Triton-X concentration greatly improved staining and solved the background problem. The nuclei showed fine, distinct KU80 foci after IR treatment. These foci could be quantified well and reliably, as the plot in Figure 13H shows. The following experiments were performed with this optimized staining protocol for KU80 foci in A549 cells.

Results

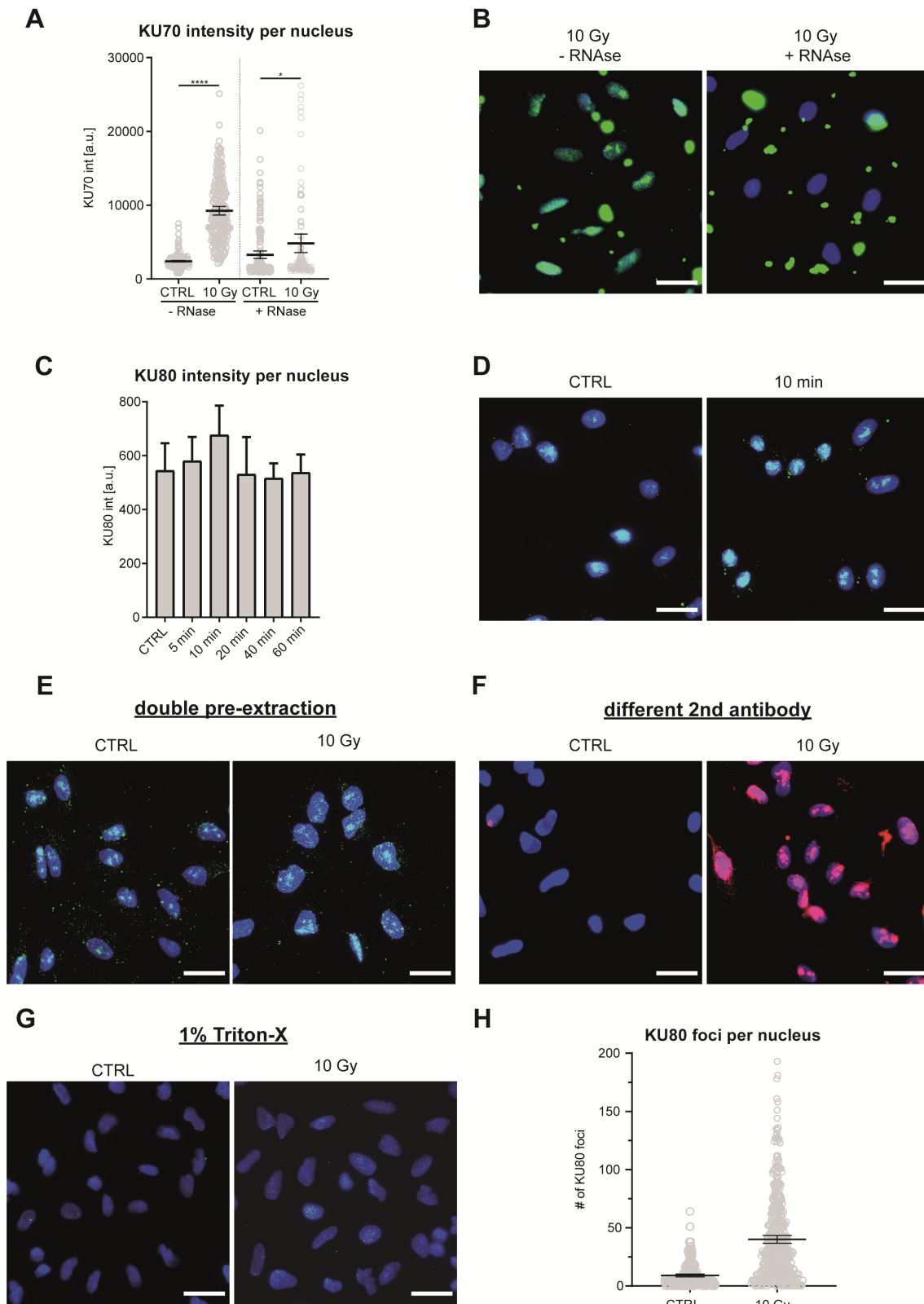


Figure 13: KU foci Optimization

(A) KU70 staining results from Britton *et al.* are reproducible. A549 WT cells were irradiated with 10 Gy IR, pre-extracted with CSK B buffer with 0.7 % Triton-X - / + RNase, fixed and stained with KU70 specific primary antibodies, Alexa488 tagged secondary antibodies and Hoechst. Dot plot show KU70 intensity per nucleus with mean values \pm 95% confidence intervals. Significance levels were calculated using the students t-test from at least 100 nuclei per sample (ns: non-significant, ****: $p < 0.0001$, ***: $p < 0.001$, *: $p < 0.05$). (A-B)

Results

(B) Representative images of experiment (A) are shown here. KU70 is shown in green and Hoechst in blue. Scale bar = 25 μ m

(C) KU80 foci per cell show an increase upon 10 Gy IR treatment and a decrease over time. A549 WT cells were irradiated with 10 Gy IR, pre-extracted with CSK B buffer with 0.7 % Triton-X + RNase, fixed and stained with KU80 specific primary antibodies, Alexa488 tagged secondary antibodies and Hoechst. Bar diagram shows KU80 intensity per nucleus with mean values \pm 95% confidence intervals. Significance levels were calculated using the students t-test from at least 100 nuclei per sample (ns: non-significant, ****: $p < 0.0001$, ***: $p < 0.001$, *: $p < 0.05$). (C-D)

(D) Representative images of experiment (C) are shown here. KU80 is shown in green and Hoechst in blue. Scale bar = 25 μ m

(E) KU80 staining has a high nuclear background upon double pre-extraction. Representative images of KU80 (green) and Hoechst (blue) stained cells after a double pre-extraction. Cells were treated as before in (C), with the difference that after pre-extraction cells were again incubated for 5 minutes in pre-extraction buffer. Scale bar = 25 μ m

(F) KU80 staining has a high nuclear background when stained with Alexa647 coupled secondary antibody. Representative images of KU80 (red) and Hoechst (blue) stained cells after staining with an Alexa647 tagged antibody. The procedure was performed as in (C) with the difference of a differently labeled secondary antibody (Goat anti-Mouse IgG (H+L) Secondary Antibody, Alexa Fluor 647). Scale bar = 25 μ m

(G) KU80 foci are distinct and very fine after pre-extraction with CSK B buffer with 1 % Triton-X. Representative images of KU80 (red) and Hoechst (blue) stained cells. The staining procedure was carried out as in (C), but the concentration of Triton-X was increased from 0.7 % to 1 %. Scale bar = 25 μ m

(H) KU80 foci number per cell increases after 10 Gy of IR. Staining was performed as in (G). Dot plot show number of KU80 foci per nucleus with mean values \pm 95% confidence intervals.

3.8 Myo6 involvement in KU70/80 removal

After optimizing the KU70/80 staining, the experimental setup was used to investigate chromatin-bound KU70/80 when Myo6 was depleted. A549 WT and KO cells were tested in parallel, with VCP inhibition as additional positive control, (Figure 14A, B). Since VCP extracts KU70/80 from chromatin (Figure 4), it was expected that KU70/80 should remain bound to chromatin after inhibition of VCP.

A549 WT cells treated with DMSO showed an increase in chromatin-bound KU80 after 10 Gy IR and a decrease in the subsequent time course. After 4, h the cells were back to control level of KU80 foci per nucleus. WT cells, treated with VCP inhibitor, showed as well an increase of KU80 foci per nucleus after 10 Gy of IR, but up to 4 h after treatment, the cells showed only a very small decrease in KU80 foci per nucleus. This means that KU70/80 was not efficiently extracted from DSB ends upon VCP inhibition. The Myo6 depleted cells showed similar behavior as the VCP-inhibited cells, an increase in chromatin-bound KU80 after IR, but no decrease in KU80 foci up to 4 hours after treatment. Representative images are shown in Figure 14B.

All experiments up to this point in summary demonstrate an involvement of Myo6 in the HDR pathway. In particular, in the HDR pathway, after short-range resection during the extraction of KU70/80 from chromatin. This is summarized graphically in Figure 14C.

Results

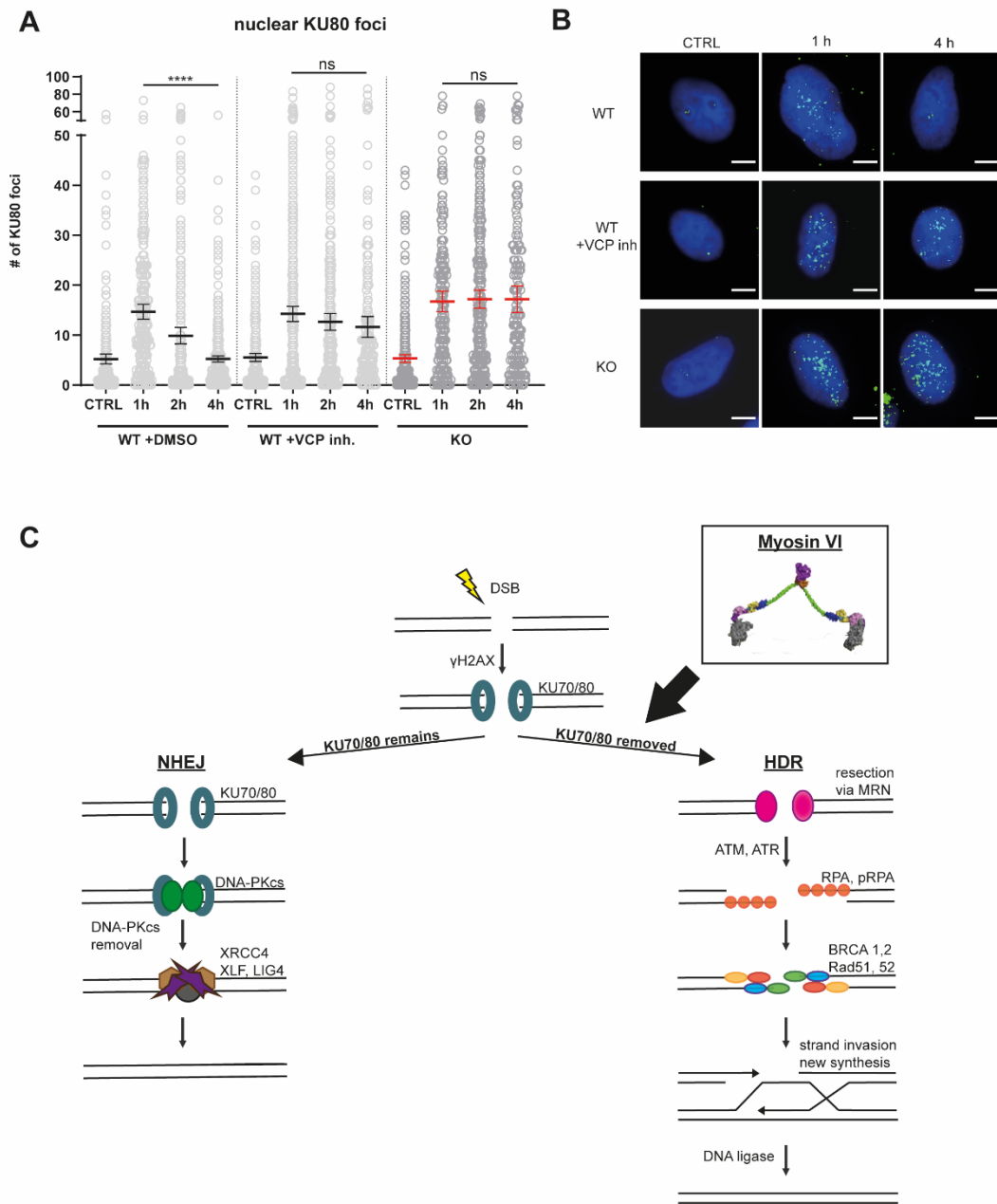


Figure 14: Myo6 in KU70/80 removal

(A) A549 KO cells show no KU80 foci resolution up to 4 h after IR damage. A549 WT cells were 15 minutes pre-treated with 0.1 % DMSO or 5 μ M VCP inhibitor (inh) (NMS-873). All cell lines were then irradiated with 10 Gy IR and then released into fresh medium with / without DMSO or VCP inh for indicated timepoints. When all timepoints were collected, cells were pre-extracted, fixed and stained with KU80 specific antibodies and Hoechst. Dot plot show KU80 foci per nucleus with mean values \pm 95% confidence intervals. Significance levels were calculated using the students t-test from at least 100 nuclei per sample (ns: non-significant, ****: $p < 0.0001$, ***: $p < 0.001$, *: $p < 0.05$). A representative plot of three independent experiments is shown. Replicates are shown in Figure S8. (A-B)

(B) Representative example images of KU80 staining (green) and Hoechst (blue) for graph (A) is shown. The Scale bar is 10 μ m

(C) Schematic summary of Myo6 involvement in HDR pathway is shown. The Myo6 scheme is adapted from Mukherjea *et al.*, 2009¹⁹

3.9 Biological consequences in form of Senescence

In the main part of this thesis I demonstrated, that Myo6 is involved in one of the most important DSB repair pathway in human cells. Damaging DNA in Myo6 depleted cells resulted in a survival defect (Figure 6A & Figure S1A). The question is now, what other biological consequences does a repair defect in cells have? Upon a chronic DDR response from unrepaired DSBs, the cells initiate senescence. In this part it is going to be investigated, if Myo6 plays a role in DNA damage-induced senescence.

3.9.1 Generation of inducible Myo6 depletion stable cell lines

This study has so far used cancer- derived cell lines to investigate the role of Myo6 in HDR. In the following, primary cell lines are used for the study of senescence. Human lung fibroblasts in form of WI-38 and IMR-90 cell lines and human foreskin in form of BJ cells were tested. To facilitate the *knockdown* of Myo6 and to reduce the stress on the cells, stable cell lines were generated that deplete Myo6 in an inducible manner. This was performed using a lentiviral transduction. An empty vector (EV), a small hairpin RNA (shRNA) targeting an untranslated region (UTR) of Myo6 and an open reading frame (ORF) of Myo6 were transduced. The shRNA on the plasmid targeted different sites of Myo6 to silence it or not. Upon this procedure, all WI-38 cells died. Most of the transduced IMR-90 cells died as well, but some of the UTR and ORF cells survived and they could get expand. The BJ cells, showed almost no cell death after transduction and cell lines of all three constructs were generated. During the selection with hygromycin, I observed that the surviving cells displayed morphological changes. The cell shape changed to small, round cells that appeared almost senescent, but proliferated very quickly. It is possible that the stress during lentiviral transduction harmed the cells or that the plasmids were integrated into the genome at sites of essential genes, or that the inducible system was leaky and caused the changes in the cells. There were many possibilities as to the cause of the abnormalities, but no reliable experiments could be carried out with these altered cells. For this reason, the following experiments were all performed upon a conventional KD with Lipofectamine™ RNAiMAX.

3.9.2 Characterization of senescence markers upon Myo6 depletion

In the initial experiments, the response of the primary cells to the KD procedure with Lipofectamine 2000 was investigated. BJ cells showed no morphological changes or increased cell death upon Myo6 depletion. Whereas, no WI-38 cells survived Myo6 KD. To further investigate on that, KDs were performed in both cell lines in parallel and Myo6 and p53 levels

Results

were compared. In BJ cells, Myo6 KD reduced the endogenous Myo6 pool and p53 levels showed no changes (Figure 15A). The WI-38 cells showed an efficient Myo6 depletion, but p53 was greatly enriched upon Myo6 KD. This may indicate that the cells were inducing programmed cell death (apoptosis) upon Myo6 depletion.

Since already in the stable cell line generation process, IMR-90 cells and WI-38 cells were more sensitive and this experiment showed major changes in p53 level of WI-38 cells, the following experiments were performed in BJ cells.

The β -galactosidase activity is one of the most commonly used senescence markers. Since senescent cells show increased β -galactosidase activity and this activity can be easily measured by substrate turnover. A control and Myo6 KD were performed in BJ cells and cells were treated with or without 10 Gy IR to induce senescence. After 10 days of recovery, cells were stained for β -Galactosidase activity (Figure 15C). The control KD cells showed IR-induced distinct black spots in the cytoplasm, which represent an increased activity of β -Galactosidase compared to untreated cells. Myo6 depletion, without IR treatment, resulted in a higher β -Galactosidase activity than in control KD cells. After 10 Gy IR treatment the Myo6 depleted cells showed a higher β -Galactosidase activity than treated control KD cells. These microscopy images were then analyzed by eye. The percentage of cells showing β -galactosidase activity was determined (Figure 15B).

This indicates that upon Myo6 depletion without any external damage, cells already show senescence associated phenotype. To confirm this, the β -Galactosidase activity was measured with another kit, which directly quantified the activity using a microplate reader for analysis (Beta Galactosidase Activity Assay Kit, BioVision). The experiment showed a very high background that tends to mask the effect (Figure 15D). Still, a significant increase of β -Galactosidase activity was measured in siCTRL and siMyo6 cells upon damage induction. When comparing the untreated samples, it was again evident that the Myo6 depleted cells showed a significant increase in β -Galactosidase activity. The treated samples also showed a significant increase in activity in Myo6-depleted cells. These experiments used two different approaches to show that primary cell lines exhibit senescence-associated phenotypes after knocking down Myo6.

In general, senescence can be triggered by p53/p21Cip1 or p16Ink4a/RB pathways⁷³. In both cases, the stable growth arrest is induced through cyclin/cyclin-dependent kinase (CDK) inhibition. P21 inhibits the kinase activity of CDK1 and p16 inhibits kinase activity of CDK4/6^{91,92}. By inhibiting these kinase activities, the transition from G1/S phase is altered, so

Results

both proteins are potent cell cycle inhibitors. Upon senescence induction, p16 and p21 are upregulated.

In the next step, it was investigated, if these two senescence marker show changes upon Myo6 depletion. After KD, 10 Gy IR treatment and 10 days of recovery, the cells were stained with p16 specific antibodies. The evaluation shows the intensity of p16 per nucleus and representative example images (Figure 15E). Both, control and Myo6 KD cells, showed an increase in p16 intensity upon 10 Gy IR. When comparing the two untreated cell types, there may was a minimal increase in p16 intensity in Myo6-depleted cells. Since the sample of cells was too small and the experiment was only carried out once, no reliable conclusions can be drawn from this. Only a slight tendency can be detected.

For p21 intensity comparison, the same procedure was carried out as for p16 intensity comparison, using a p21 specific antibody for staining. In Figure 15G the dot plot and representative example images are shown. The untreated cells showed no difference in p21 intensity per nucleus between control and Myo6 KD. After 10 Gy IR, KD cell populations showed an increase in p21 intensity per nucleus to the same extent. Control KD cells and Myo6 KD cells thus behaved the same.

Since Myo6 depletion triggers a senescence-associated phenotype in at least one senescence marker (β -Galactosidase activity), it was interesting to study what happens to general DNA damage markers upon Myo6 depletion in primary cell lines. I hypothesized that upon Myo6 depletion, DSB repair is impaired and cells might accumulate DNA damage, inducing through this pathway senescence.

3.9.3 Characterization of damage marker upon Myo6 depletion

For the investigation of general DNA damage in Myo6-depleted primary cell lines, γ H2AX and 53BP1 were chosen as established markers. KDs were performed in BJ cells and already two days after KD, the cells were stained with γ H2AX and 53BP1 specific antibodies. In general, Myo6 is so abundant in the cell that it takes three days for the pool to be mainly degraded. However, already upon incomplete KD of Myo6 (after 2 days), the cells showed a drastic increase of γ H2AX foci per cell (Figure 15F). The same effect was observed for 53BP1 foci per nucleus (Figure 15H). That means, that upon Myo6 depletion DNA damage accumulated in the cells and this might explain the increase of β -Galactosidase activity. The cells accumulate DNA damage in the absence of Myo6, DDR might be constantly activated and the cells might induce senescence upon this trigger.

Results

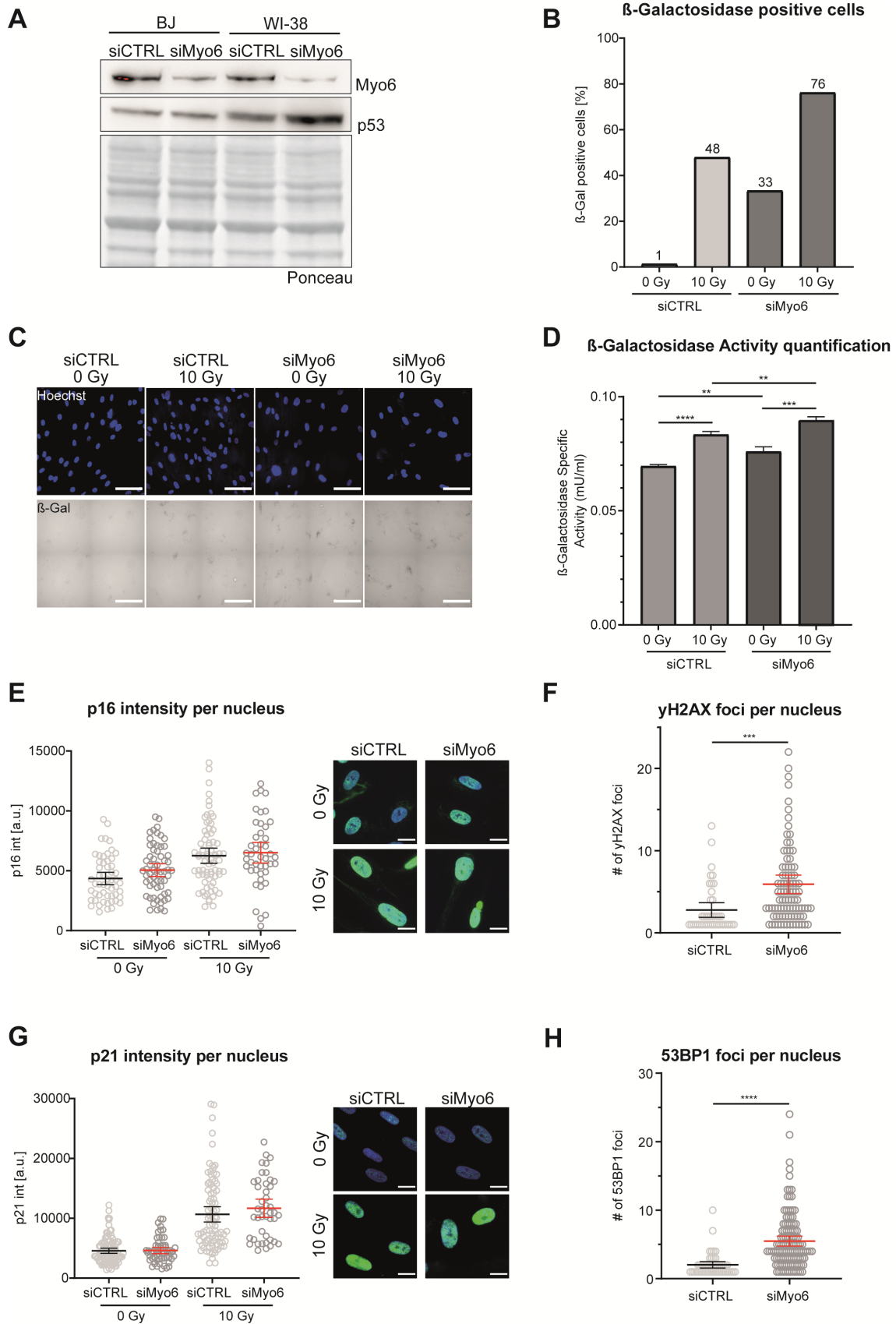


Figure 15: Myo6 role in senescence

(A) W-38 cells show activation of p53 upon Myo6 KD. A control and a Myo6 KD was performed in BJ and WI-38 cells. After three days of recovery, the cells were harvested, lysed and analyzed by Western blot. The membrane was stained with Myo6 and p53 specific antibodies and Ponceau as loading control.

Results

(B) Myo6 depletion results in more β -Gal positive cells than control KD. BJ cells were seeded and allowed to recover overnight. The next day a control and Myo6 KD was performed. After three days of recovery, the cells were treated - / + 10 Gy IR and the cells were recovered for 10 days. β -Galactosidase activity staining was performed according to Senescence β -Galactosidase Staining Kit (MERCK). After staining, β -galactosidase positive cells were counted manually. The graph shows % of β -Galactosidase positive cells - / + 10 Gy IR from one experiment.

(C) Example images for (B) are shown here. Scale bar = 100 μ m

(D) Myo6 KD leads to increased β -Gal activity in BJ cells. A control and Myo6 KD was performed in BJ cells. After three days, the cells were treated - / + 10 Gy IR and following staining and quantification was performed according to Beta Galactosidase (β -Gal) Activity Assay Kit (BioVision).

(E) p16 immunofluorescence staining (IF) shows no differences between control KD and Myo6 KD. BJ cells were seeded and allowed to recover overnight. The next day a control and Myo6 KD was performed. After three days of recovery, the cells were treated - / + 10 Gy IR and were recovered for 10 days. After that time, cells were stained with p16 specific antibodies. Left: dot plots of p16 intensity per nucleus with mean values \pm 95% confidence intervals. Significance levels were calculated using the students t-test from at least 50 nuclei per sample (ns: non-significant, ****: $p < 0.0001$, ***: $p < 0.001$, *: $p < 0.05$). Right: representative images with Hoechst staining in blue and p16 signals in green. Scale bar = 10 μ m

(F) γ H2AX foci are increasing 2 days after Myo6 KD in BJ cells. Control KD and Myo6 KD was performed in BJ cells. After two days, cells were fixed and stained with γ H2AX specific antibodies and Hoechst. Dot plots of number of γ H2AX foci per nucleus with mean values \pm 95% confidence intervals. Significance levels were calculated using the students t-test from at least 100 nuclei per sample (ns: non-significant, ****: $p < 0.0001$, ***: $p < 0.001$, *: $p < 0.05$).

(G) p21 IF staining shows no differences between control KD and Myo6 KD. Procedure was performed as in (E), except for the usage of p21 specific antibodies. Scale bar = 10 μ m

(H) 53BP1 foci are increasing 2 days after Myo6 KD in BJ cells. Procedure was performed as in (F), except for the usage of 53BP1 specific antibodies.

4. Discussion

So far, very little is known about the roles of actin cytoskeletal proteins in the nucleus. It was shown that F-actin is involved in the HDR pathway, yet lacking a mechanism^{20,21}. To better understand the role of cytoskeleton proteins in the nucleus, this work focused on the investigation of myosins, the motors on F-actin. Of particular interest was the role of a unique myosin with its special backward orientation: Myo6.

The aim of this work was to reveal new functions of Myo6 for genome stability and ageing. Based on preliminary data, the focus was laid on Myo6's role in HDR and its likely function in senescence as a result of repair defects. This thesis provides first evidence for a functional contribution of Myo6 in removal of KU70/80 from DSB ends. This modification of the initial phase of HDR may lead to an accumulation of DNA damage in primary cell lines and a phenotype associated with senescence.

4.1 Myo6 depletion results in a survival defect

In this work, a modified colony formation assay that provides more accurate results on DNA repair and subsequent survival was performed. This was achieved by plating cells after treatment instead of before as done during my master's thesis^{84,85}. With this improved assay, the survival defect in Myo6-depleted cells could be confirmed with CPT and NCS representing different DNA damages (Figure 6A & Figure S1). The main limitation of the CFA is that it cannot distinguish between dead or non-proliferating cells. Only visible colonies are counted after two weeks, but whether cells are alive but no longer proliferating is not included in the validation. To avoid this disadvantage, another approach could be a viability option, such as an MTT test or a chemiluminescence test that detects the ATP content in the cells.

The MTT assay for example, is based on the activity of mitochondrial dehydrogenase. The main limitation of this assay is that evaluation is affected when the tested DNA-damaging agent targets mitochondria. For our interest, CFA with plating after treatment was the most appropriate technique. This would ideally be complemented with another viability assay technique to distinguish between dead and non-proliferating cells, such as the flow cytometry experiments in Figure 8E.

Here, S-phase cells were labeled with EdU and tracked into the next cell cycle. By combining the EdU pulse with a subsequent CPT treatment (CPT causes DNA damage only in S-phase), the labeled cells would also be the DNA-damaged cells. With this approach, it would be possible to track the damaged cells and observe how many of them manage to enter the next cell cycle, how many arrest, and what percentage of the population dies. Preliminary

experiments were conducted to test this approach and initial results were very promising that it is possible to track damaged cells into next cell cycle (data not shown). CPT-treated WT cells showed a (very slow) cell cycle progression to the next cell cycle phase, indicating the cell cycle slow down upon DNA damage (data not shown). Since during the optimization phase a different focus was set in my work, I could not finalize these experiments, but specialized flow cytometry is a promising approach to follow the progress of damaged cells through the cell cycle.

4.2 Myo6-depleted cells show less cell cycle slow down upon DNA damage

In general, cells reduce cell cycle speed upon DNA damage⁹³. During DDR, checkpoints are activated that slow down cell cycle progression to repair the DNA damage⁹³. The behaviour of Myo6 KO cells, however, is different. They progress quicker through in S-phase upon CPT damage and continue cell cycle progression to late S-phase faster than WT cells (Figure 8A-D). This phenotype was also observed in DNA fibre assays upon DNA damage (pers. commun. Jie Shi) and may be explained by reduced recruitment of HDR markers to the damaged DNA, which also act as checkpoints for cell cycle progression. One of this markers is phosphorylated RPA^{93,94}. Hyperphosphorylation of RPA by ATR leads to Chk1 activation and thus to DNA replication arrest⁹⁴. Analysis of RPA foci per nucleus and pRPA intensity per nucleus showed that both markers were less present at the DSB sites in Myo6 KO cells than in WT cells (Figure 6C, D, H). This may serve as an explanation since when cell cycle slowing checkpoints are less activated, cell cycle slowing is performed to a lesser extent.

4.3 Myo6 characterisation in HDR

Several HDR markers, such as Rad51, pRPA, and RPA were tested in this thesis and showed a reduction in intensity or in foci formation at DNA damage sites upon Myo6 depletion (Figure 6B-D). The general damage response in the form of H2AX phosphorylation was not affected upon depletion of Myo6 (Figure 6F). A specialized assay to directly test for resection revealed that long-range resection was impaired by Myo6 depletion (Figure 6E). It was also shown that there was no delay in γ H2AX resolution in Myo6-KO cells after DNA damage even when the intensity of pRPA as HDR marker was reduced (Figure 6G-H).

The observed RPA phenotype was confirmed using different cell lines and approaches to deplete the Myo6 pool (Figure 7 and Figure 11A), which together indicate that the phenotype of HDR impairment is caused by the depletion of the nuclear pool of Myo6 (Figure 11B-D). This finding was further supported by localizing Myo6 at DSB sites using live cell imaging

Discussion

(pers. Commun. Hans-Peter Wollscheid). Here, Myo6 fused to a GFP tag was transiently overexpressed in cells and DNA damage was induced using laser tracks. Upon Myo6-GFP overexpression, Myo6 was recruited into the nucleus after DNA damage, but not enriched at the DNA damage site. The localization of Myo6 to the nucleus upon IR was published before by Bennetzen *et al.*⁸⁸. Using SILAC-based proteomics, they observed that several DNA damage related proteins, translation related proteins, energy metabolism related proteins and more translocate into the nucleus upon IR⁸⁸. Next, overexpression of a Myo6-GFP motor domain-deficient mutant and its response to DNA damage was tested in an analogous experiment. This motor-deficient mutant was accumulating at the laser track site (pers. commun. Hans-Peter Wollscheid). This observation led to the hypothesis that Myo6 passively localizes to sites of damage but actively re-localizes using its motor domain. In a last experiment, a Myo6-GFP Δ motor mutant with additional mutations in the ubiquitin binding sites was tested. This mutant accumulated significantly less at the DSB sites compared to the exclusive motor deficient mutant (pers. commun. Hans-Peter Wollscheid). Taken together, these experiments suggest that Myo6 is recruited to the DSB site through its ubiquitin-binding domains and actively transports itself away from it (using its motor domain). Recruitment through the ubiquitin-binding domain to the DSB would be likely as many proteins are known to be recruited to DNA lesions via the complex ubiquitin code⁹⁵. Taken together, the live cell imaging data as well as the SPOP system data are powerful evidence that the role of Myo6 in HDR is indeed carried out by nuclear Myo6.

In this thesis, an attempt was made to generate an inducible Myo6-DARPin NLS cell line that (upon induction) should localize cytoplasmic Myo6 to the nucleus. This technique was also used by Shi *et al.*, but in U2OS cells³¹. In A549 cells, the Myo6 antibody showed non-specific binding in the nucleus. Microscopy images showed re-localization of cytoplasmic Myo6 to the nucleus, but the cytoplasmic pool was not completely re-localized as it was the case for U2OS cells (Figure 11E). The Myo6-DARPin NLS cell line would need to be further tested, for example in comparison to KD / KO cell lines to draw meaningful conclusions. Nevertheless, several clones showed that the cytoplasmic Myo6 pool was strongly reduced after expression of the construct yet no changes in the RPA phenotype could be observed. Taken together with the previously discussed data, this is another indication that the nuclear Myo6 pool is solely responsible for the observed DNA damage response phenotype.

Up to this point, it has been shown in this thesis that nuclear Myo6 depletion leads to impaired resection during HDR. This was also one of the suggested involvement points for F-actin^{20,21}. Schrank and colleagues demonstrated that resection at DSB sites is reduced upon actin filament

Discussion

polymerization inhibition²⁰. Indeed, it was possible to reproduce the results in terms of the reduced number of RPA foci per cell and the same phenotype appeared when Myo6 was depleted (Figure 7G-H). Moreover, an epistatic effect was demonstrated when F-actin formation is inhibited and Myo6 is depleted. This suggests that these two factors are jointly involved in the same process. This assumption is not unlikely, since Myo6 requires F-actin for many of its functions in order to move along it.

Interestingly, Schrank and colleagues did not further investigate how F-actin influences HDR-dependent resection. Thus, it is still possible that F-actin is involved upstream of long-range resection, as suspected for Myo6 involvement.

4.4 Myo6's role in HDR

A previously performed mass spectrometry experiment revealed KU70/80 and VCP as interaction partners for Myo6³¹. Other identified proteins involved in early HDR were chromatin remodelers, such as NAP1L1, RUVBL1/2, etc.. Based on the interaction partners of Myo6 from this mass spectrometry, Myo6 could be associated with chromatin remodelers or with VCP KU70/80 during HDR. To investigate this in more detail, initial experiments were conducted in both possible directions in which Myo6 could be involved (Figure 12). First, co-depletion of ARID-1A with Myo6 showed an epistatic effect on chromatin-bound RPA upon DNA damage. This could indicate an involvement of these proteins in the same pathway. Secondly, chromatin-bound KU70 enriched drastically after IR damage upon Myo6 depletion. Due to this dramatic effect, a focus was laid on Myo6 in KU70/80 removal.

For more detailed characterisation, western blot analysis was exchanged to IF staining in order to have a more quantitative approach. Indeed, not only western blot but also IF staining showed an impairment of resolution of KU80 foci after depletion of Myo6. This implies that the mechanism of how Myo6 affects HDR is at a very early step in the pathway. After short-range resection and before long-range resection, Myo6 is involved in the removal of KU70/80 from DSB ends.

Taken together with the DNA damage accumulation in primary cell lines upon Myo6 depletion (Figure 15F, H), this could indicate that impaired KU70/80 removal results in blocked DSB ends. Once the HDR repair pathway is chosen, the cell cannot switch back to the NHEJ pathway to repair the DSB. After short-term resection, KU70/80 needs to be removed. If removal of KU70/80 is impaired, as after depletion of Myo6, this will result in no further resection at DSB sites. Since no further processing is possible in the HDR pathway because KU70/80 is bound

Discussion

to the DSB ends, the DSB may not be repaired at all⁹⁶, DSB repair is blocked, and unrepaired DSBs might accumulate in the cell.

Interestingly, Andrin and colleagues suggested a role of F-actin in relation with KU70/80 already in 2012⁶⁹. Based on their results, they suggested F-actin to be a stabilizer for KU70/80 at the DNA damage site. In contrast to this thesis, Andrin and colleagues focused on the very rapid response up to 40 seconds after DNA damage, where they observed an altered retention of KU70/80 from DSB sites upon F-actin polymerization inhibition⁶⁹. In contrast to this thesis, the medium-term effects, after one hour and longer, were neglected in the aforementioned study. Based on what was found in this work, it would be very exciting to see how KU70/80 behaves at the DSB when F-actin formation is inhibited.

As described before, Schrank *et al.* and Caridi *et al.* stated an involvement of actin in resection during HDR^{20,21}. Given that only resection impairment has been shown, but no mechanism, it is possible that Myo6 and F-actin are involved together in the process of KU70/80 removal. This hypothesis is also supported by the finding that Myo6 requires its motor domain to actively move away from the DSB site (pers. commun. Hans-Peter Wollscheid). F-actin would be required for this active transport.

Another interesting finding was made by Wang and colleagues, who showed that WASH (an actin nucleation-promoting factor) is also interacting with KU70/80 upon DSB induction⁹⁷. They demonstrate that KU70/80 is involved in recruitment of WASH to the DNA damage site, where it interacts with KU70/80 and DNA-PKcs. WASH activates the Arp2/3 complex through its VCA domain, thereby stimulating actin polymerization^{98,99}. This VCA domain is also important for DNA relaxation after DNA damage to make potential lesion accessible for repair proteins⁹⁷.

Palumbieri and colleagues hypothesized something similar for F-actin. They state that F-actin might be supportive for chromatin remodeling upon replication stress to make DNA lesion accessible for other factors¹⁰⁰. The functions of F-actin in chromatin remodeling have also been described by Baarlink and colleagues. They state the importance of F-actin in the reorganization of the mammalian nucleus after mitosis by de-condensation of chromatin¹⁰¹. Already in 2014 Plessner and colleagues hypothesizes about a role of F-actin in chromatin organization¹⁵. Some classes of myosins have also been shown to cooperate with chromatin remodeling complexes to facilitate transcription through chromatin¹⁰². A mass spectrometry experiment performed by my colleagues found that chromatin remodeling factors interact with Myo6, which also supports this theory³¹.

Discussion

Based on all these findings, it is possible that WASH recruits Arp2/3 to the DSB site, which then triggers the formation of F-actin. Myo6 is recruited to the DSB via its ubiquitin-binding domain. Upon interaction, F-actin and Myo6 then remodel chromatin to be better accessible for VCP to extract KU70/80 from DSB ends.

Another hypothesis could be that Myo6 acts as an anchor for VCP during extraction of KU70/80 from DNA. Since Myo6 can not only serve as a motor protein, but also as an anchor to DNA or F-actin¹⁰³, this would also be a possibility. KU70/80 has a high affinity for dsDNA and is one of the most tightly-bound proteins to DNA. Its removal from DNA, needs to be actively carried out by VCP (p97), a hexameric AAA+-type ATPase. It has been described as an unfoldase that drags substrates through its central pore. Unfolding of the substrate occurs through the composite binding surface, which locally denatures the substrate and is supported by the pulling force exerted by the D2-ATPase¹⁰⁴. This unfolded polypeptide loop is inserted into the D1 pore, threaded through the central pore, and then ejected from the D2 pore^{105–107}. To exert the pulling force to drag the protein through the central pore, VCP might be fixed or anchored at some point. This opposing pole of strength has not yet been studied, but the data presented here support a role of Myo6 in this process. Myo6 could anchor VCP at DNA or F-actin to ensure removal of KU70/80 from DNA. This would be an interesting topic for future investigations.

A third hypothesis could be that Myo6 actively transports KU70/80 away from the DSB site after removal of KU70/80 by VCP. With the help of its motor domain, it could also be involved in the removal of VCP from the DSB side. For this function, its motor domain and also F-actin would be needed as a track.

There are many hypotheses about the mechanistic effect of Myo6 in DSB repair. This work represents the first step to characterize and narrow down the function of the cytoskeletal protein Myo6 in HDR.

4.5 Myo6's role in replication stress

In Shi *et al.*, it was hypothesized that Myo6 positively regulates the association of WRNIP1 with reversed replication forks³¹. This theory is based on an assay in which depletion of Myo6 led to reduced accumulation of WRNIP1 at the replication stress site. The new findings from this thesis also allow other assumptions to be made about Myo6's involvement during replication stress.

During replication stress, the replication fork can stall and form a reversed fork structure. This structure serves to stabilize the replication fork and can be resolved when the reversed fork is

Discussion

restarted^{108,109}. These dysfunctional forks provide a single dsDNA end for KU70/80 binding, which is very similar to a seDSB end. KU70/80 is recruited to seDSBs and also to terminally arrested reversed forks^{56,110,111}. Teixeira-Silva and colleagues showed that KU70/80 ensures the two-step mechanism of fork resection¹¹⁰ avoiding unnecessary extensive resection by restricting the initial resection and thereby fine-tuning HR-mediated fork restart. They state that KU70/80 removal is an essential step in this process and important for replication restart and cell viability¹¹⁰. This two-step resection is also known from the HDR DSB repair pathway. MRE11 and CtIP perform the first-step and after which KU70/80 needs to be removed. The mechanism seems to be a little different for reversed forks, because if KU70/80 is not removed from the fork, there is a defect in the RPA displacement by Rad51⁵⁶. Both cases have in common that KU70/80 must be removed from the DNA to ensure complete repair.

Thus, if Myo6 is involved in KU70/80 removal at the beginning of the HDR pathway, this could also be its role during replication stress. As discussed before, another option for Myo6's involvement could be in chromatin remodelling during fork reversal / fork restart to ensure accessibility for repair-related proteins.

4.6 Myo6's role in senescence

One hallmark of senescence is a stable and in general reversible cell cycle arrest in G1 and S phase. Cells use this state as one of the most important tumor suppressor mechanisms. If a cell has accumulated too much damage, and proper cell division is endangered, senescence can be induced to prevent passing on damaged genetic information to daughter cells. When the damage is repaired and all checkpoints are deactivated, the cell can restart the cell cycle and start dividing again⁷⁴. In case the damage in the cell is beyond repair, apoptosis, a programmed cell death, can be initiated.

In previous experiments by colleagues, senescence-associated phenotypes were observed in primary cells after Myo6 depletion. RPE-hTERT and MCF10A cells displayed a cell cycle arrest in G1 and developed a dramatic increase in cell size upon Myo6 depletion. This phenotype is a typical sign of senescence. Furthermore, Myo6 interacts with a key factor in senescence induction, p53. Genetic and physical interaction of p53 with Myo6 and the ability of Myo6 to positively regulate RNA polymerase II transcription may hint at Myo6 involvement in senescence²⁸. Moreover, Myo6 is not only involved in transcription, but also plays an important role in secretion¹¹², a crucial process for the formation and maintenance of SASP.

In the present study, the role of Myo6 in senescence was further explored. It was demonstrated that WI-38 cells immediately induce p53 dependent cell death upon Myo6 depletion,

Discussion

presumably through apoptosis (Figure 15A). Different approaches were used to show an increase in β -galactosidase activity in Myo6-depleted BJ cells (Figure 15B-D). It was also very exciting to observe that BJ cells accumulate endogenous DNA damage after Myo6 depletion. This was demonstrated by the observation of γ H2AX foci and 53BP1 foci after Myo6 depletion (Figure 15F, H).

These observations in context with the results obtained from Myo6 in the DNA repair pathway allow interesting speculations to be drawn. Thus, one could speculate that senescence is initiated as a biological consequence through impairment of HDR upon Myo6 depletion.

In general, senescence is initiated by chronic DDR. If Myo6 is involved in the removal of KU70/80, and in the absence of Myo6 KU70/80 blocks DSB ends for further processing, endogenous damage cannot be repaired. Therefore, once endogenous DNA damage accumulates, chronic DDR will occur and senescence can be induced.

It was already described in the literature that senescence has effects on the cytoskeleton. The morphological changes of senescent cells, such as flattening and enlargement, are associated with actin stress fibers¹¹³. It was also reported that senescence is linked to reorganization of microtubules and deficiencies in microtubule and actin cytoskeleton¹¹⁴. But only a few scientists have so far turned the connection around and looked at whether the cytoskeleton can also influence senescence. Xiaodong and colleagues showed that cytoskeletal stiffness in combination with RhoA/Sun2 signaling represents a mechanism for promoting ageing and cellular senescence¹¹⁵. Interestingly, Magistrati and colleagues recently published the same phenotype we observed in Myo6 depleted primary cell lines⁸³. They observed a cell cycle arrest in hTERT-RPE1 and BJ-hTERT cells upon Myo6 knockdown, which was rescued by co-depletion of p53. Additionally, they observed a β -Galactosidase activity increase in Myo6-depleted cells and an increase of p53 and p21 upon Myo6 KD⁸³. These phenotypes were not observed upon Myo6 depletion in p53-null cancer cell lines. Therefore, the hypothesis is that Myo6 is involved in a cell cycle maintenance pathway that is deregulated upon carcinogenesis⁸³. Interestingly, this is consistent with our observations of the phenotype changes upon Myo6 depletion in primary cell lines (WI-38 and BJ). Cancer-derived cell lines, such as A549 and HeLa, showed no phenotype changes upon Myo6 depletion, although A549 KO cells showed severe survival defects after DNA damage induction by CPT and NCS. These observations would fit the hypothesis of Magistrati and colleagues that the pathway involving Myo6 is deregulated upon carcinogenesis.

Research in the area of the cytoskeleton and senescence is still quite new, but based on knowledge from the literature, initial experiments from this thesis, and the study by Magistrati

Discussion

and colleagues, there is strong evidence that Myo6 influences the induction of senescence. One hypothesis could be that after deletion of Myo6, unrepaired, endogenous DNA damage accumulates due to DNA blockade of KU70/80, thereby triggering chronic DDR and consequently leading cells into senescence.

4.7 Summary and Outlook

The aim of this thesis was to study the molecular motor Myo6 in genome stability and ageing. Here, I could show for the first time that Myo6 is involved in the removal of KU70/80, an early step of DNA DSB repair in the HDR pathway. Through the experiments of Hans-Peter Wollscheid, it is also known that Myo6 requires its motor domain to actively move away from the DSB site. This suggests that F-actin is also involved in this process. Preliminary experiments also suggest an accumulation of unrepaired DNA damage in primary cell lines, resulting in induction of senescence.

In more detail, Myo6-depleted cells show a significant survival defect upon CPT and NCS treatment in colony formation assays. IF staining showed that the general damage response to CPT and NCS in form of H2AX phosphorylation is not changed in Myo6 KO cells. In contrast, HDR marker such as Rad51, pRPA, and RPA were reduced in intensity or foci buildup upon Myo6 depletion. In addition, a special resection assay, which exclusively detects ssDNA in cells, showed a reduction of resection after CPT and NCS treatment in Myo6 KO cells. The general repair kinetics are not different in Myo6-depleted cells. To exclude any possibility that the phenotype is an artifact of the cell line or the depletion method, the RPA phenotype was verified in A549 and HeLa cells after KD and KO upon CPT and NCS. An epistatic effect in terms of the number of RPA foci after damage between Myo6 and CK666 (Arp2/3 inhibitor) was also observed. Using flow cytometry, the cell cycle profiles of Myo6-depleted cells were examined in comparison to WT cells. This showed that Myo6 KO cells do slow down the cell cycle to a lower extent after damage and continue to rush into late S phase, whereas WT cells decrease the speed to repair the DNA damage first. To answer the complex question of whether only the nuclear pool of Myo6 is responsible for the effects observed, I generated stable cell lines. These contained the 2-RING construct coupled to a non-binding DARPIn and to a Myo6-binding DARPIn that can inducibly proteasomally degrade the entire cellular pool of Myo6. Another construct was the SPOP system coupled to a non-binding DARPIn and to a Myo6-binding DARPIn. This system was tagged to an NLS to only degrade the nuclear pool of Myo6 in an inducible manner. The third construct was a non-binding DARPIn or Myo6-binding DARPIn coupled with an NLS tag to bring the cytoplasmic pool of Myo6 into the nucleus. The

Discussion

2-RING system demonstrated what had been observed previously, that the number of RPA foci is reduced after induction of DNA damage when Myo6 is depleted. The SPOP construct showed that upon depletion of the nuclear pool of Myo6, RPA foci number is also reduced after DNA damage. After re-localizing the cytoplasmic Myo6 pool into the nucleus the cells showed no changes in RPA foci number per cell after damage induction. These experiments indicate that the nuclear pool of Myo6 is responsible for the observed HDR defect. The following experiments focused on the mechanism involving Myo6 during HDR. Based on some initial experiments, I investigated the role of Myo6 in the removal of KU70/80. After optimization of KU80 IF staining, it was observed that KU80 foci were formed after IR treatment, but they had not resolved in Myo6 KO cells after 4 hours, in contrast to WT cells. The same phenotype was observed for VCP inhibitor treated cells. Since VCP is involved in the removal of KU70/80 from DNA during HDR and the same phenotype was observed as in Myo6-depleted cells, their involvement in the same mechanism is likely. In combination with a previously performed mass spectrometry experiment in which Myo6 interacted with KU70/80 and VCP, the hypothesis was supported³¹. This part of the project demonstrated the involvement of Myo6 in one of the most important DNA repair pathways in cells, the HDR pathway. All results taken together, the role of Myo6 seems to be in the removal of KU70/80 during resection.

In the second part of this thesis, I investigated the role of Myo6 in the induction of senescence. My colleagues and I were able to detect a phenotype associated with senescence in primary cell lines after KD of Myo6. The β -galactosidase activity was increased in these cells and the morphology changed to enlarged cells, typical signs of senescence. In addition, I demonstrated that Myo6-depleted primary cell lines accumulate endogenous DNA damage.

Combining these two parts of my thesis, the results suggest that upon Myo6 depletion, KU70/80 removal is impaired, DSBs are blocked, and DNA damage is accumulated, leading to senescence in primary cells as a biological consequence. When the choice of repair pathway is based on the resection-friendly environment, the homologous repair pathway is chosen. This decision means that a short-range resection will take place. The next step would be to remove KU70/80 from the DSB ends to make room for long-range resection. However, if this step is impaired after depletion of Myo6, the DSB ends are blocked for further processing and DNA damage accumulates. Upon this chronic DDR, primary cell lines might induce senescence.

The results of this thesis demonstrate a new role of Myo6 in DNA repair. Its involvement in KU70/80 removal has been shown, but a precise mechanism remains unknown. It would be very interesting to further investigate its mechanism, particularly in KU70/80 removal. The

Discussion

cooperation with F-actin should also be investigated in more detail. How KU80 foci behave when F-actin formation is inhibited would be an exciting question. Another approach would be to address how exactly Myo6 is recruited to the DSB site. Are ubiquitin chains at KU70/80 recruiting Myo6 or others at surrounding proteins or DNA? What type of ubiquitin chains are recruiting Myo6? These questions could be addressed *in vitro* with purified proteins and different E3 ubiquitin ligases. Alternatively, cell lysates could be treated with different deubiquitinases after DNA damage and investigated whether there is an interaction between KU70/80 and Myo6.

Applying the optimized flow cytometry approach to follow labeled/damaged cells to the next cell cycle would also be an interesting experiment. To test whether Myo6-depleted cells can go to the next cell cycle after DNA damage or go into senescence or apoptosis. This could be additionally answered with an apoptosis staining in flow cytometry. Complementary viability assays for Myo6-depleted cells after DNA damage would be interesting as well.

A basis has been laid for Myo6 role in senescence, but many questions are still open. First, it would be of great interest to see whether it is DDR induced senescence and via which exact pathway it is activated. For this purpose, different markers for senescence induction could be tested to see whether they change after Myo6 depletion. Further the interaction between Myo6 and p53 should be investigated in more detail. The role of F-actin in this context would be as well very interesting.

Research could also be conducted to determine whether only Myo6 plays a role in these pathways or whether other myosins are also involved or more generally speaking, whether or which other cytoskeletal proteins might be involved.

Recently, many exciting discoveries about the cytoskeleton have been made. Santos and colleagues could show F-actin in the microtubule lumen using cryogenic electron tomography in *Drosophila* S2 cell protrusions¹¹⁶. They demonstrated that cofilin activation is stimulating F-actin accumulation inside the microtubules. It is assumed that the connection between F-actin and the microtubule wall stabilizes the microtubules. In 2020, microtubule luminal filaments were also found in human cells¹¹⁷. All these findings improve our understanding of the cytoskeleton and all the complex interactions in which it is involved.

Defects in Myo6 have already been associated with various diseases, such as deafness, hypertrophic cardiomyopathy and neurodegeneration. But this year Panier and colleagues could show that RhoJ, which controls the dynamic reorganization of F-actin, promotes cancer therapy resistance^{118,119}. Through the ability of RhoJ to induce the formation of F-actin, it positively

Discussion

regulates DNA repair and replication stress tolerance of cancer cells. This means that F-actin is involved in resistance to cancer therapies and that RhoJ is a promising target to overcome the therapy resistance of cancer cells. Myo6 is consistently overexpressed in prostate cancer and high-grade ovarian cancer, and the degree of overexpression is associated with the aggressiveness of ovarian cancer^{22,23}. Taken together, if F-actin regulates DNA repair and replication stress tolerance of cancer cells, it might be that Myo6 is also involved. The results of this study show that Myo6 is important for DSB repair, and on this basis, Myo6 might also be involved in therapy resistance of certain cancers.

For new approaches in the treatment of various diseases where F-actin is involved, F-actin cannot be inhibited directly, because other important functions of cells would be affected as well. Therefore, it is important to identify interactors of F-actin to create targeted therapies for special cell types. This is why research on myosins, as motors on F-actin, is so crucial to gain new insights into the diverse roles of the cytoskeleton and into possible new therapeutic approaches.

5. List of Tables

Table 1: Lab devices and equipment.....	19
Table 2: Software	19
Table 3: Chemicals.....	19
Table 4: Antibodies	21
Table 5: siRNAs	22
Table 6: Plasmids	22
Table 7: Media and buffer solutions	23
Table 8: Mammalian cell lines	23

6. List of Figures

Figure 1: Processive stepping of myosin V along actin filament.....	2
Figure 2: Schematic of Full-Length Myosin VI.....	4
Figure 3: A decision tree of DNA double strand break repair	8
Figure 4: NHEJ and HDR - the two main DSB repair mechanisms	11
Figure 5: Senescence drivers and phenotypes.....	16
Figure 6: Knockout of Myo6 results in impaired survival and decreased HDR marker levels upon DNA damage.....	34
Figure 7: RPA phenotype is conserved in A549 / HeLa cells after KO or KD upon CPT and NCS.....	37
Figure 8: Myo6 depletion leads to different behaviour in cell cycle progression in A549 cells upon CPT treatment	40
Figure 9: DARPIn 2-RING-mediated destruction system testing for Myo6 depletion.....	43
Figure 10: SPOP system for nuclear degradation of Myo6	45
Figure 11: Different Myo6 degradation systems or re-localisation of Myo6	48
Figure 12: Myo6 in chromatin remodelling vs Myo6 in KU70/80 removal.....	50
Figure 13: KU foci Optimization	53
Figure 14: Myo6 in KU70/80 removal.....	55
Figure 15: Myo6 role in senescence.....	59
Figure S1: Knockout of Myo6 results in impaired survival and decreased HDR marker levels upon CPT.....	87

Abbreviations

Figure S2: Replicates of figure 6: Knockout of Myo6 results in impaired survival and decreased HDR marker levels upon NCS 89

Figure S3: Replicates of figure 7: RPA phenotype is conserved in A549 / HeLa cells after KO or KD upon CPT and NCS 90

Figure S 4: representative Western blots for KD efficiency in A549 and HeLa cells 91

Figure S5: Replicates of figure 7: Epistasis upon actin polymerisation inhibition and Myo6 *knockout* 92

Figure S 6: Replicates of figure 8: Myo6 depletion leads to different behaviour in cell cycle progression in A549 cells upon CPT treatment 93

Figure S7: Replicates of figure 11: 2-RING and SPOP system for degradation of Myo6 94

Figure S8: Replicates of figure 14: Myo6 in KU70/80 removal..... 95

7. Abbreviations

2-RING	Antibody RING-mediated destruction system
aEJ	alternative End Joining
ATM	Ataxia telangiectasia mutata
ATP	Adenosine Tri Phosphate
ATR	Ataxia telangiectasia and Rad3 related
BIR	Break induced replication
ARMeD / 2-RING	Antibody RING-mediated destruction
BLM	Bloom syndrome protein
BSA	Bovine serum albumin
CAM	Calmodulin
CBD	cargo binding domain
CFA	Colony formation assay
cNHEJ	Classical Non-Homologous End Joining
CPT	Camptothecin
Dab-2	endocytic adaptor protein
DARPin	Designed Ankyrin Repeat Proteins
DDR	DNA damage response
DMEM	Dulbecco's Modified Eagle Medium
DNA	Deoxyribonucleic acid
DNA-PKcs	DNA-dependent protein kinase catalytic subunit
DOX	doxycycline

Abbreviations

DSB	Double strand break
F-actin	filamentous actin
FBS	Fetal bovine serum
FIJI	Fiji Is Just ImageJ
GFP	Green fluorescent protein
HDR	Homology Directed Repair
IF	Immunofluorescence
IR	ionizing radiation
KO	MyosinVI knockout
KU	Ku70-Ku80 heterodimer
LIG4	Ligase IV
MCP1	monocyte chemoattractant protein 1
MG132	Proteasomal inhibitor
MIU	Motif interacting with ubiquitin
MMEJ	microhomology-mediated end joining
MMP	matrix metalloproteinases
mRNA	Messenger RNA
Myo6	Myosin VI
MyUb	myosin VI ubiquitin-binding domain
NCS	Neocarzinostatin
NLS	Nuclear localisation signal
NEB	New England Biolabs
PBS(-T)	Phosphate buffered saline (-Tween)
pRPA	phosphorylated Replication protein A
RNAPII	RNA polymerase II
ROS	reactive oxygen species
RPA	Replication protein A
RT	Room temperature
SAH	single alpha helix
SPOP	adaptor protein of the Cullin-RING E3 ubiquitin ligase complex
SASP	senescence associated secretory phenotype
SA-β-gal	senescence-associated- β -galactosidase
SDSA	Synthesis-dependent strand annealing
seDSB	Single ended DSB
SERPINS	serine/cysteine proteinase inhibitors
SPOP	Speckle-type POZ Protein

Abbreviations

SSA	Single strand annealing
TIMPs	tissue inhibitors of metalloproteinases
UV	Ultraviolet radiation
VCP	Valosin-containing protein (or p97)
WT	Wildtype
XLF	XRCC4-like factor

8. Eigenständigkeitserklärung

Ich, Kristine Hauschulte, geboren am 14.08.1997 in Eupen (Belgien), Matrikelnummer 2726179 versichere, dass ich meine Doktor-Thesis selbständig verfasst und keine anderen als die angegebenen schriftlichen und elektronischen Quellen sowie andere Hilfsmittel benutzt habe. Alle Ausführungen, die anderen Schriften wörtlich oder sinngemäß entnommen wurden, habe ich kenntlich gemacht. Zusätzlich bestätige ich, dass diese Arbeit nicht an anderer Stelle als Prüfungsleistung vorgelegt wurde.

Mainz, den 14.07.2023

(Ort, Datum)

(Unterschrift)

Eigenständigkeitserklärung

9. References

- (1) Hohmann, T.; Dehghani, F. The Cytoskeleton—A Complex Interacting Meshwork. *Cells* **2019**, *8* (4), 362. <https://doi.org/10.3390/cells8040362>.
- (2) de Lanerolle, P. Nuclear Actin and Myosins at a Glance. *Journal of Cell Science* **2012**, *125* (21), 4945–4949. <https://doi.org/10.1242/jcs.099754>.
- (3) Foth, B. J.; Goedecke, M. C.; Soldati, D. New Insights into Myosin Evolution and Classification. *Proceedings of the National Academy of Sciences* **2006**, *103* (10), 3681–3686. <https://doi.org/10.1073/pnas.0506307103>.
- (4) Berg, J. S.; Powell, B. C.; Cheney, R. E. A Millennial Myosin Census. *Mol Biol Cell* **2001**, *12* (4), 780–794. <https://doi.org/10.1091/mbc.12.4.780>.
- (5) Fili, N.; Toseland, C. P. Unconventional Myosins: How Regulation Meets Function. *Int J Mol Sci* **2019**, *21* (1), 67. <https://doi.org/10.3390/ijms21010067>.
- (6) Ryan, J. M.; Nebenführ, A. Update on Myosin Motors: Molecular Mechanisms and Physiological Functions1[OPEN]. *Plant Physiol* **2018**, *176* (1), 119–127. <https://doi.org/10.1104/pp.17.01429>.
- (7) Hartman, M. A.; Spudich, J. A. The Myosin Superfamily at a Glance. *J Cell Sci* **2012**, *125* (7), 1627–1632. <https://doi.org/10.1242/jcs.094300>.
- (8) Woolner, S.; Bement, W. M. Unconventional Myosins Acting Unconventionally. *Trends Cell Biol* **2009**, *19* (6), 245–252. <https://doi.org/10.1016/j.tcb.2009.03.003>.
- (9) Fletcher, D. A.; Mullins, R. D. Cell Mechanics and the Cytoskeleton. *Nature* **2010**, *463* (7280), 485–492. <https://doi.org/10.1038/nature08908>.
- (10) Köhler, D.; Ruff, C.; Meyhöfer, E.; Bähler, M. Different Degrees of Lever Arm Rotation Control Myosin Step Size. *J Cell Biol* **2003**, *161* (2), 237–241. <https://doi.org/10.1083/jcb.200212039>.
- (11) Magistrati, E.; Polo, S. Myomics: Myosin VI Structural and Functional Plasticity. *Curr Opin Struct Biol* **2021**, *67*, 33–40. <https://doi.org/10.1016/j.sbi.2020.09.005>.
- (12) Spudich, J. A. The Myosin Swinging Cross-Bridge Model. *Nat Rev Mol Cell Biol* **2001**, *2* (5), 387–392. <https://doi.org/10.1038/35073086>.
- (13) Van Gele, M.; Dynoodt, P.; Lambert, J. Griscelli Syndrome: A Model System to Study Vesicular Trafficking. *Pigment Cell Melanoma Res* **2009**, *22* (3), 268–282. <https://doi.org/10.1111/j.1755-148X.2009.00558.x>.
- (14) Trivedi, D. V.; Nag, S.; Spudich, A.; Ruppel, K. M.; Spudich, J. A. The Myosin Family of Mechanoenzymes: From Mechanisms to Therapeutic Approaches. *Annual Review of Biochemistry* **2020**, *89* (1), 667–693. <https://doi.org/10.1146/annurev-biochem-011520-105234>.
- (15) Plessner, M.; Melak, M.; Chinchilla, P.; Baarlink, C.; Grosse, R. Nuclear F-Actin Formation and Reorganization upon Cell Spreading. *J Biol Chem* **2015**, *290* (18), 11209–11216. <https://doi.org/10.1074/jbc.M114.627166>.
- (16) Wells, A. L.; Lin, A. W.; Chen, L. Q.; Safer, D.; Cain, S. M.; Hasson, T.; Carragher, B. O.; Milligan, R. A.; Sweeney, H. L. Myosin VI Is an Actin-Based Motor That Moves Backwards. *Nature* **1999**, *401* (6752), 505–508. <https://doi.org/10.1038/46835>.
- (17) Buss, F.; Spudich, G.; Kendrick-Jones, J. MYOSIN VI: Cellular Functions and Motor Properties. *Annual Review of Cell and Developmental Biology* **2004**, *20* (1), 649–676. <https://doi.org/10.1146/annurev.cellbio.20.012103.094243>.
- (18) Wollscheid, H.-P.; Biancospino, M.; He, F.; Magistrati, E.; Molteni, E.; Lupia, M.; Soffientini, P.; Rottner, K.; Cavallaro, U.; Pozzoli, U.; Mapelli, M.; Walters, K. J.; Polo, S. Diverse Functions of Myosin VI Elucidated by an Isoform-Specific α -Helix Domain. *Nat Struct Mol Biol* **2016**, *23* (4), 300–308. <https://doi.org/10.1038/nsmb.3187>.
- (19) Mukherjea, M.; Llinas, P.; Kim, H.; Travaglia, M.; Safer, D.; Ménétrey, J.; Franzini-Armstrong, C.; Selvin, P. R.; Houdusse, A.; Sweeney, H. L. Myosin VI Dimerization

References

- Triggers an Unfolding of a 3-Helix Bundle in Order to Extend Its Reach. *Mol Cell* **2009**, 35 (3), 305–315. <https://doi.org/10.1016/j.molcel.2009.07.010>.
- (20) Schrank, B. R.; Aparicio, T.; Li, Y.; Chang, W.; Chait, B. T.; Gundersen, G. G.; Gottesman, M. E.; Gautier, J. Nuclear Arp2/3 Drives DNA Break Clustering for Homology-Directed Repair. *Nature* **2018**, 559 (7712), 61–66. <https://doi.org/10.1038/s41586-018-0237-5>.
- (21) Caridi, C. P.; D’Agostino, C.; Ryu, T.; Zapotoczny, G.; Delabaere, L.; Li, X.; Khodaverdian, V. Y.; Amaral, N.; Lin, E.; Rau, A. R.; Chiolo, I. Nuclear F-Actin and Myosins Drive Relocalization of Heterochromatic Breaks. *Nature* **2018**, 559 (7712), 54–60. <https://doi.org/10.1038/s41586-018-0242-8>.
- (22) Dunn, T. A.; Chen, S.; Faith, D. A.; Hicks, J. L.; Platz, E. A.; Chen, Y.; Ewing, C. M.; Sauvageot, J.; Isaacs, W. B.; De Marzo, A. M.; Luo, J. A Novel Role of Myosin VI in Human Prostate Cancer. *Am J Pathol* **2006**, 169 (5), 1843–1854. <https://doi.org/10.2353/ajpath.2006.060316>.
- (23) Yoshida, H.; Cheng, W.; Hung, J.; Montell, D.; Geisbrecht, E.; Rosen, D.; Liu, J.; Naora, H. Lessons from Border Cell Migration in the Drosophila Ovary: A Role for Myosin VI in Dissemination of Human Ovarian Cancer. *Proc Natl Acad Sci U S A* **2004**, 101 (21), 8144–8149. <https://doi.org/10.1073/pnas.0400400101>.
- (24) Mohiddin, S. A.; Ahmed, Z. M.; Griffith, A. J.; Tripodi, D.; Friedman, T. B.; Fananapazir, L.; Morell, R. J. Novel Association of Hypertrophic Cardiomyopathy, Sensorineural Deafness, and a Mutation in Unconventional Myosin VI (MYO6). *J Med Genet* **2004**, 41 (4), 309–314. <https://doi.org/10.1136/jmg.2003.011973>.
- (25) Fili, N.; Hari-Gupta, Y.; dos Santos, A.; Cook, A.; Poland, S.; Ameer-Beg, S. M.; Parsons, M.; Toseland, C. P. NDP52 Activates Nuclear Myosin VI to Enhance RNA Polymerase II Transcription. *Nat Commun* **2017**, 8 (1), 1871. <https://doi.org/10.1038/s41467-017-02050-w>.
- (26) Alexander W. Cook; Rosemarie E. Gough; Christopher P. Toseland. *Nuclear myosins – roles for molecular transporters and anchors | Journal of Cell Science | The Company of Biologists*. <https://journals.biologists.com/jcs/article/133/11/jcs242420/224751/Nuclear-myosins-roles-for-molecular-transporters> (accessed 2023-04-18).
- (27) Sarshad, A. A.; Percipalle, P. New Insight into Role of Myosin Motors for Activation of RNA Polymerases. *Int Rev Cell Mol Biol* **2014**, 311, 183–230. <https://doi.org/10.1016/B978-0-12-800179-0.00004-0>.
- (28) Vreugde, S.; Ferrai, C.; Miluzio, A.; Hauben, E.; Marchisio, P. C.; Crippa, M. P.; Bussi, M.; Biffo, S. Nuclear Myosin VI Enhances RNA Polymerase II-Dependent Transcription. *Mol Cell* **2006**, 23 (5), 749–755. <https://doi.org/10.1016/j.molcel.2006.07.005>.
- (29) Loikkanen, I.; Toljamo, K.; Hirvikoski, P.; Väisänen, T.; Paavonen, T.; Vaarala, M. Myosin VI Is a Modulator of Androgen-Dependent Gene Expression. *Oncology reports* **2009**, 22, 991–995. https://doi.org/10.3892/or_00000526.
- (30) Jung, E. J.; Liu, G.; Zhou, W.; Chen, X. Myosin VI Is a Mediator of the P53-Dependent Cell Survival Pathway. *Mol Cell Biol* **2006**, 26 (6), 2175–2186. <https://doi.org/10.1128/MCB.26.6.2175-2186.2006>.
- (31) Shi, J.; Hauschulte, K.; Mikicic, I.; Maharjan, S.; Arz, V.; Strauch, T.; Heidelberger, J. B.; Schaefer, J. V.; Dreier, B.; Plückthun, A.; Beli, P.; Ulrich, H. D.; Wollscheid, H.-P. Nuclear Myosin VI Maintains Replication Fork Stability. *Nat Commun* **2023**, 14 (1), 3787. <https://doi.org/10.1038/s41467-023-39517-y>.
- (32) Aparicio, T.; Baer, R.; Gautier, J. DNA Double-Strand Break Repair Pathway Choice and Cancer. *DNA Repair (Amst)* **2014**, 19, 169–175. <https://doi.org/10.1016/j.dnarep.2014.03.014>.

References

- (33) Bakkenist, C. J.; Kastan, M. B. DNA Damage Activates ATM through Intermolecular Autophosphorylation and Dimer Dissociation. *Nature* **2003**, *421* (6922), 499–506. <https://doi.org/10.1038/nature01368>.
- (34) Blackford, A. N.; Jackson, S. P. ATM, ATR, and DNA-PK: The Trinity at the Heart of the DNA Damage Response. *Molecular Cell* **2017**, *66* (6), 801–817. <https://doi.org/10.1016/j.molcel.2017.05.015>.
- (35) Coleman, K. A.; Greenberg, R. A. The BRCA1-RAP80 Complex Regulates DNA Repair Mechanism Utilization by Restricting End Resection. *J Biol Chem* **2011**, *286* (15), 13669–13680. <https://doi.org/10.1074/jbc.M110.213728>.
- (36) Stewart, G. S.; Panier, S.; Townsend, K.; Al-Hakim, A. K.; Kolas, N. K.; Miller, E. S.; Nakada, S.; Ylanko, J.; Olivarius, S.; Mendez, M.; Oldreive, C.; Wildenhain, J.; Tagliaferro, A.; Pelletier, L.; Taubenheim, N.; Durandy, A.; Byrd, P. J.; Stankovic, T.; Taylor, A. M. R.; Durocher, D. The RIDDLE Syndrome Protein Mediates a Ubiquitin-Dependent Signaling Cascade at Sites of DNA Damage. *Cell* **2009**, *136* (3), 420–434. <https://doi.org/10.1016/j.cell.2008.12.042>.
- (37) Doil, C.; Mailand, N.; Bekker-Jensen, S.; Menard, P.; Larsen, D. H.; Pepperkok, R.; Ellenberg, J.; Panier, S.; Durocher, D.; Bartek, J.; Lukas, J.; Lukas, C. RNF168 Binds and Amplifies Ubiquitin Conjugates on Damaged Chromosomes to Allow Accumulation of Repair Proteins. *Cell* **2009**, *136* (3), 435–446. <https://doi.org/10.1016/j.cell.2008.12.041>.
- (38) Daley, J. M.; Sung, P. 53BP1, BRCA1, and the Choice between Recombination and End Joining at DNA Double-Strand Breaks. *Mol Cell Biol* **2014**, *34* (8), 1380–1388. <https://doi.org/10.1128/MCB.01639-13>.
- (39) Katsuki, Y.; Jeggo, P. A.; Uchihara, Y.; Takata, M.; Shibata, A. DNA Double-Strand Break End Resection: A Critical Relay Point for Determining the Pathway of Repair and Signaling. *GENOME INSTAB. DIS.* **2020**, *1* (4), 155–171. <https://doi.org/10.1007/s42764-020-00017-8>.
- (40) Grundy, G. J.; Rulten, S. L.; Arribas-Bosacoma, R.; Davidson, K.; Kozik, Z.; Oliver, A. W.; Pearl, L. H.; Caldecott, K. W. The Ku-Binding Motif Is a Conserved Module for Recruitment and Stimulation of Non-Homologous End-Joining Proteins. *Nat Commun* **2016**, *7*, 11242. <https://doi.org/10.1038/ncomms11242>.
- (41) Takata, M.; Sasaki, M. S.; Sonoda, E.; Morrison, C.; Hashimoto, M.; Utsumi, H.; Yamaguchi-Iwai, Y.; Shinohara, A.; Takeda, S. Homologous Recombination and Non-Homologous End-Joining Pathways of DNA Double-Strand Break Repair Have Overlapping Roles in the Maintenance of Chromosomal Integrity in Vertebrate Cells. *EMBO J* **1998**, *17* (18), 5497–5508. <https://doi.org/10.1093/emboj/17.18.5497>.
- (42) Scully, R.; Panday, A.; Elango, R.; Willis, N. A. DNA Double-Strand Break Repair-Pathway Choice in Somatic Mammalian Cells. *Nat Rev Mol Cell Biol* **2019**, *20* (11), 698–714. <https://doi.org/10.1038/s41580-019-0152-0>.
- (43) Beucher, A.; Birraux, J.; Tchouandong, L.; Barton, O.; Shibata, A.; Conrad, S.; Goodarzi, A. A.; Krempler, A.; Jeggo, P. A.; Löbrich, M. ATM and Artemis Promote Homologous Recombination of Radiation-Induced DNA Double-Strand Breaks in G2. *EMBO J* **2009**, *28* (21), 3413–3427. <https://doi.org/10.1038/emboj.2009.276>.
- (44) Chang, H. H. Y.; Pannunzio, N. R.; Adachi, N.; Lieber, M. R. Non-Homologous DNA End Joining and Alternative Pathways to Double-Strand Break Repair. *Nat Rev Mol Cell Biol* **2017**, *18* (8), 495–506. <https://doi.org/10.1038/nrm.2017.48>.
- (45) Britton, S.; Coates, J.; Jackson, S. P. A New Method for High-Resolution Imaging of Ku Foci to Decipher Mechanisms of DNA Double-Strand Break Repair. *J Cell Biol* **2013**, *202* (3), 579–595. <https://doi.org/10.1083/jcb.201303073>.
- (46) Graham, T. G. W.; Walter, J. C.; Loparo, J. J. Two-Stage Synapsis of DNA Ends during Non-Homologous End Joining. *Mol Cell* **2016**, *61* (6), 850–858. <https://doi.org/10.1016/j.molcel.2016.02.010>.

References

- (47) Gottlieb, T. M.; Jackson, S. P. The DNA-Dependent Protein Kinase: Requirement for DNA Ends and Association with Ku Antigen. *Cell* **1993**, *72* (1), 131–142. [https://doi.org/10.1016/0092-8674\(93\)90057-w](https://doi.org/10.1016/0092-8674(93)90057-w).
- (48) Ochi, T.; Blackford, A. N.; Coates, J.; Jhujh, S.; Mehmood, S.; Tamura, N.; Travers, J.; Wu, Q.; Draviam, V. M.; Robinson, C. V.; Blundell, T. L.; Jackson, S. P. PAXX, a Paralog of XRCC4 and XLF, Interacts with Ku to Promote DNA Double-Strand Break Repair. *Science* **2015**, *347* (6218), 185–188. <https://doi.org/10.1126/science.1261971>.
- (49) Sfeir, A.; Symington, L. S. Microhomology-Mediated End Joining: A Back-up Survival Mechanism or Dedicated Pathway? *Trends Biochem Sci* **2015**, *40* (11), 701–714. <https://doi.org/10.1016/j.tibs.2015.08.006>.
- (50) Ochi, T.; Wu, Q.; Blundell, T. L. The Spatial Organization of Non-Homologous End Joining: From Bridging to End Joining. *DNA Repair (Amst)* **2014**, *17* (100), 98–109. <https://doi.org/10.1016/j.dnarep.2014.02.010>.
- (51) *DNA End Resection: Facts and Mechanisms | Elsevier Enhanced Reader*. <https://doi.org/10.1016/j.gpb.2016.05.002>.
- (52) Postow, L.; Funabiki, H. An SCF Complex Containing Fbx12 Mediates DNA Damage-Induced Ku80 Ubiquitylation. *Cell Cycle* **2013**, *12* (4), 587–595. <https://doi.org/10.4161/cc.23408>.
- (53) Feng, L.; Chen, J. The E3 Ligase RNF8 Regulates KU80 Removal and NHEJ Repair. *Nat Struct Mol Biol* **2012**, *19* (2), 201–206. <https://doi.org/10.1038/nsmb.2211>.
- (54) Schmidt, C. K.; Galanty, Y.; Sczaniecka-Clift, M.; Coates, J.; Jhujh, S.; Demir, M.; Cornwell, M.; Beli, P.; Jackson, S. P. Systematic E2 Screening Reveals a UBE2D-RNF138-CtIP Axis Promoting DNA Repair. *Nat Cell Biol* **2015**, *17* (11), 1458–1470. <https://doi.org/10.1038/ncb3260>.
- (55) van den Boom, J.; Wolf, M.; Weimann, L.; Schulze, N.; Li, F.; Kaschani, F.; Riemer, A.; Zierhut, C.; Kaiser, M.; Iliakis, G.; Funabiki, H.; Meyer, H. VCP/P97 Extracts Sterically Trapped Ku70/80 Rings from DNA in Double Strand Break Repair. *Mol Cell* **2016**, *64* (1), 189–198. <https://doi.org/10.1016/j.molcel.2016.08.037>.
- (56) Chanut, P.; Britton, S.; Coates, J.; Jackson, S. P.; Calsou, P. Coordinated Nuclease Activities Counteract Ku at Single-Ended DNA Double-Strand Breaks. *Nat Commun* **2016**, *7*, 12889. <https://doi.org/10.1038/ncomms12889>.
- (57) Chung, W.-H.; Zhu, Z.; Papusha, A.; Malkova, A.; Ira, G. Defective Resection at DNA Double-Strand Breaks Leads to De Novo Telomere Formation and Enhances Gene Targeting. *PLoS Genet* **2010**, *6* (5), e1000948. <https://doi.org/10.1371/journal.pgen.1000948>.
- (58) Zhao, W.; Steinfeld, J. B.; Liang, F.; Chen, X.; Maranon, D. G.; Ma, C. J.; Kwon, Y.; Rao, T.; Wang, W.; Chen, S.; Song, X.; Deng, Y.; Jimenez-Sainz, J.; Lu, L.; Jensen, R. B.; Xiong, Y.; Kupfer, G. M.; Wiese, C.; Greene, E. C.; Sung, P. Promotion of RAD51-Mediated Homologous DNA Pairing by BRCA1-BARD1. *Nature* **2017**, *550* (7676), 360–365. <https://doi.org/10.1038/nature24060>.
- (59) van der Heijden, T.; Modesti, M.; Hage, S.; Kanaar, R.; Wyman, C.; Dekker, C. Homologous Recombination in Real Time: DNA Strand Exchange by RecA. *Molecular Cell* **2008**, *30* (4), 530–538. <https://doi.org/10.1016/j.molcel.2008.03.010>.
- (60) Sarbajna, S.; West, S. C. Holliday Junction Processing Enzymes as Guardians of Genome Stability. *Trends Biochem Sci* **2014**, *39* (9), 409–419. <https://doi.org/10.1016/j.tibs.2014.07.003>.
- (61) Pâques, F.; Haber, J. E. Multiple Pathways of Recombination Induced by Double-Strand Breaks in *Saccharomyces Cerevisiae*. *Microbiol Mol Biol Rev* **1999**, *63* (2), 349–404.
- (62) Ciccia, A.; Elledge, S. J. The DNA Damage Response: Making It Safe to Play with Knives. *Mol Cell* **2010**, *40* (2), 179–204. <https://doi.org/10.1016/j.molcel.2010.09.019>.

References

- (63) Rastogi, R. P.; Richa; Kumar, A.; Tyagi, M. B.; Sinha, R. P. Molecular Mechanisms of Ultraviolet Radiation-Induced DNA Damage and Repair. *J Nucleic Acids* **2010**, *2010*, 592980. <https://doi.org/10.4061/2010/592980>.
- (64) Mavragani, I. V.; Nikitaki, Z.; Kalospyros, S. A.; Georgakilas, A. G. Ionizing Radiation and Complex DNA Damage: From Prediction to Detection Challenges and Biological Significance. *Cancers (Basel)* **2019**, *11* (11), 1789. <https://doi.org/10.3390/cancers11111789>.
- (65) Goldberg, I. H. Free Radical Mechanisms in Neocarzinostatin-Induced DNA Damage. *Free Radical Biology and Medicine* **1987**, *3* (1), 41–54. [https://doi.org/10.1016/0891-5849\(87\)90038-4](https://doi.org/10.1016/0891-5849(87)90038-4).
- (66) Edo, K.; Koide, Y. Neocarzinostatin Chromophore: Structure and Mechanism of DNA Cleavage. In *Neocarzinostatin: The Past, Present, and Future of an Anticancer Drug*; Maeda, H., Edo, K., Ishida, N., Eds.; Springer Japan: Tokyo, 1997; pp 23–45. https://doi.org/10.1007/978-4-431-66914-2_3.
- (67) Yamauchi, T.; Yoshida, A.; Ueda, T. Camptothecin Induces DNA Strand Breaks and Is Cytotoxic in Stimulated Normal Lymphocytes. *Oncol Rep* **2011**, *25* (2), 347–352. <https://doi.org/10.3892/or.2010.1100>.
- (68) Montecucco, A.; Zanetta, F.; Biamonti, G. Molecular Mechanisms of Etoposide. *EXCLI J* **2015**, *14*, 95–108. <https://doi.org/10.17179/excli2015-561>.
- (69) Andrin, C.; McDonald, D.; Attwood, K. M.; Rodrigue, A.; Ghosh, S.; Mirzayans, R.; Masson, J.-Y.; Dellaire, G.; Hendzel, M. J. A Requirement for Polymerized Actin in DNA Double-Strand Break Repair. *Nucleus* **2012**, *3* (4), 384–395. <https://doi.org/10.4161/nucl.21055>.
- (70) Torgovnick, A.; Schumacher, B. DNA Repair Mechanisms in Cancer Development and Therapy. *Front Genet* **2015**, *6*, 157. <https://doi.org/10.3389/fgene.2015.00157>.
- (71) Hustedt, N.; Gasser, S. M.; Shimada, K. Replication Checkpoint: Tuning and Coordination of Replication Forks in S Phase. *Genes (Basel)* **2013**, *4* (3), 388–434. <https://doi.org/10.3390/genes4030388>.
- (72) Roos, W. P.; Kaina, B. DNA Damage-Induced Cell Death by Apoptosis. *Trends Mol Med* **2006**, *12* (9), 440–450. <https://doi.org/10.1016/j.molmed.2006.07.007>.
- (73) Hernandez-Segura, A.; Nehme, J.; Demaria, M. Hallmarks of Cellular Senescence. *Trends in Cell Biology* **2018**, *28* (6), 436–453. <https://doi.org/10.1016/j.tcb.2018.02.001>.
- (74) Gorgoulis, V.; Adams, P. D.; Alimonti, A.; Bennett, D. C.; Bischof, O.; Bishop, C.; Campisi, J.; Collado, M.; Evangelou, K.; Ferbeyre, G.; Gil, J.; Hara, E.; Krizhanovskiy, V.; Jurk, D.; Maier, A. B.; Narita, M.; Niedernhofer, L.; Passos, J. F.; Robbins, P. D.; Schmitt, C. A.; Sedivy, J.; Vougas, K.; von Zglinicki, T.; Zhou, D.; Serrano, M.; Demaria, M. Cellular Senescence: Defining a Path Forward. *Cell* **2019**, *179* (4), 813–827. <https://doi.org/10.1016/j.cell.2019.10.005>.
- (75) Fumagalli, M.; Rossiello, F.; Mondello, C.; d'Adda di Fagagna, F. Stable Cellular Senescence Is Associated with Persistent DDR Activation. *PLoS One* **2014**, *9* (10), e110969. <https://doi.org/10.1371/journal.pone.0110969>.
- (76) Dulić, V.; Beney, G.-E.; Frebourg, G.; Drullinger, L. F.; Stein, G. H. Uncoupling between Phenotypic Senescence and Cell Cycle Arrest in Aging P21-Deficient Fibroblasts. *Mol Cell Biol* **2000**, *20* (18), 6741–6754.
- (77) Coppé, J.-P.; Patil, C. K.; Rodier, F.; Sun, Y.; Muñoz, D. P.; Goldstein, J.; Nelson, P. S.; Desprez, P.-Y.; Campisi, J. Senescence-Associated Secretory Phenotypes Reveal Cell-Nonautonomous Functions of Oncogenic RAS and the P53 Tumor Suppressor. *PLoS Biol* **2008**, *6* (12), e301. <https://doi.org/10.1371/journal.pbio.0060301>.
- (78) Coppé, J.-P.; Patil, C. K.; Rodier, F.; Krtolica, A.; Beauséjour, C. M.; Parrinello, S.; Hodgson, J. G.; Chin, K.; Desprez, P.-Y.; Campisi, J. A Human-Like Senescence-

References

- Associated Secretory Phenotype Is Conserved in Mouse Cells Dependent on Physiological Oxygen. *PLoS One* **2010**, *5* (2), e9188. <https://doi.org/10.1371/journal.pone.0009188>.
- (79) Eren, M.; Boe, A. E.; Murphy, S. B.; Place, A. T.; Nagpal, V.; Morales-Nebreda, L.; Ulrich, D.; Quaggin, S. E.; Budinger, G. R. S.; Mutlu, G. M.; Miyata, T.; Vaughan, D. E. PAI-1-Regulated Extracellular Proteolysis Governs Senescence and Survival in Klotho Mice. *Proc Natl Acad Sci U S A* **2014**, *111* (19), 7090–7095. <https://doi.org/10.1073/pnas.1321942111>.
- (80) Özcan, S.; Alessio, N.; Acar, M. B.; Mert, E.; Omerli, F.; Peluso, G.; Galderisi, U. Unbiased Analysis of Senescence Associated Secretory Phenotype (SASP) to Identify Common Components Following Different Genotoxic Stresses. *Aging (Albany NY)* **2016**, *8* (7), 1316–1327. <https://doi.org/10.18632/aging.100971>.
- (81) McHugh, D.; Gil, J. Senescence and Aging: Causes, Consequences, and Therapeutic Avenues. *J Cell Biol* **2018**, *217* (1), 65–77. <https://doi.org/10.1083/jcb.201708092>.
- (82) Di Micco, R.; Krizhanovsky, V.; Baker, D.; d’Adda di Fagagna, F. Cellular Senescence in Ageing: From Mechanisms to Therapeutic Opportunities. *Nat Rev Mol Cell Biol* **2021**, *22* (2), 75–95. <https://doi.org/10.1038/s41580-020-00314-w>.
- (83) Magistrati, E.; Maestrini, G.; Niño, C. A.; Lince-Faria, M.; Beznoussenko, G.; Mironov, A.; Maspero, E.; Bettencourt-Dias, M.; Polo, S. Myosin VI Regulates Ciliogenesis by Promoting the Turnover of the Centrosomal/Satellite Protein OFD1. *EMBO Rep* **2022**, *23* (3), e54160. <https://doi.org/10.15252/embr.202154160>.
- (84) Franken, N. A. P.; Rodermond, H. M.; Stap, J.; Haveman, J.; van Bree, C. Clonogenic Assay of Cells in Vitro. *Nat Protoc* **2006**, *1* (5), 2315–2319. <https://doi.org/10.1038/nprot.2006.339>.
- (85) Buch, K.; Peters, T.; Nawroth, T.; Sängler, M.; Schmidberger, H.; Langguth, P. Determination of Cell Survival after Irradiation via Clonogenic Assay versus Multiple MTT Assay - A Comparative Study. *Radiation Oncology* **2012**, *7* (1), 1. <https://doi.org/10.1186/1748-717X-7-1>.
- (86) Ibrahim, A. F. M.; Shen, L.; Tatham, M. H.; Dickerson, D.; Prescott, A. R.; Abidi, N.; Xirodimas, D. P.; Hay, R. T. Antibody RING-Mediated Destruction of Endogenous Proteins. *Mol Cell* **2020**, *79* (1), 155-166.e9. <https://doi.org/10.1016/j.molcel.2020.04.032>.
- (87) Ju Shin, Y.; Kyun Park, S.; Jung Jung, Y.; Na Kim, Y.; Sung Kim, K.; Kyu Park, O.; Kwon, S.-H.; Ho Jeon, S.; Trinh, L. A.; Fraser, S. E.; Kee, Y.; Joon Hwang, B. Nanobody-Targeted E3-Ubiquitin Ligase Complex Degrades Nuclear Proteins. *Sci Rep* **2015**, *5* (1), 14269. <https://doi.org/10.1038/srep14269>.
- (88) Bennetzen, M. V.; Kosar, M.; Bunkenborg, J.; Payne, M. R.; Bartkova, J.; Lindström, M. S.; Lukas, J.; Andersen, J. S.; Bartek, J.; Larsen, D. H. DNA Damage-Induced Dynamic Changes in Abundance and Cytosol-Nuclear Translocation of Proteins Involved in Translational Processes, Metabolism, and Autophagy. *Cell Cycle* **2018**, *17* (17), 2146–2163. <https://doi.org/10.1080/15384101.2018.1515552>.
- (89) Vélez-Cruz, R.; Manickavinayam, S.; Biswas, A. K.; Clary, R. W.; Premkumar, T.; Cole, F.; Johnson, D. G. RB Localizes to DNA Double-Strand Breaks and Promotes DNA End Resection and Homologous Recombination through the Recruitment of BRG1. *Genes Dev* **2016**, *30* (22), 2500–2512. <https://doi.org/10.1101/gad.288282.116>.
- (90) Rando, O. J.; Zhao, K.; Janmey, P.; Crabtree, G. R. Phosphatidylinositol-Dependent Actin Filament Binding by the SWI/SNF-like BAF Chromatin Remodeling Complex. *Proceedings of the National Academy of Sciences* **2002**, *99* (5), 2824–2829. <https://doi.org/10.1073/pnas.032662899>.
- (91) Shtutman, M.; Chang, B.-D.; Schools, G. P.; Broude, E. V. Cellular Model of P21-Induced Senescence. *Methods Mol Biol* **2017**, *1534*, 31–39. https://doi.org/10.1007/978-1-4939-6670-7_3.

References

- (92) Rayess, H.; Wang, M. B.; Srivatsan, E. S. Cellular Senescence and Tumor Suppressor Gene P16. *Int J Cancer* **2012**, *130* (8), 1715–1725. <https://doi.org/10.1002/ijc.27316>.
- (93) Campos, A.; Clemente-Blanco, A. Cell Cycle and DNA Repair Regulation in the Damage Response: Protein Phosphatases Take Over the Reins. *Int J Mol Sci* **2020**, *21* (2), 446. <https://doi.org/10.3390/ijms21020446>.
- (94) Ashley, A. K.; Shrivastav, M.; Nie, J.; Amerin, C.; Troksa, K.; Glanzer, J. G.; Liu, S.; Opiyo, S. O.; Dimitrova, D. D.; Le, P.; Sishc, B.; Bailey, S. M.; Oakley, G. G.; Nickoloff, J. A. DNA-PK Phosphorylation of RPA32 Ser4/Ser8 Regulates Replication Stress Checkpoint Activation, Fork Restart, Homologous Recombination and Mitotic Catastrophe. *DNA Repair (Amst)* **2014**, *21*, 131–139. <https://doi.org/10.1016/j.dnarep.2014.04.008>.
- (95) Citterio, E. Fine-Tuning the Ubiquitin Code at DNA Double-Strand Breaks: Deubiquitinating Enzymes at Work. *Front Genet* **2015**, *6*, 282. <https://doi.org/10.3389/fgene.2015.00282>.
- (96) Shao, Z.; Davis, A. J.; Fattah, K. R.; So, S.; Sun, J.; Lee, K.-J.; Harrison, L.; Yang, J.; Chen, D. J. Persistently Bound Ku at DNA Ends Attenuates DNA End Resection and Homologous Recombination. *DNA Repair (Amst)* **2012**, *11* (3), 310–316. <https://doi.org/10.1016/j.dnarep.2011.12.007>.
- (97) Wang, T.; Du, X.-H.; Hong, Y.; Hong, X.; Fan, L.; Zhou, J.-W.; Sun, H.; Ge, J.; Billadeau, D. D.; Deng, Z.-H. WASH Interacts with Ku to Regulate DNA Double-Stranded Break Repair. *iScience* **2021**, *25* (1), 103676. <https://doi.org/10.1016/j.isci.2021.103676>.
- (98) Linardopoulou, E. V.; Parghi, S. S.; Friedman, C.; Osborn, G. E.; Parkhurst, S. M.; Trask, B. J. Human Subtelomeric WASH Genes Encode a New Subclass of the WASP Family. *PLoS Genet* **2007**, *3* (12), e237. <https://doi.org/10.1371/journal.pgen.0030237>.
- (99) Liu, R.; Abreu-Blanco, M. T.; Barry, K. C.; Linardopoulou, E. V.; Osborn, G. E.; Parkhurst, S. M. Wash Functions Downstream of Rho and Links Linear and Branched Actin Nucleation Factors. *Development* **2009**, *136* (16), 2849–2860. <https://doi.org/10.1242/dev.035246>.
- (100) Maria Dilia Palumbieri; Chiara Merigliano; Daniel González Acosta; Thomas von Känel; Bettina Welter; Henriette Stoy; Jana Krietsch; Svenja Ulferts; Andrea Sanchi; Robert Grosse; Irene Chiolo; Massimo Lopes. Replication Fork Plasticity upon Replication Stress Requires Rapid Nuclear Actin Polymerization | BioRxiv. bioRxiv. <https://doi.org/10.1101/2023.03.24.534097>.
- (101) Baarlink, C.; Plessner, M.; Sherrard, A.; Morita, K.; Misu, S.; Virant, D.; Kleinschnitz, E.-M.; Harniman, R.; Alibhai, D.; Baumeister, S.; Miyamoto, K.; Endesfelder, U.; Kaidi, A.; Grosse, R. A Transient Pool of Nuclear F-Actin at Mitotic Exit Controls Chromatin Organization. *Nat Cell Biol* **2017**, *19* (12), 1389–1399. <https://doi.org/10.1038/ncb3641>.
- (102) Percipalle, P.; Fomproix, N.; Cavellán, E.; Voit, R.; Reimer, G.; Krüger, T.; Thyberg, J.; Scheer, U.; Grummt, I.; Östlund Farrants, A.-K. The Chromatin Remodelling Complex WSTF–SNF2h Interacts with Nuclear Myosin 1 and Has a Role in RNA Polymerase I Transcription. *EMBO Rep* **2006**, *7* (5), 525–530. <https://doi.org/10.1038/sj.embor.7400657>.
- (103) Miller, K. G. Converting a Motor to an Anchor. *Cell* **2004**, *116* (5), 635–636. [https://doi.org/10.1016/s0092-8674\(04\)00213-2](https://doi.org/10.1016/s0092-8674(04)00213-2).
- (104) Meyer, H.; van den Boom, J. Targeting of Client Proteins to the VCP/P97/Cdc48 Unfolding Machine. *Front Mol Biosci* **2023**, *10*, 1142989. <https://doi.org/10.3389/fmolb.2023.1142989>.
- (105) Bodnar, N. O.; Rapoport, T. A. Molecular Mechanism of Substrate Processing by the Cdc48 ATPase Complex. *Cell* **2017**, *169* (4), 722–735.e9. <https://doi.org/10.1016/j.cell.2017.04.020>.
- (106) Weith, M.; Seiler, J.; van den Boom, J.; Kracht, M.; Hülsmann, J.; Primorac, I.; Del Pino Garcia, J.; Kaschani, F.; Kaiser, M.; Musacchio, A.; Bollen, M.; Meyer, H. Ubiquitin-

References

- Independent Disassembly by a P97 AAA-ATPase Complex Drives PP1 Holoenzyme Formation. *Mol Cell* **2018**, *72* (4), 766-777.e6. <https://doi.org/10.1016/j.molcel.2018.09.020>.
- (107) van den Boom, J.; Kueck, A. F.; Kravic, B.; Müschenborn, H.; Giesing, M.; Pan, D.; Kaschani, F.; Kaiser, M.; Musacchio, A.; Meyer, H. Targeted Substrate Loop Insertion by VCP/P97 during PP1 Complex Disassembly. *Nat Struct Mol Biol* **2021**, *28* (12), 964–971. <https://doi.org/10.1038/s41594-021-00684-5>.
- (108) Quinet, A.; Lemaçon, D.; Vindigni, A. Replication Fork Reversal: Players and Guardians. *Mol Cell* **2017**, *68* (5), 830–833. <https://doi.org/10.1016/j.molcel.2017.11.022>.
- (109) Audoynaud, C.; Schirmeisen, K.; Saada, A. A.; Gesnik, A.; Fernández-Varela, P.; Boucherit, V.; Ropars, V.; Chaudhuri, A.; Fréon, K.; Charbonnier, J.-B.; Lambert, S. A. E. RNA:DNA Hybrids from Okazaki Fragments Contribute to Establish the Ku-Mediated Barrier to Replication-Fork Degradation. *Molecular Cell* **2023**, *83* (7), 1061-1074.e6. <https://doi.org/10.1016/j.molcel.2023.02.008>.
- (110) Teixeira-Silva, A.; Ait Saada, A.; Hardy, J.; Iraqui, I.; Nocente, M. C.; Fréon, K.; Lambert, S. A. E. The End-Joining Factor Ku Acts in the End-Resection of Double Strand Break-Free Arrested Replication Forks. *Nat Commun* **2017**, *8* (1), 1982. <https://doi.org/10.1038/s41467-017-02144-5>.
- (111) Zahid, S.; Seif El Dahan, M.; Iehl, F.; Fernandez-Varela, P.; Le Du, M.-H.; Ropars, V.; Charbonnier, J. B. The Multifaceted Roles of Ku70/80. *International Journal of Molecular Sciences* **2021**, *22* (8), 4134. <https://doi.org/10.3390/ijms22084134>.
- (112) Warner, C. L.; Stewart, A.; Luzio, J. P.; Steel, K. P.; Libby, R. T.; Kendrick-Jones, J.; Buss, F. Loss of Myosin VI Reduces Secretion and the Size of the Golgi in Fibroblasts from Snell's Waltzer Mice. *EMBO J* **2003**, *22* (3), 569–579. <https://doi.org/10.1093/emboj/cdg055>.
- (113) Liu, S.; Matsui, T. S.; Kang, N.; Deguchi, S. Analysis of Senescence-Responsive Stress Fiber Proteome Reveals Reorganization of Stress Fibers Mediated by Elongation Factor EEF2 in HFF-1 Cells. *MBoC* **2022**, *33* (1), ar10. <https://doi.org/10.1091/mbc.E21-05-0229>.
- (114) Moujaber, O.; Fishbein, F.; Omran, N.; Liang, Y.; Colmegna, I.; Presley, J. F.; Stochaj, U. Cellular Senescence Is Associated with Reorganization of the Microtubule Cytoskeleton. *Cell Mol Life Sci* **2019**, *76* (6), 1169–1183. <https://doi.org/10.1007/s00018-018-2999-1>.
- (115) Mu, X.; Tseng, C.; Hambright, W. S.; Matre, P.; Lin, C.-Y.; Chanda, P.; Chen, W.; Gu, J.; Ravuri, S.; Cui, Y.; Zhong, L.; Cooke, J. P.; Niedernhofer, L. J.; Robbins, P. D.; Huard, J. Cytoskeleton Stiffness Regulates Cellular Senescence and Innate Immune Response in Hutchinson–Gilford Progeria Syndrome. *Aging Cell* **2020**, *19* (8), e13152. <https://doi.org/10.1111/acel.13152>.
- (116) Santos, C. V.; Rogers, S. L.; Carter, A. P. CryoET Shows Cofilactin Filaments inside the Microtubule Lumen. *bioRxiv* March 31, 2023, p 2023.03.31.535077. <https://doi.org/10.1101/2023.03.31.535077>.
- (117) Paul, D. M.; Mantell, J.; Borucu, U.; Coombs, J.; Surridge, K. J.; Squire, J. M.; Verkade, P.; Dodding, M. P. In Situ Cryo-Electron Tomography Reveals Filamentous Actin within the Microtubule Lumen. *Journal of Cell Biology* **2020**, *219* (9), e201911154. <https://doi.org/10.1083/jcb.201911154>.
- (118) Panier, S. Cancer Cells Remodel Nuclear Actin Filaments to Resist Chemotherapy. *Nature* **2023**, *616* (7955), 40–42. <https://doi.org/10.1038/d41586-023-00801-y>.
- (119) Debaugnies, M.; Rodríguez-Acebes, S.; Blondeau, J.; Parent, M.-A.; Zocco, M.; Song, Y.; de Maertelaer, V.; Moers, V.; Latil, M.; Dubois, C.; Coulonval, K.; Impens, F.; Van Haver, D.; Dufour, S.; Uemura, A.; Sotiropoulou, P. A.; Méndez, J.; Blanpain, C. RHOJ Controls EMT-Associated Resistance to Chemotherapy. *Nature* **2023**, *616* (7955), 168–175. <https://doi.org/10.1038/s41586-023-05838-7>.

10. Appendix

10.1 Supplementary figures

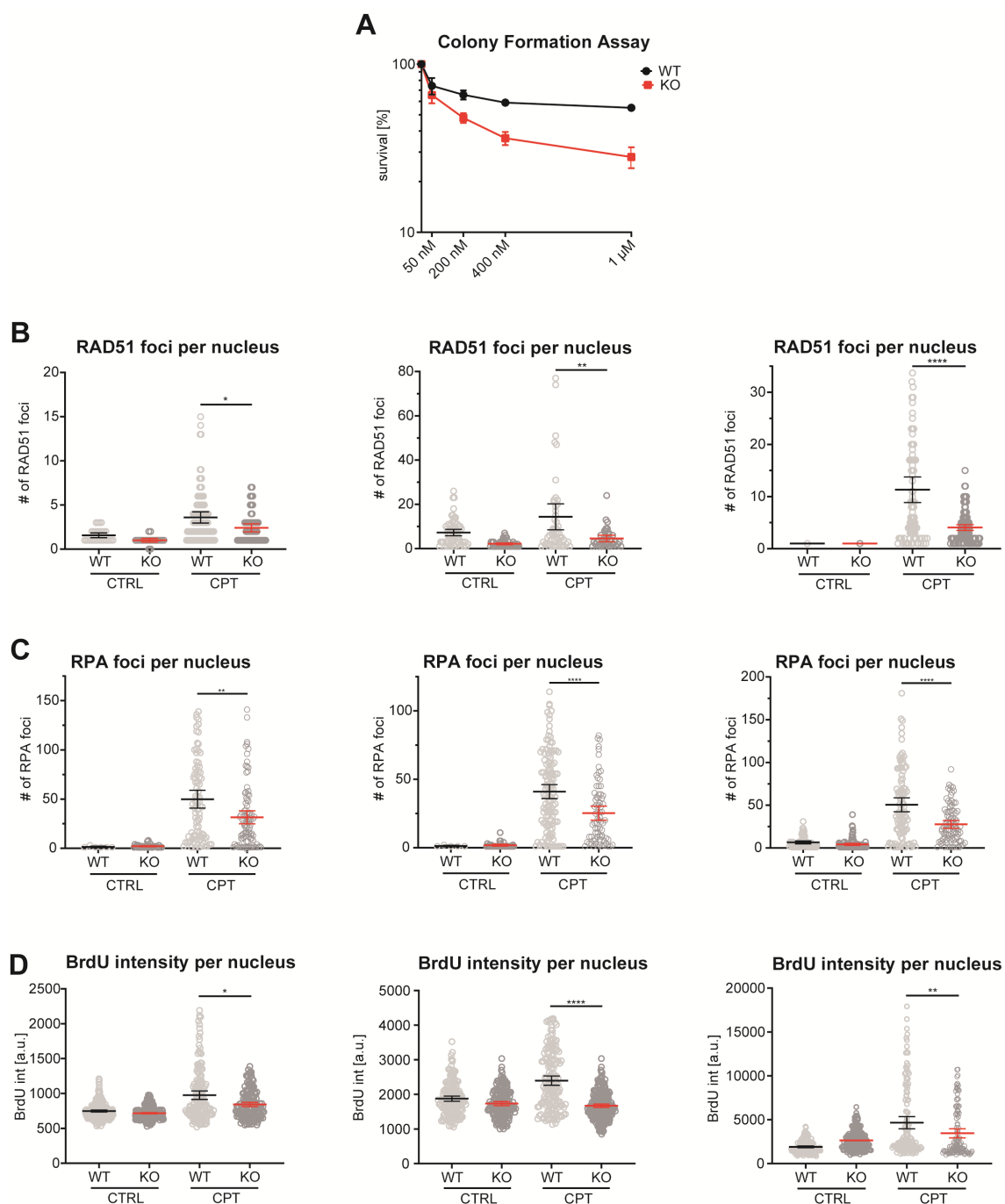


Figure S1: Knockout of Myo6 results in impaired survival and decreased HDR marker levels upon CPT
 A549 *wildtype* (WT) and *Myo6 knockout* (KO) cells were treated with 1 μ M camptothecin (CPT) for 1 h (A-D).

(A) Colony Formation Assay show lower survival in KO cells. Cells were treated with indicated concentrations of CPT and then reseeded (in triplicates) into 10 cm petri dishes. After 10 days, they were counted manually. The graph shows mean and standard error of the mean (SEM) of three independent experiments.

Appendix

(B) Rad51 immunofluorescence staining (IF) shows a lower foci number in KO cells. After treatment, cells recovered for 20 hours and were then stained with Rad51-specific antibodies. Dot plots of number of Rad51 foci per nucleus with mean values \pm 95% confidence intervals. Significance levels were calculated using the students t-test from at least 100 nuclei per sample (ns: non-significant, ****: $p < 0.0001$, ***: $p < 0.001$, *: $p < 0.05$). Three independent replicates are shown.

(C) RPA IF shows less RPA foci in KO cells. After treatment of 1h, cells were pre-extracted and stained with RPA specific antibodies. Dot plots of RPA foci number per nucleus with mean values \pm 95% confidence intervals. Significance levels were calculated using the students t-test from at least 100 nuclei per sample (ns: non-significant, ****: $p < 0.0001$, ***: $p < 0.001$, *: $p < 0.05$). Three independent replicates are shown.

(E) BrdU IF shows less BrdU intensity in KO cells. After a 24 h pre-treatment with 10 ng/ml BrdU, cells were treated with CPT, pre-extracted and following stained with BrdU specific antibodies. The properties of the graph are the same as in (B). Three independent replicates are shown.

Appendix

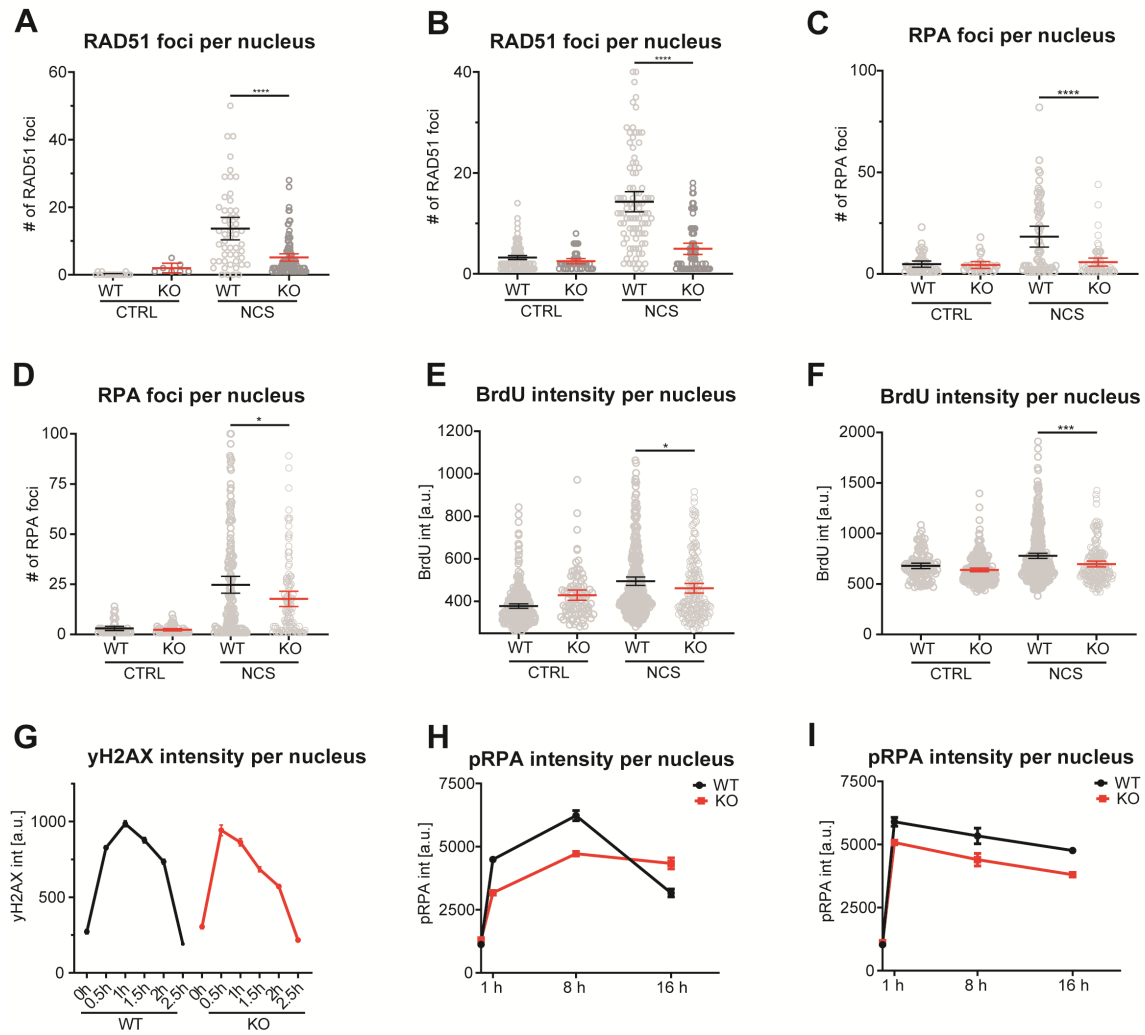


Figure S2: Replicates of figure 6: Knockout of Myo6 results in impaired survival and decreased HDR marker levels upon NCS

A549 *wildtype* (WT) and *Myo6 knockout* (KO) cells were treated with 0.5 mg/ml neocarzinostatin (NCS) for 1 h (A-J).

(A/B) Rad51 immunofluorescence staining (IF) shows a lower foci number in KO cells. After treatment, cells recovered for 8 hours and were then stained with Rad51-specific antibodies. Dot plots of number of Rad51 foci per nucleus with mean values \pm 95% confidence intervals. Significance levels were calculated using the students t-test from at least 100 nuclei per sample (ns: non-significant, ****: $p < 0.0001$, ***: $p < 0.001$, *: $p < 0.05$). Two independent replicates are shown.

(C/D) RPA IF shows less RPA foci in KO cells. After treatment of 1h, cells were pre-extracted and stained with RPA specific antibodies. Dot plots of RPA foci number per nucleus with mean values \pm 95% confidence intervals. Significance levels were calculated using the students t-test from at least 100 nuclei per sample (ns: non-significant, ****: $p < 0.0001$, ***: $p < 0.001$, *: $p < 0.05$). Two independent replicates are shown.

(E/F) BrdU IF shows less BrdU intensity in KO cells. After a 24 h pre-treatment with 10 ng/ml BrdU, cells were treated with CPT, pre-extracted and following stained with BrdU specific antibodies. The properties of the graph are the same as in (A/B). Two independent replicates are shown.

(G) γ H2AX IF kinetic shows no differences between WT and KO cells. At 0 h timepoint, NCS was added and after 1h cells were washed and the γ H2AX foci resolution was monitored. The graph show the mean with SEM. One independent replicate is shown.

(H/I) pRPA (S33) IF kinetics show no delay in KO cells, but a decrease in pRPA (S33) intensity. At 0 h timepoint, NCS was added and after 1 h it was removed and the decrease of pRPA (S33) was monitored. The graph show the mean with SEM. Two independent replicates are shown.

Appendix

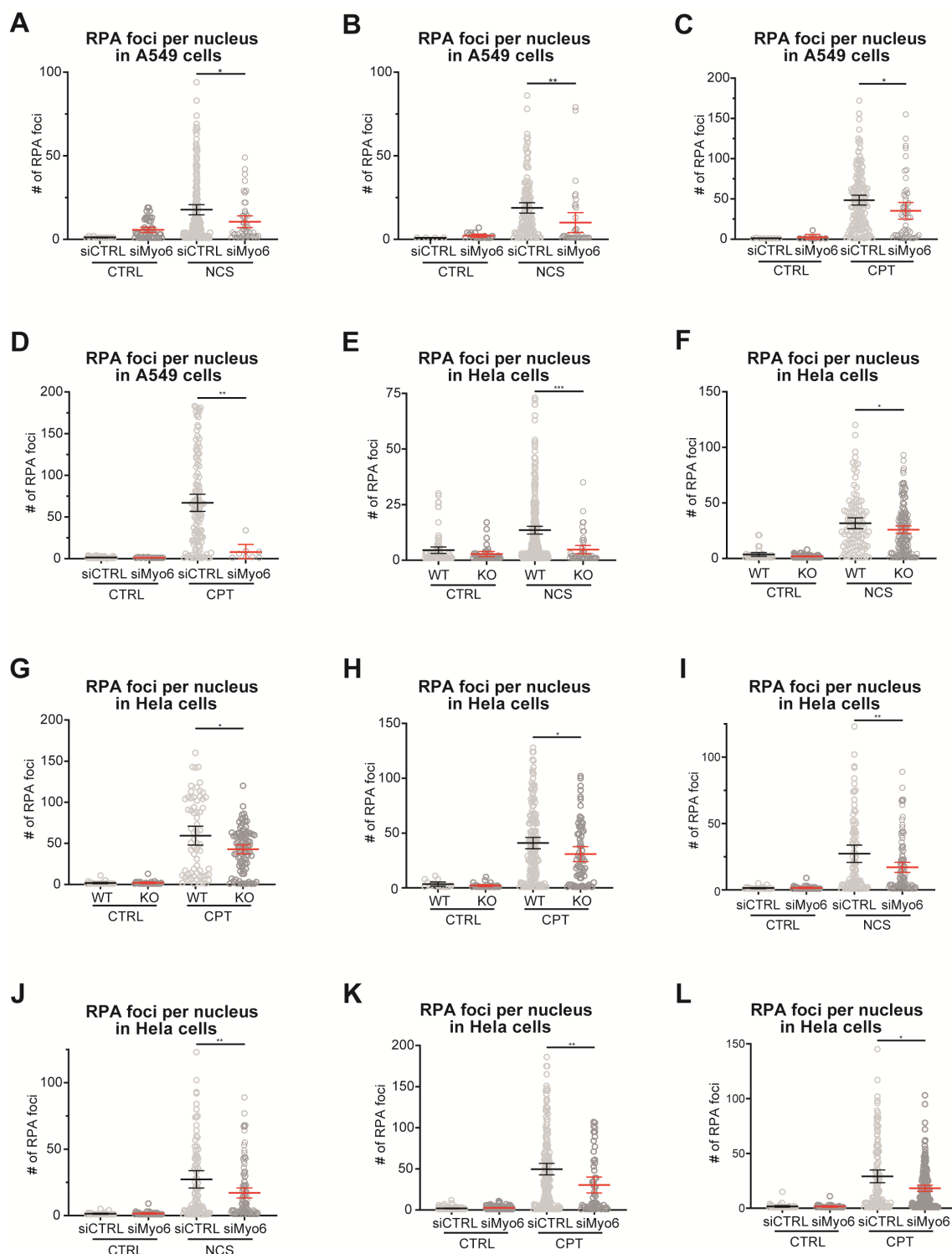


Figure S3: Replicates of figure 7: RPA phenotype is conserved in A549 / HeLa cells after KO or KD upon CPT and NCS

(A-D) A549 A549 WT cells show reduced RPA foci number after KD of Myo6 upon CPT and NCS. A549 WT cells were treated with siRNA control (siCTRL) and siRNA Myo6 (siMyo6). DNA damage was induced (as indicated) with NCS or CPT. After treatment of 1h, cells were pre-extracted, fixed and stained with RPA specific antibodies. Dot plots show number of RPA foci per nucleus with mean values \pm 95% confidence intervals. Significance levels were calculated using the students t-test from at least 100 nuclei per sample (ns: non-significant, ****: $p < 0.0001$, ***: $p < 0.001$, *: $p < 0.05$). Two independent replicates are shown.

Appendix

(E-H) HeLa cells show reduced number of RPA foci after Myo6 KO, upon NCS and CPT. DNA damage to HeLa WT and KO cells was induced (as indicated) with NCS or CPT. The staining and evaluation were performed as in (A-D). Two independent replicates are shown.

(I-L) HeLa WT cells show reduced RPA foci number after KD of Myo6 upon CPT and NCS. HeLa WT cells were treated with siRNA control (siCTRL) and siRNA Myo6 (siMyo6). DNA damage was induced (as indicated) with NCS or CPT. The staining and evaluation were performed as in (A-D). Two independent replicates are shown.

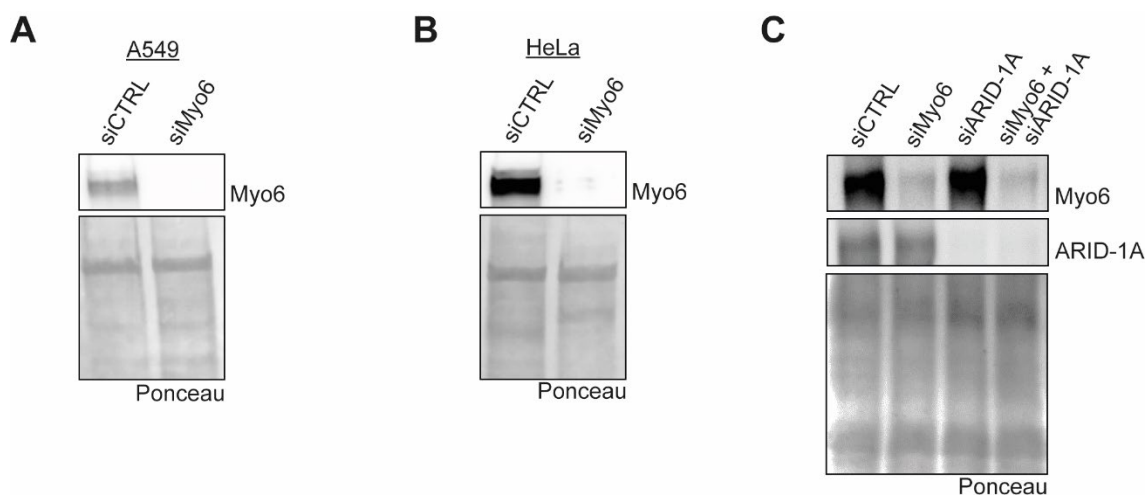


Figure S 4: representative Western blots for KD efficiency in A549 and HeLa cells

(A) A549 WT cells were treated with siRNA control (siCTRL) and siRNA Myo6 (siMyo6). Cell lysate was analyzed using Western blot with Myo6 specific antibodies and Ponceau as loading control.

(B) HeLa WT cells were treated with siRNA control (siCTRL) and siRNA Myo6 (siMyo6). Cell lysate was analyzed using Western blot with Myo6 specific antibodies and Ponceau as loading control.

(C) A549 WT cells were treated with siRNA control (siCTRL), siRNA Myo6 (siMyo6), siRNA ARID-1A and a combination of siMyo6 and siARID-1A. Cell lysate was analyzed using Western blot with Myo6 and ARID-1A specific antibodies and Ponceau as loading control.

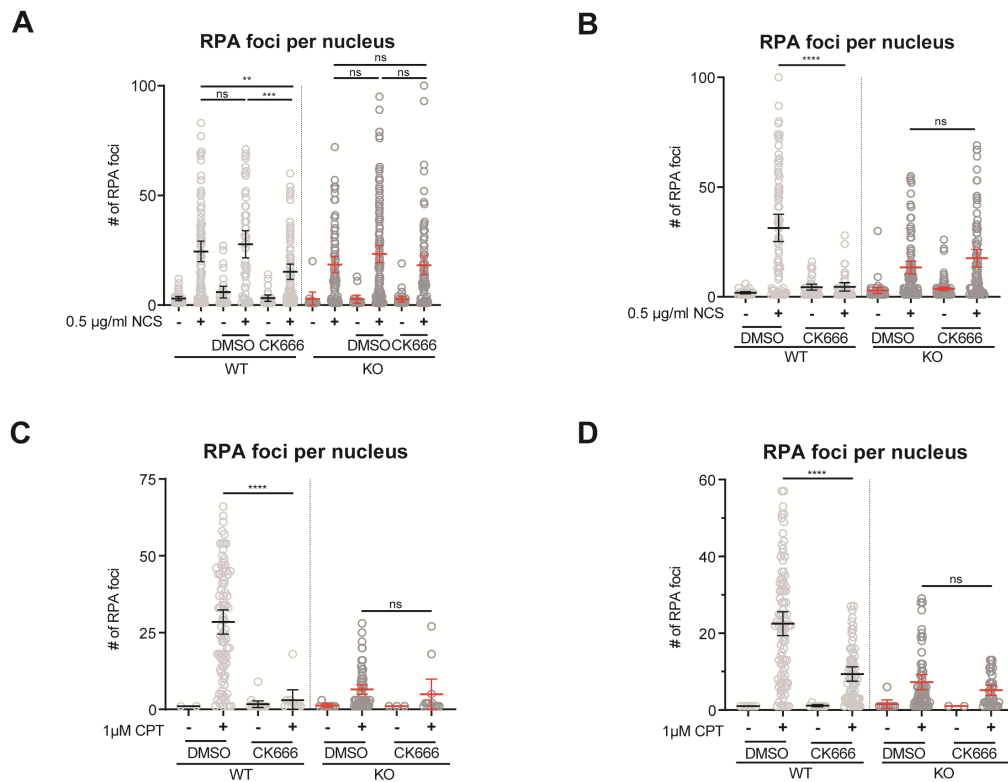


Figure S5: Replicates of figure 7: Epistasis upon actin polymerisation inhibition and Myo6 knockout
 (A-D) A549 cells show epistasis upon Myo6 KO and CK666 treatment after NCS or CPT treatment. A549 WT and KO cells were pre-treated with DMSO or CK666 for 30 minutes and then treated for 1 h with 1 µM CPT or 0.5 µg/ml NCS to induce DNA damage. Cells were pre-extracted, fixed and stained with RPA specific antibodies. Dot plots show number of RPA foci per nucleus with mean values \pm 95% confidence intervals. Significance levels were calculated using the students t-test from at least 100 nuclei per sample (ns: non-significant, ****: $p < 0.0001$, ***: $p < 0.001$, *: $p < 0.05$). Two independent replicates are shown.

Appendix

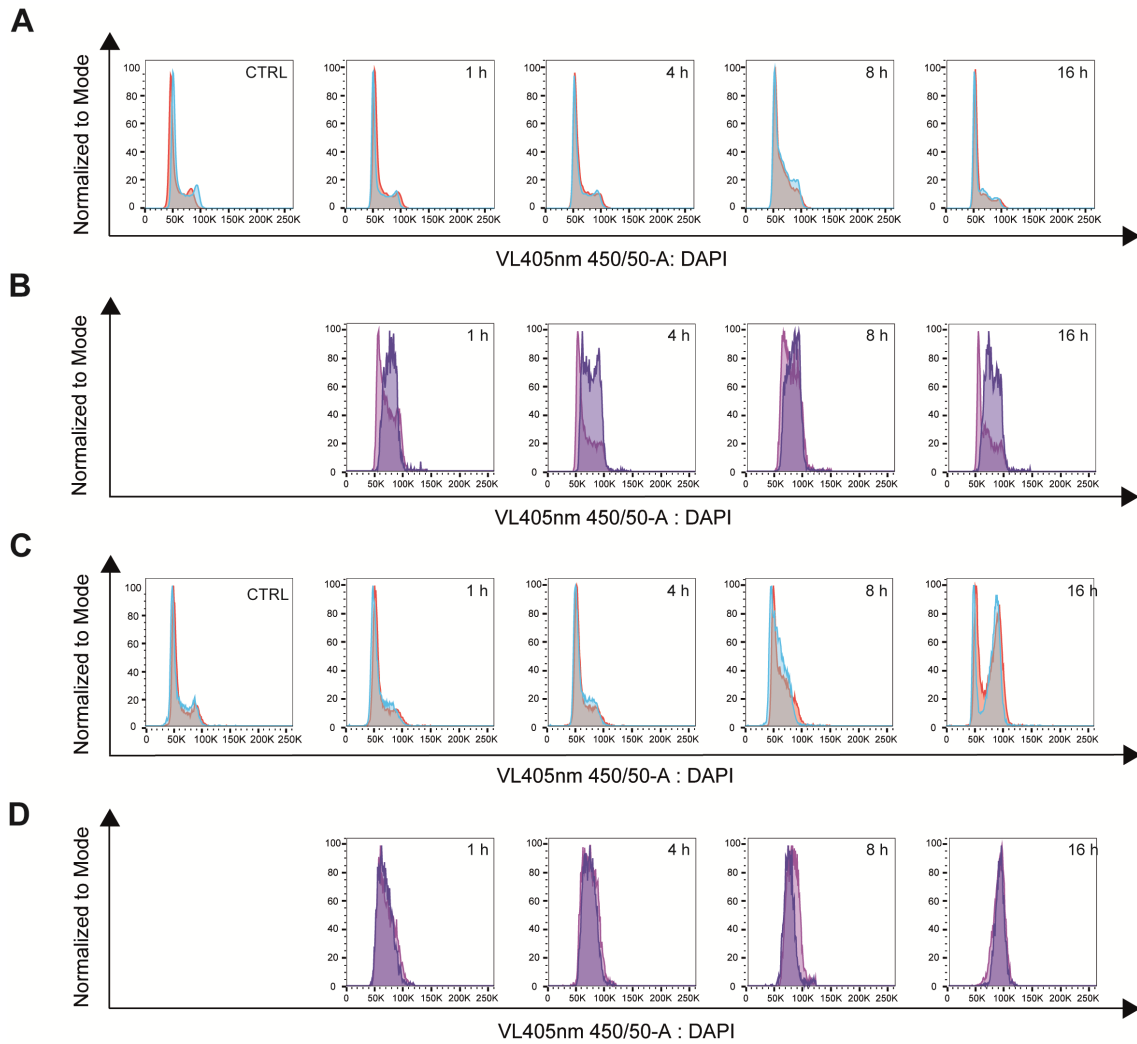


Figure S 6: Replicates of figure 8: Myo6 depletion leads to different behaviour in cell cycle progression in A549 cells upon CPT treatment

A549 WT and KO cells were treated for 20 min with 10 μ M EdU, next 1 μ M of CPT was added for 1 h. Cells were then washed with PBS, harvested and fixed in PFA (1h) or released in fresh medium for 4h, 8h and 16h and harvested and fixed in PFA. Staining were performed using DAPI and EdU click reaction and evaluated using Flow cytometry. The number of WT and KO cells was adjusted to each other. Two independent replicates are shown.

(A/C) A549 KO cells show no cell cycle slow down upon CPT treatment. Cell cycle profile overlay of A549 WT (blue) and KO (red) cells at indicated timepoints.

(B/D) Overlay of EdU positive WT (magenta) and EdU positive KO (purple) cells.

Appendix

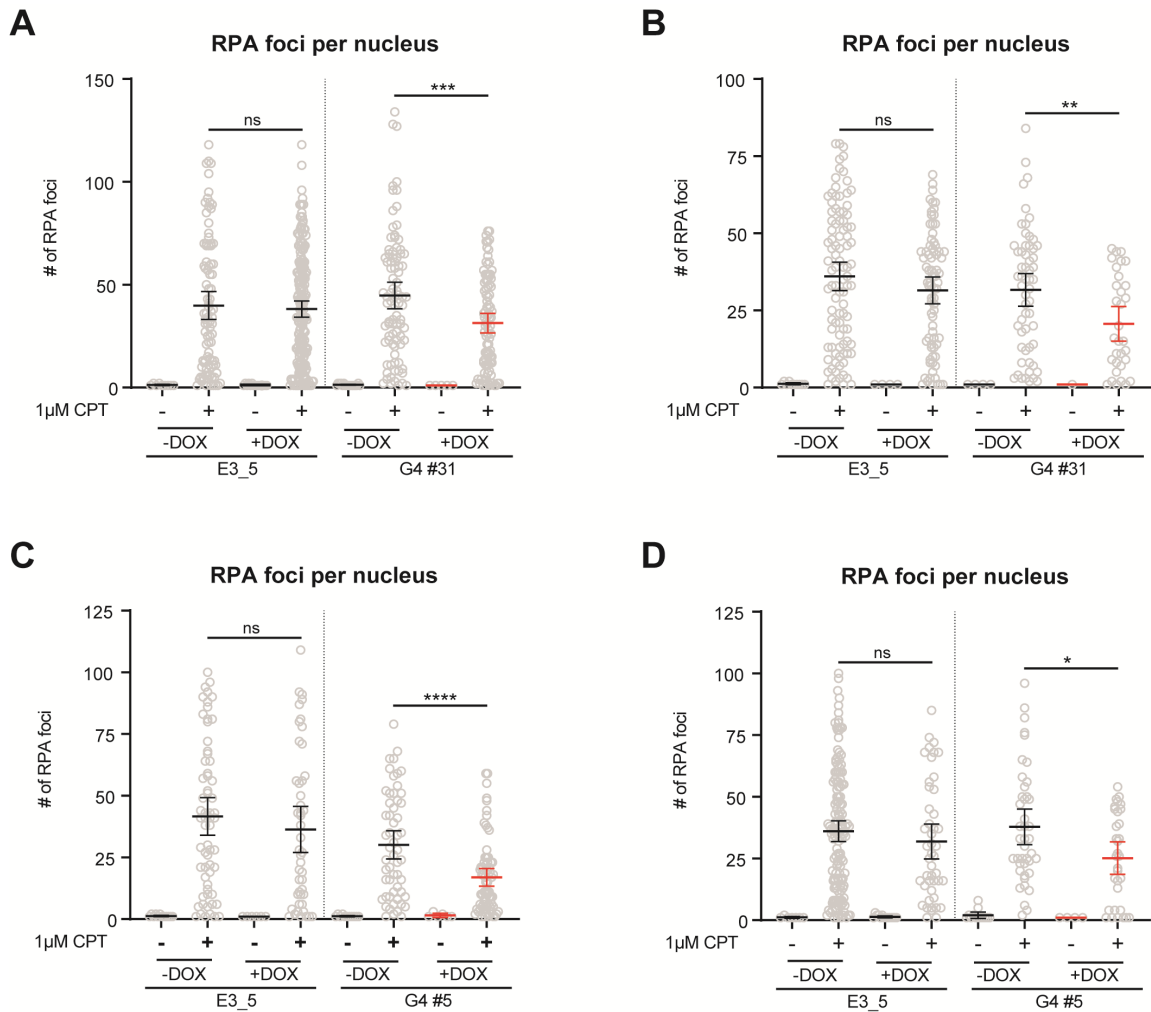


Figure S7: Replicates of figure 11: 2-RING and SPOP system for degradation of Myo6

The constructs (2-RING, SPOP) were brought into A549 WT cells using lentiviral transduction. For each cell line, a control DARPin (E3_5) and a Myo6 binding DARPin (G4) was transfected. Previously tested clones were pre-treated with - / + 16 h 2 μ g/ml DOX and treated next with - / + 1 μ M CPT for 1 h. After treatment of 1h, cells were pre-extracted, fixed and stained with RPA specific antibodies. Dot plots show number of RPA foci per nucleus with mean values \pm 95% confidence intervals. Significance levels were calculated using the students t-test from at least 100 nuclei per sample (ns: non-significant, ****: $p < 0.0001$, ***: $p < 0.001$, *: $p < 0.05$). Two independent replicates are shown.

(A/B) 2-RING G4 clone #31 shows upon DOX, a significant decrease in RPA foci number per nucleus. (C/D) SPOP G4 clone #5 shows upon DOX, a significant decrease in RPA foci number per nucleus.

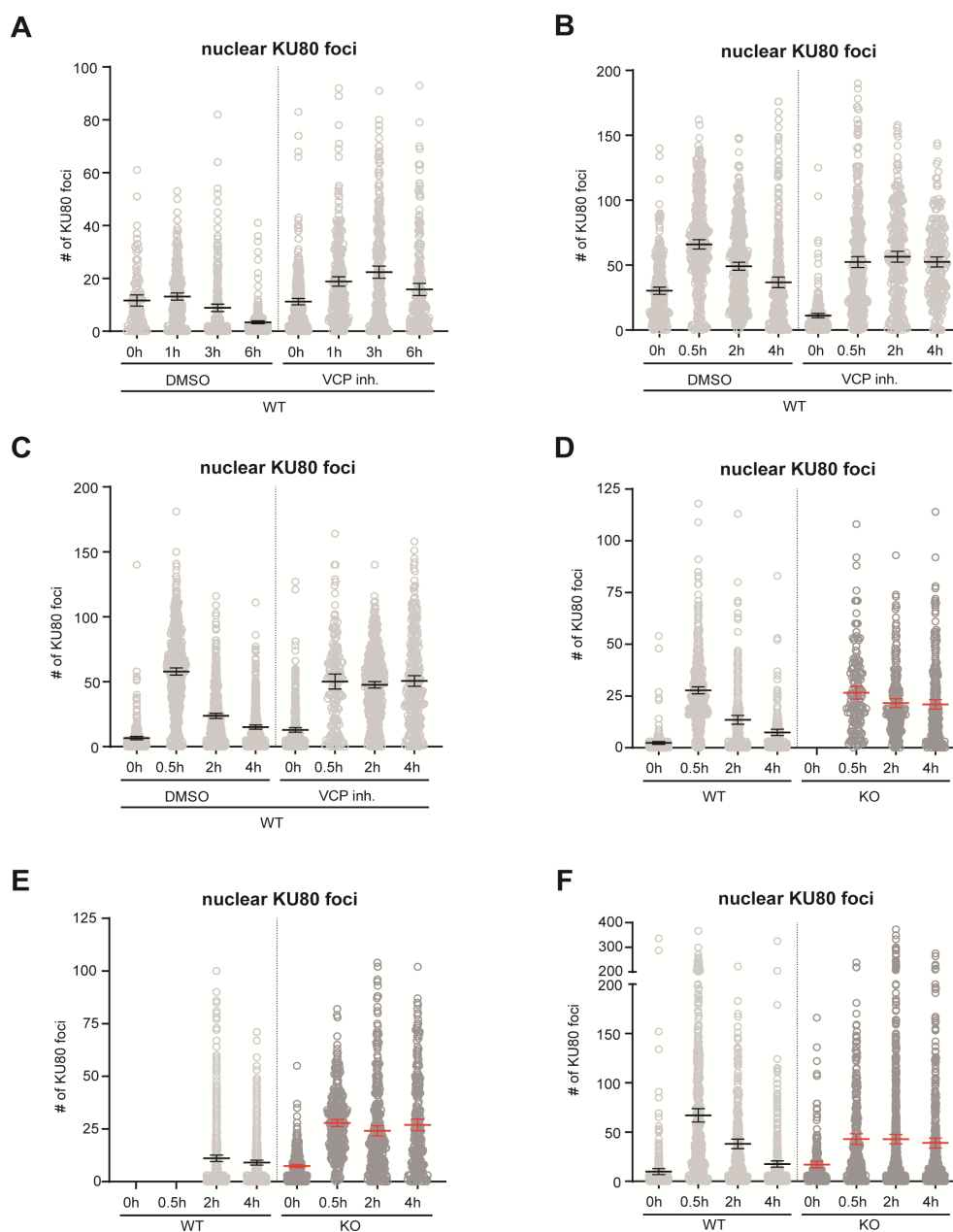


Figure S8: Replicates of figure 14: Myo6 in KU70/80 removal

(A-D) A549 WT cells show no KU80 foci resolution up to 4 h after IR damage upon VCP inhibition. A549 WT cells were 15 minutes pre-treated with 0.1 % DMSO or 5 μ M VCP inhibitor (inh) (NMS-873). All cell lines were then irradiated with 10 Gy IR and then released into fresh medium with / without DMSO or VCP inh for indicated timepoints. When all timepoints were collected, cells were pre-extracted, fixed and stained with KU80 specific antibodies and Hoechst. Dot plot show KU80 foci per nucleus with mean values \pm 95% confidence intervals. Significance levels were calculated using the students t-test from at least 100 nuclei per sample (ns: non-significant, ****: $p < 0.0001$, ***: $p < 0.001$, *: $p < 0.05$). Three independent replicates are shown.

(D-F) A549 KO cells show no KU80 foci resolution up to 4 h after IR damage. A549 WT and KO cells were treated with 10 Gy IR and then released into fresh medium for indicated timepoints. The staining and evaluation were performed as in (A-D). Three independent replicates are shown.

Nuclear myosin VI maintains replication fork stability

Received: 19 September 2022

Accepted: 9 June 2023

Published online: 24 June 2023

 Check for updates

Jie Shi¹, Kristine Hauschulte ¹, Ivan Mikicic ¹, Srijana Maharjan^{1,4}, Valerie Arz¹, Tina Strauch¹, Jan B. Heidelberger^{1,5}, Jonas V. Schaefer ², Birgit Dreier², Andreas Plückthun ², Petra Beli ^{1,3}, Helle D. Ulrich ¹ ✉ & Hans-Peter Wollscheid ¹ ✉

The actin cytoskeleton is of fundamental importance for cellular structure and plasticity. However, abundance and function of filamentous actin in the nucleus are still controversial. Here we show that the actin-based molecular motor myosin VI contributes to the stabilization of stalled or reversed replication forks. In response to DNA replication stress, myosin VI associates with stalled replication intermediates and cooperates with the AAA ATPase Werner helicase interacting protein 1 (WRNIP1) in protecting these structures from DNA2-mediated nucleolytic attack. Using functionalized affinity probes to manipulate myosin VI levels in a compartment-specific manner, we provide evidence for the direct involvement of myosin VI in the nucleus and against a contribution of the abundant cytoplasmic pool during the replication stress response.

Complete and correct duplication of the genome in each cell cycle is crucial for genome stability in proliferating cells. One of the many protective responses to DNA replication stress is the reversal of replication forks, involving a reannealing of the parental strands and a joining of the newly synthesized strands into a four-way Holliday junction-like structure^{1,2}. However, fork reversal, mediated by DNA-remodeling factors such as RAD51, SMARCAL1, HLTF, and ZRANB3^{3–5}, can also be detrimental for genome stability. Due to their structure resembling a one-ended double strand break (DSB), reversed forks can become targets of nucleolytic attack by nucleases such as DNA2 and MRE11, resulting in fork instability and collapse⁶.

The actin cytoskeleton exerts a fundamental role in cell mechanics, motility and intracellular transport. Filamentous (F-) actin is highly abundant in the cytoplasm but barely detectable in the nucleus, where its functional relevance is still controversially discussed^{7,8}. Recent discoveries have connected nuclear F-actin to genome maintenance pathways such as DSB repair, DNA replication and maintenance of nuclear architecture^{9–14}. If and how myosins in their function as actin-based molecular motor proteins participate in these processes is still poorly understood. The myosin superfamily

comprises more than 35 distinct classes, of which only a few have been shown to exert nuclear functions in humans¹⁵. Based on their presumably higher degree of functional specialization compared to actin, investigation of myosins rather than actin itself provides a unique opportunity to tease apart specific functional aspects of actin-mediated dynamic processes while avoiding the pleiotropic effects of manipulating actin directly.

Myosin VI, the only minus end-directed myosin characterized to date¹⁶, is well known for its contribution to multiple steps of the transcriptional process^{17–19}. Here we report an association of myosin VI with numerous components of the replication machinery. Upon replication stress, we found myosin VI to cooperate with Werner helicase interacting protein 1 (WRNIP1) in the protection of stressed replication forks from DNA2-mediated degradation.

Results

Myosin VI interacts with replisome components and protects reversed forks from nuclease-mediated degradation

We recently identified a region adjacent to the C-terminal cargo-binding domain of myosin VI as a ubiquitin-interacting domain

¹Institute of Molecular Biology gGmbH (IMB), Ackermannweg 4, D – 55128 Mainz, Germany. ²University of Zurich, Department of Biochemistry, Winterthurerstr. 190, CH – 8057 Zurich, Switzerland. ³Institute of Developmental Biology and Neurobiology, Johannes Gutenberg University, Hanns-Dieter-Hüsch-Weg 15, D – 55128 Mainz, Germany. ⁴Present address: Mainz Biomed N.V., Robert-Koch-Str. 50, D – 55129 Mainz, Germany. ⁵Present address: Max Planck School Matter to Life, Jahnstr. 29, D – 69120 Heidelberg, Germany. ✉ e-mail: h.ulrich@imb-mainz.de; h.wollscheid@imb-mainz.de

(MyUb, Fig. 1a)²⁰. Pull-down assays with a GST-MyUb construct, followed by SILAC-based quantitative mass spectrometry (Fig. 1b), identified 490 proteins with an at least twofold enrichment over the GST control (FDR < 0.05; Supplementary Data 1, Supplementary Fig. 1b), including 346 proteins annotated with the gene ontology (GO) cellular

compartment “nucleus” (Supplementary Data 2). In line with its known function, GO term analysis of the MyUb interactome showed transcription-associated proteins as the most prominently enriched category (Fig. 1c, Supplementary Data 3). We also detected GIPC1, a well-described cytoplasmic myosin VI cargo (Fig. 1d). In addition, we

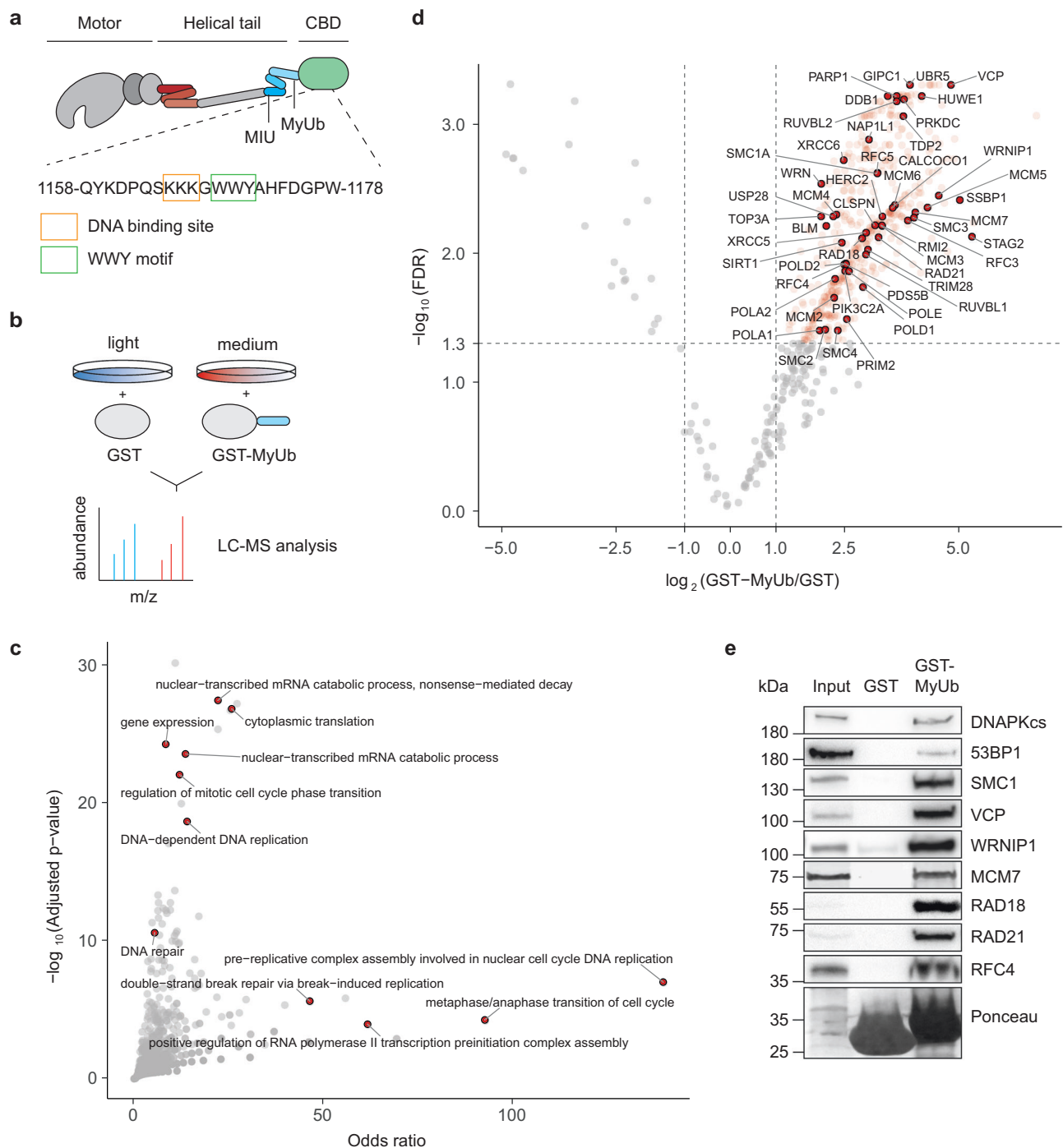


Fig. 1 | Myosin VI interacts with the replisome. **a** Schematic representation of myosin VI (adapted from Magistrati and Polo⁴⁰) showing the positions of the ubiquitin-binding MIU and MyUb domains (blue) adjacent to the cargo-binding domain (CBD, green). The amino acid sequence shows a triple-Lys repeat involved in DNA binding¹⁸ (orange box) and the WWY motif (green box), a well-characterized protein interaction site. The three-helix bundle at the N-terminal tail is indicated in red. Amino acid numbering is according to the short isoform (isoform 2). **b** Set-up of the SILAC experiment for identification of MyUb interaction partners. **c** GO term analysis (GO biological process) of proteins identified to interact with the MyUb

domain (fold change > 4, FDR < 0.05) using EnrichR. **d** Volcano plot of protein groups identified in the SILAC interactome experiment. Mean \log_2 fold change of all replicates between GST-MyUb and GST are plotted against the $-\log_{10}$ FDR. Significantly enriched proteins are shown in red (fold change > 2, FDR < 0.05). Interactors involved in DNA replication and repair are highlighted and labeled. **e** Validation of selected candidates by pull-down assays from total cell lysates with recombinant GST-MyUb, followed by western blotting and Ponceau S staining. Results were confirmed by at least two independent experiments. Source data are provided as a Source Data file.

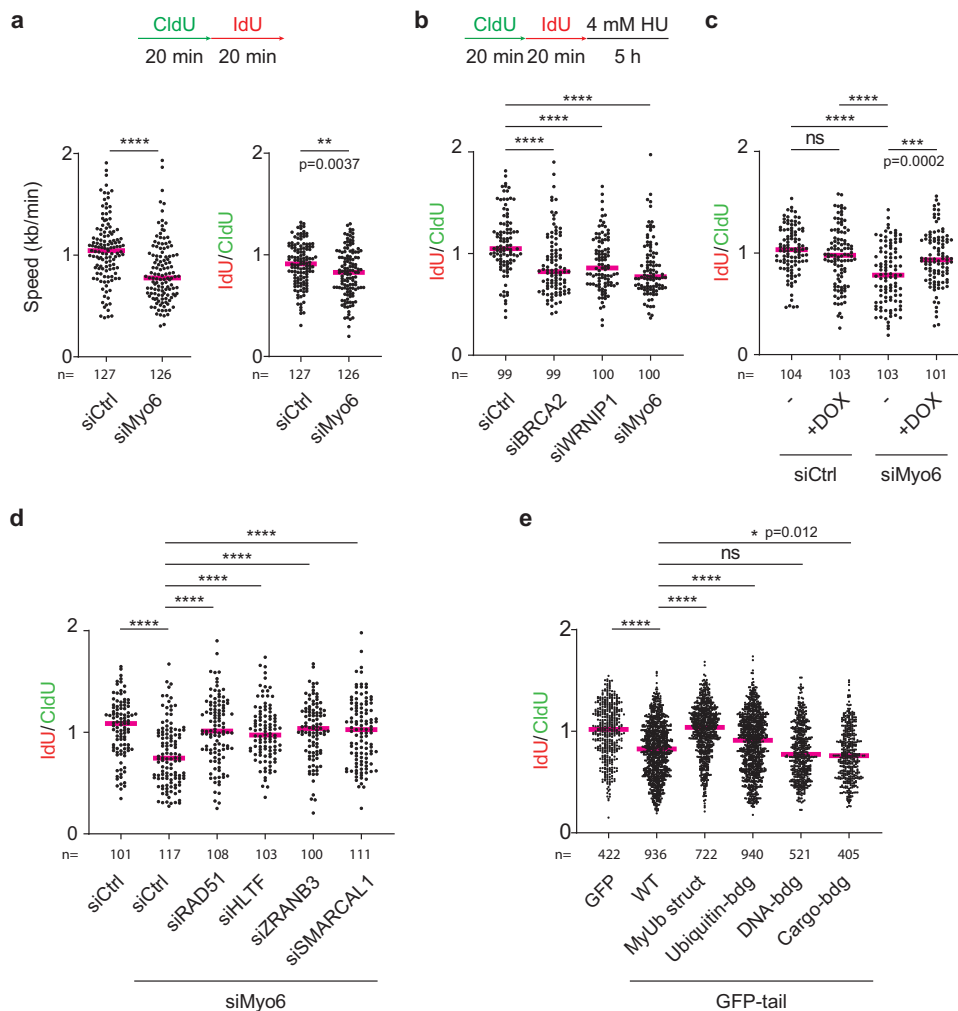


Fig. 2 | Myosin VI protects stalled replication forks from degradation. **a** Myosin VI is required for efficient unperturbed DNA replication. Top: Schematic representation of fiber assay conditions. Bottom: Fiber assays performed on siRNA-transfected U2OS cells. Left panel: replication speed, measured as total track lengths (CldU+IdU). Right panel: IdU/CldU ratio. **b** Depletion of myosin VI via siRNA causes erosion of stalled replication forks. Top: Schematic representation of fiber assay conditions. Bottom: Fiber assays performed on siRNA-transfected U2OS cells. **c** GFP-myosin VI complements the loss of endogenous myosin VI. U2OS cells harboring DOX-inducible GFP-myosin VI were siRNA-transfected (siRNA #10 targeting myosin VI) and treated $-/+$ 20 ng/ml DOX for 24 h, followed by fiber assays as shown in **(b)**. **d** Myosin VI-dependent fork protection requires fork reversal factors. U2OS cells were siRNA-transfected as indicated, followed by fiber assays as shown

in **(b)**. **e** Motor- and MyUb-domains of myosin VI are required for fork protection. GFP-tail *wildtype* (WT) and mutants were overexpressed in U2OS cells, followed by fiber assays as shown in **(b)**. Combined data from at least three independent replicates are shown. Detailed information about the respective mutations is given in Supplementary Fig. 2f. For all panels: IdU/CldU ratios are shown as dot plots with median values (red bars). Significance levels were calculated using the two-sided Mann–Whitney test from the indicated number of fibers per sample (ns: not significant, ****: $p < 0.0001$, ***: $p < 0.001$, **: $p < 0.01$, *: $p < 0.05$) and annotated for $p > 0.0001$. Knockdown efficiencies and overexpression levels are shown in Supplementary Fig. 2. For **(a–d)**: A representative experiment from three independent replicates is shown. Source data are provided as a Source Data file.

identified many DNA replication-associated factors, suggesting a yet unidentified function of myosin VI at the replisome (Fig. 1c, d). Immunoprecipitation (IP) experiments upon overexpression of GFP-tagged putative interactors (Supplementary Fig. 1c) or pull-down experiments with recombinant GST-MyUb followed by immunoblotting with antibodies against endogenous proteins (Fig. 1e) validated many of the candidates identified in our proteomic screen as genuine interaction partners of myosin VI.

To assess a potential role of myosin VI during DNA replication, we measured replication speed using DNA fiber assays, where nascent DNA is labeled consecutively with two thymidine analogues, CldU and IdU. Knockdown of myosin VI did not lead to detectable changes in the activation pattern of the checkpoint kinase ATR in the absence or presence of replication stress (Supplementary Fig. 2b) but caused a reduction in overall unperturbed DNA replication speed, suggesting its requirement for efficient DNA replication (Fig. 2a, left panel). To

determine whether this reduction was attributable to an overall slowing of replication fork progression or rather an increase in the frequency of fork breakdown, we calculated the IdU/CldU ratio as an estimate of the extent to which forks irreversibly stall during the IdU pulse. A reduction of this value upon myosin VI knockdown suggested an increased propensity of fork stalling or possibly a defect in fork recovery after stalling (Fig. 2a, right panel).

The AAA-ATPase WRNIP1 has been implicated in genome maintenance as a protector of reversed replication forks^{21,22}. Considering its identification as an interaction partner of myosin VI (Fig. 1d, e, Supplementary Fig. 1c), we asked whether the replication problems upon myosin VI depletion were linked to a defect in the protection of stalled forks. To distinguish fork degradation from fork stalling, we labeled cells with CldU and IdU for 20 min each, followed by a 5 h treatment with hydroxyurea (HU) (Fig. 2b). In this setup, any additional shortening of the IdU tract is an indication of nascent strand degradation

during the HU treatment. According to their well-established roles as replication fork protectors, siRNA-mediated depletion of WRNIP1 and BRCA2²³ resulted in a reduction in the IdU/CldU ratio (Fig. 2b). Notably, myosin VI depletion reduced this ratio to a similar extent, suggesting that myosin VI is essential for preventing nuclease-mediated degradation of reversed forks (Fig. 2b). To exclude off-target effects, we carried out rescue experiments using a cell line expressing siRNA-resistant GFP-myosin VI under the control of a doxycycline (DOX)-inducible promoter (Fig. 2c, Supplementary Fig. 2d). In control cells expressing endogenous myosin VI, addition of DOX did not significantly alter the stability of stalled replication forks (Fig. 2c, lanes 1 and 2). However, in myosin VI-depleted cells, we observed a rescue of fork protection upon DOX-induced restoration of myosin VI levels (Fig. 2c, lanes 3 and 4), thus verifying the direct correlation between replication fork stability and myosin VI abundance. Furthermore, co-depletion of the fork remodelers RADS1, HLTF, SMARCAL1 or ZRANB3 together with myosin VI completely abolished nascent strand degradation (Fig. 2d), indicating that the defect in fork stability induced by myosin VI depletion depends on the prior action of the fork remodelers. Thus, myosin VI appears to protect reversed replication forks, but it does not prevent fork reversal.

To elucidate the molecular characteristics of myosin VI-dependent fork protection, we made use of a motor-deficient variant (GFP-tail, Supplementary Fig. 2f). Its overexpression resulted in nascent strand degradation similar to myosin VI depletion (Fig. 2e), demonstrating the importance of its motor activity for fork protection. By exploiting this dominant-negative effect, we addressed the contributions of multiple functional domains of myosin VI (Supplementary Fig. 2f, g) to the replication stress response. It was previously shown that mutation of the RRL motif within the MyUb domain leads to destabilization of its helical structure²⁰. In line with the multitude of replication factors that interact with this domain, mutation of the RRL motif to AAA abolished the dominant-negative effect of the GFP-tail construct (Fig. 2e, lane 3). A combination of point mutations in the MIU (A1013G)²⁴ and MyUb (I1072A)²⁰ domains revealed a contribution of ubiquitin binding to myosin VI's activity in fork protection, whereas its DNA¹⁸- and WWY²⁵-mediated cargo-binding activities (Fig. 1a, Supplementary Fig. 2f) seem to be less important (Fig. 2e).

Myosin VI cooperates with WRNIP1 to protect stalled forks from DNA2-mediated degradation

In contrast to other fork protectors, myosin VI primarily localizes to the cytoplasm. Even upon replication stress, where nuclear actin and F-actin levels slightly increase, we did not observe an accumulation of myosin VI in the nucleus (Supplementary Fig. 3a–f). To investigate a potential physical association with ongoing and stalled or reversed replication forks, we therefore utilized iPOND (isolation of proteins on nascent DNA) with western blotting to focus specifically on chromatin-associated factors²⁶. PCNA is known to dissociate from newly replicated DNA upon replication stress²⁷, and this pattern was reproducible in our hands (Fig. 3a). In agreement with the observed interactions of myosin VI with replisome components (Fig. 1c, e), we detected myosin VI at unperturbed replication forks (Fig. 3a). Unlike PCNA, however, myosin VI association was not diminished upon HU treatment. To achieve a more quantitative assessment, we used SIRF (in situ protein interaction with nascent DNA replication forks) assays, which detect the co-localization of a protein of interest with nascent, EdU-labeled DNA via proximity ligation²⁸. Again, the PCNA signal was lost under conditions of replication stress, while both myosin VI and WRNIP1 showed enhanced association with EdU-positive nascent DNA upon HU treatment (Fig. 3b), suggesting an enrichment of both myosin VI and WRNIP1 at stalled forks.

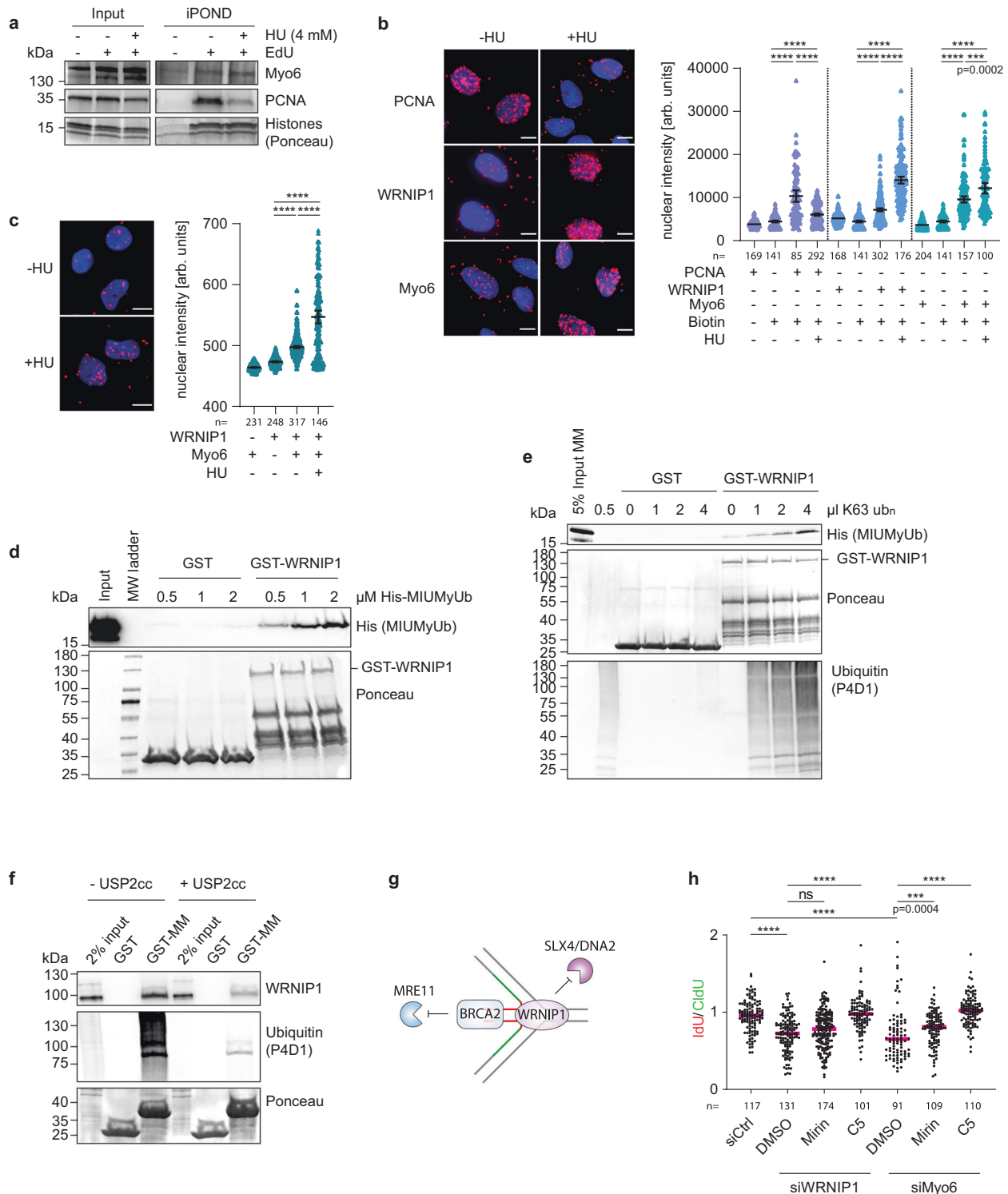
Having established the interaction of WRNIP1 with the MyUb domain of myosin VI (Fig. 1e, Supplementary Fig. 1c), we utilized proximity ligation assays (PLA) to validate this interaction in living cells

using antibodies against the endogenous proteins (Fig. 3c). Strikingly, the PLA signal was prominently enhanced under conditions of replication stress, suggesting that the proteins preferentially interact at stalled replication forks (Fig. 3c). To assess whether the interaction of WRNIP1 with myosin VI is direct or possibly mediated via common association on ubiquitin conjugates through their respective ubiquitin-binding domains^{20,29}, we performed GST-pulldown assays with bacterially expressed recombinant proteins. We detected a direct interaction of a His-tagged MIUMyUb domain construct with GST-WRNIP1 (Fig. 3d) that was further enhanced by the addition of K63-linked polyubiquitin chains (Fig. 3e), indicating a potential modulation of the myosin VI-WRNIP1 interaction by ubiquitin signaling. To verify this effect with endogenous proteins, we pre-treated cellular lysates with a non-selective de-ubiquitylating enzyme, His-USP2cc³⁰, resulting in the disassembly of endogenous ubiquitin conjugates. A significant decrease in WRNIP1 binding to myosin VI was detected upon His-USP2cc treatment, further supporting the relevance of polyubiquitin chains for myosin VI's association with WRNIP1 (Fig. 3f).

Unlike BRCA2, which is thought to protect the ends of the regressed arm from MRE11-dependent degradation²³, WRNIP1 was reported to prevent attack by SLX4/DNA2 at the four-way junction²¹ (Fig. 3g). To specify the nature of myosin VI activity at reversed forks, we performed DNA fiber assays in the presence of the MRE11- or DNA2-specific inhibitors mirin or C5, respectively. Consistent with previous findings²¹, mirin treatment did not rescue nascent strand degradation in WRNIP1-depleted cells, while DNA2 inhibition led to a full stabilization of reversed forks (Fig. 3h). Use of the inhibitors in myosin VI-depleted cells resulted in a very similar pattern (Fig. 3h), suggesting that myosin VI cooperates with WRNIP1 to protect reversed replication forks from DNA2-mediated nucleolytic attack.

A functionalized DARPIn verifies the contribution of myosin VI to fork stabilization

Actin filaments are of a transient nature and difficult to detect in the nucleus because of their high cytoplasmic abundance. An actin-specific nanobody fused to a nuclear localization signal (NLS), termed nuclear actin chromobody (nAC), has proven to be a valuable instrument in visualizing nuclear F-actin specifically³¹. However, manipulation of nuclear F-actin remains challenging due to the involvement of monomeric actin in chromatin remodeling complexes³² and its association with RNA polymerase complexes^{33–35}. Inspired by the nAC technology, we aimed to develop tools to manipulate the stability and localization of endogenous myosin VI. To obtain a myosin VI-specific affinity probe, we employed a ribosome display library of designed ankyrin repeat proteins (DARPins)³⁶, which consist of stacked repeat modules with a randomized surface. They can be selected to bind proteins with antibody-like selectivity and affinity^{36–38}. Unlike antibodies, DARPins fold under the reducing conditions of the cytoplasm and the nucleus and can thus be expressed and folded in these compartments. After selection of DARPins using a biotinylated tail fragment of myosin VI (aa 992 – 1122) as bait, the enriched pool was subcloned into an *E. coli* expression vector and crude bacterial extracts of 380 individual clones were tested for DARPIn binding to the biotinylated fragment of myosin VI in HTRF assays (Supplementary Fig. 4a). Among these, 54 high-scoring clones (>30% signal over background) and 46 clones with low signal intensity (>5%) were identified as initial hits. From these, 52 random clones were chosen and further screened in GST-pulldown experiments (examples are shown in Supplementary Fig. 4b). Five positive clones were tested for their ability to deplete endogenous myosin VI from cellular lysates, using a non-binding DARPIn (E3_5)³⁸ as negative control. One clone, M6G4, effectively depleted myosin VI from the lysate (Fig. 4a, Supplementary Fig. 4d, Supplementary Fig. 7) and was therefore selected as the target-binding module for the myosin VI-specific tools. Using Surface Plasmon Resonance (SPR) assays, we measured a dissociation constant for



M6G4 of ca. 60 nM (Supplementary Fig. 4e). Notably, M6G4 does not interfere with the binding of endogenous interactors like WRNIP1 or ubiquitin to myosin VI (Supplementary Fig. 4f).

To generate a myosin VI-specific degradation tool, we adapted a recently published system based on the ubiquitin protein ligase RNF4³⁹ (Supplementary Fig. 5a). A fusion construct of DARPin M6G4 with two RING finger domains of RNF4 (M6G4-2RING) was stably integrated in the chromosomes under the control of a DOX-inducible promoter. A single-cell clone termed 2R#8 showed efficient proteasome-dependent degradation of endogenous myosin VI in a time- and DOX-dependent manner (Fig. 4b, Supplementary Fig. 5b–d).

Importantly, depletion of myosin VI via M6G4-2RING resulted in a destabilization of stalled forks, comparable to siRNA-mediated myosin VI depletion (Fig. 4c), providing additional support for the specificity of the phenotype.

The nuclear but not the cytoplasmic pool of myosin VI contributes to fork protection

Having verified the selectivity of the M6G4 probe, we asked whether fork stability was regulated by the nuclear or the cytoplasmic pool of myosin VI. We found that inducible expression of a GFP-tagged fusion construct of M6G4 to a 3xNLS resulted in a nearly complete

Fig. 3 | Myosin VI cooperates with WRNIP1 to protect stalled forks from DNA2-mediated degradation. **a** iPOND assays show localization of myosin VI at replication forks. U2OS cells, 30 min EdU-pulsed \pm 4 mM HU. Chromatin-bound proteins are visualized using western blotting and Ponceau S staining. **b** SIRF assays confirm the presence of myosin VI at replication forks. U2OS cells, 30 min EdU-pulsed \pm 4 mM HU, followed by click reaction with Biotin azide and standard PLA assay. **c** Interaction of myosin VI with WRNIP1 is enhanced upon replication stress. U2OS cells, \pm 4 mM HU, followed by standard PLA assay. For **(b, c)**: Left: representative images, Hoechst (blue), PLA (magenta), scale bar = 10 μ m. Right: dot plots of PLA signal intensities with mean values \pm 95% confidence intervals. **d** WRNIP1 interacts directly with the MIUMyUb domains of myosin VI. GST-pulldown assay with recombinant proteins, visualized by western blotting and Ponceau S staining. Input represents 5% of the 2 μ M MIUMyUb sample. **e** K63-linked ubiquitin chains enhance the WRNIP1-myosin VI interaction. GST-pulldown as in **(d)**, using 1 μ M His-MIUMyUb and increasing concentrations of K63 poly-ubiquitin. **f** Depletion of

ubiquitin conjugates interferes with the WRNIP1-myosin VI interaction. GST-pulldown assay with recombinant baits and cellular lysates, pre-treated for 10 min at 37 $^{\circ}$ C \pm 5 μ M USP2c. Visualization by western blotting and Ponceau S staining. **g** Schematic representation of fork protection mechanisms by WRNIP1 and BRCA2 according to Porebski et al.²¹ with nascent DNA colored in green and red. **h** Inhibition of DNA2 restores fork stability in WRNIP1- and myosin VI-deficient cells. Fiber assays performed on siRNA-transfected U2OS cells, \pm 5 h nuclease inhibitor treatment, as in Fig. 2b. IdU/CldU ratios are shown as dot plots with median values. Knockdown efficiencies are shown in Supplementary Fig. 3g. For **(a-f, h)**: A representative experiment from three independent replicates is shown. For **(b, c, h)**: Significance levels were calculated using the two-tailed Mann-Whitney test from the indicated number of nuclei or fibers per sample (ns: not significant, ****: $p < 0.0001$, ***: $p < 0.001$) and annotated for $p > 0.0001$. Source data are provided as a Source Data file.

localization of myosin VI to the nuclear compartment (Fig. 4d), while the analogous GFP-NLS-E3_5 control construct (with a non-binding DARPin) did not afford significant changes in the subcellular distribution of myosin VI. Fiber assays in cells expressing either the myosin VI-specific or the control NLS-DARPin did not show significant degradation of newly replicated DNA (Fig. 4e), suggesting that depletion of cytoplasmic myosin VI has little or no influence on fork stability. Unfortunately, our attempts to selectively deplete myosin VI from the nucleus by fusion of an analogous nuclear export signal (NES) were inconclusive due to low expression of the NES-M6G4 construct and difficulties visualizing the nuclear pool of myosin VI.

As an alternative approach, we therefore expressed motor-deficient myosin VI mutants (NLS/NES-tail) intended as dominant-negative alleles that would compete with endogenous myosin VI for functional interactions in the respective subcellular compartments. Whereas expression of nuclear NLS-tail caused significant degradation of nascent DNA, expression of cytoplasmic NES-tail had no effect (Fig. 4f, Supplementary Fig. 5g), strongly suggesting that the compartment relevant for myosin VI activity in fork protection is the nucleus rather than the cytoplasm.

Myosin VI promotes replication stress-induced WRNIP1 accumulation at replication forks

The requirement of myosin VI's motor domain for its function in fork protection implied a mobility-dependent mechanism (Fig. 2e). This might involve an active transport of fork-protecting factors such as WRNIP1 toward stalled or reversed forks (Fig. 5a) or, alternatively, a transport of fork-stabilizing factors such as pertinent nucleases away from the sites of fork stalling (Fig. 5b). To differentiate between these models, we used SIRF to test whether myosin VI affected the recruitment of WRNIP1 to unperturbed or stalled replication forks. Consistent with our previous results (Fig. 3b), control cells expressing myosin VI afforded a WRNIP1 signal at unperturbed forks that increased after HU treatment (Fig. 5c). Knockdown of myosin VI did not significantly affect association of PCNA with replication forks (Fig. 5c, left panel) and WRNIP1 recruitment to unperturbed replication forks. However, under conditions of replication stress, we scored a clear defect in WRNIP1 accumulation at forks upon depletion of myosin VI, arguing for a model where myosin VI positively regulates WRNIP1's enhanced association with stressed replication forks (Fig. 5a). Conversely, WRNIP1 depletion did not affect localization of myosin VI to replication forks (Supplementary Fig. 6). In summary, these data show the requirement of myosin VI for efficient WRNIP1 localization to stalled replication forks.

Discussion

Our findings connect the actin-based motor protein myosin VI to a defined pathway of replication fork protection that maintains genome stability under conditions of replication stress. Using an unbiased mass

spectrometry approach in combination with in situ localization studies, we found myosin VI to accumulate at stalled replication forks in response to nucleotide depletion, and functional assays have revealed a contribution to the WRNIP1-mediated protection of stressed forks from nucleolytic attack by DNA2. Based on our placement of myosin VI activity downstream of a series of factors known to mediate fork reversal, such as RAD51, SMARCAL1, HLTf and ZRANB3³⁻⁵, we postulate that myosin VI specifically acts on reversed forks; however, our data do not exclude an alternative fork geometry generated by the above mentioned remodelers. The notion that the motor domain of myosin VI is required for its function suggests a role in shuttling; however, as myosin VI has also been shown to act in an anchoring fashion⁴⁰, we cannot exclude a model where myosin VI stabilizes the fork protection complex at the junction between parental and reversed strands in a static manner. In addition to the motor domain, we found the UBDs of myosin VI to be functionally important (Fig. 2e). The identification of another ubiquitin-binding protein, WRNIP1, as a direct interactor of myosin VI and the stimulating effect of ubiquitin chains on this interaction strongly suggest a regulatory role of ubiquitin signaling in this particular pathway of replication fork protection (Fig. 3d-f). Although ubiquitin is known as a signaling molecule in virtually all cellular processes, its contributions to the replication stress response are still poorly understood. In contrast, DNA binding by myosin VI does not appear to be important in this context, as the relevant mutant did not cause any fork destabilization.

Beyond the functional interaction of myosin VI and WRNIP1, our data support and expand recent evidence for nuclear functions of the actin cytoskeleton in genome maintenance. Although we did not directly address nuclear F-actin, the requirement of the myosin VI motor domain for fork protection (Figs. 2e, 4f) strongly suggests a mechanism based on the interaction of the myosin with nuclear actin filaments rather than invoking an actin-independent mechanism. However, WASp, a positive regulator of ARP2/3 dependent actin-polymerization, was recently shown to modulate RPA-regulated signaling upon genotoxic insult⁴¹. The authors convincingly demonstrate an actin-independent role of WASp as a chaperone-like factor for RPA's ssDNA binding. Likewise, we cannot rule out additional, actin-independent functions of myosin VI.

Finally, while technical limitations have so far precluded firm evidence against an influence of the cytoplasmic actin cytoskeleton on genome maintenance, our newly designed tools in combination with classical dominant-negative approaches have provided clear evidence for the relevance of the nuclear pool of myosin VI for fork protection while excluding myosin VI-related cytoplasmic signaling events.

The formation of actin filaments inside the nucleus upon replication stress, detected by Lamm et al.¹⁴, raises speculations about the relevance of the unique minus-end directionality of myosin VI and the possible orientation of actin filaments forming in the vicinity of

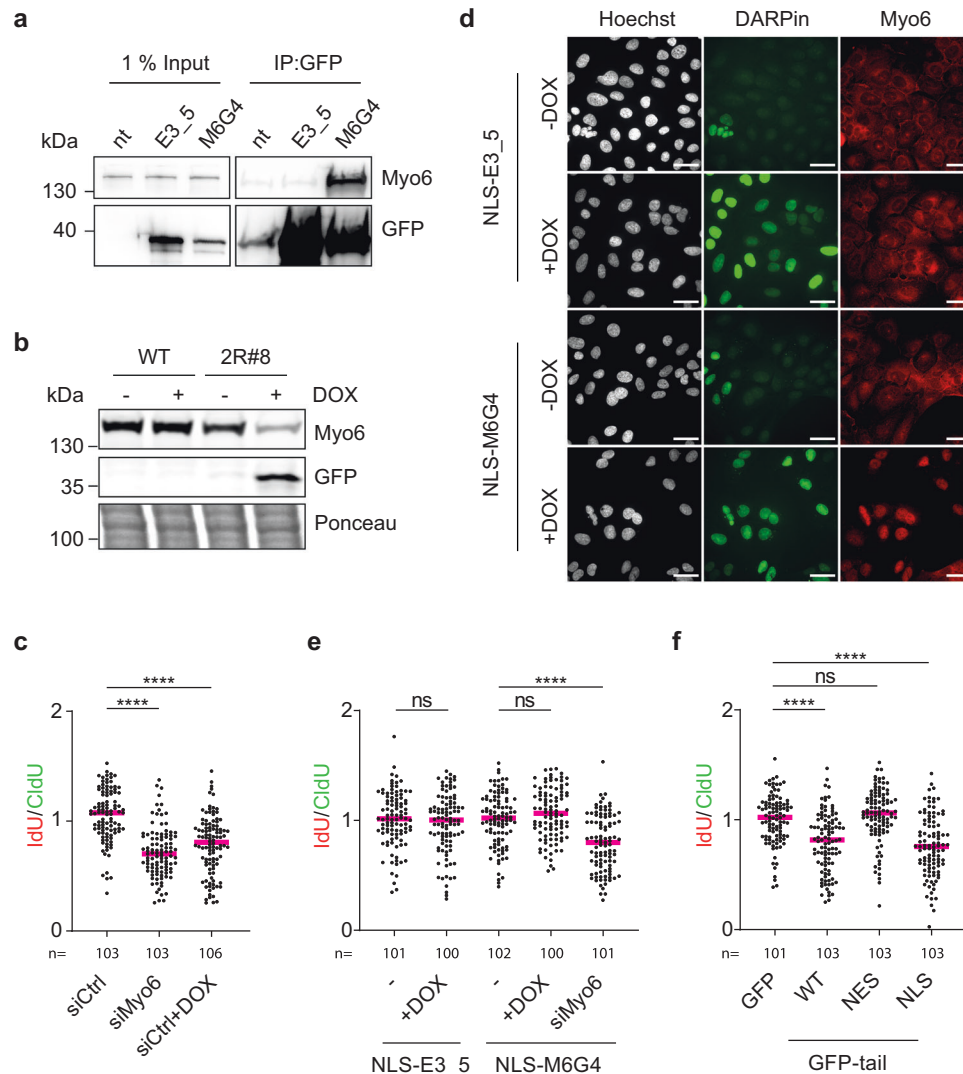


Fig. 4 | Nuclear but not cytoplasmic myosin VI is active in fork protection.
a DARPin M6G4 depletes myosin VI from cellular lysates. HEK293T cells, transfected with control (GFP-E3_5) or anti-myosin VI DARPin (GFP-M6G4), subjected to immunoprecipitations (IPs) against GFP, followed by western blotting. **b** DOX-induced degradation of myosin VI via a DARPin-based construct. A U2OS Flp-In T-REx single-cell clone harboring a DOX-inducible GFP-M6G4-2RING fusion construct (2R#8) was treated $-/+$ 20 ng/ml DOX for 24 h. Cellular lysates were analyzed by western blotting and Ponceau S staining. **c** DARPin-2RING fusion-mediated degradation of myosin VI interferes with fork protection. U2OS Flp-In T-REx cells harboring DOX-inducible GFP-M6G4-2RING (2R#8) were siRNA-transfected and treated $-/+$ 20 ng/ml DOX for 24 h, followed by fiber assays as shown in Fig. 2b. **d** DARPin-mediated re-localization of myosin VI to the nucleus. U2OS Flp-In T-REx cells harboring DOX-inducible GFP-M6G4-NLS or GFP-E3_5-NLS (control), treated $-/+$ 20 ng/ml DOX for 24 h, were analyzed by immunofluorescence (IF) using

myosin VI-specific antibodies (red) and Hoechst (white). GFP-DARPin: green; scale bar = 40 μ m. **e** Depletion of cytoplasmic myosin VI has no effect on fork stability. U2OS Flp-In T-REx cells harboring DOX-inducible GFP-M6G4-NLS or GFP-E3_5-NLS (control) were siRNA-transfected (siRNA#10 targeting myosin VI) and treated $-/+$ 20 ng/ml DOX for 24 h, followed by fiber assays as shown in Fig. 2b. **f** Inhibition of nuclear but not cytoplasmic myosin VI leads to fork de-stabilization upon replication stress. Fiber assays as shown in Fig. 2b, performed on U2OS cells transfected with compartment-specific GFP-tail constructs. For (c, e, f): IdU/CldU ratios are shown as dot plots with median values. Significance levels were calculated from the indicated number of fibers per sample using the two-tailed Mann-Whitney test (ns: not significant, ****: $p < 0.0001$). A representative experiment from three independent replicates is shown. Knockdown efficiencies and overexpression levels are shown in Supplementary Fig. 5. For (a, b, d): Results were confirmed by at least two independent experiments. Source data are provided as a Source Data file.

reversed forks. We also envision the involvement of other myosins, e.g., myosin I or myosin V¹⁰, in fork protection, opening the possibility for a competition between minus- and plus-end-directed motors. Probing the role of other myosins as well as actin cytoskeleton proteins such as bundling, capping, assembly or disassembly factors will thus be important for future studies. Taken together, our discovery of the requirement of myosin VI-dependent transport or tethering for the protection of stressed replication forks, possibly controlled by ubiquitin binding, adds to the accumulating evidence for a key role of the nuclear actin cytoskeleton in genome maintenance and paves the way for exploring new layers of regulation of nuclear transactions by a set of proteins better known for their role in cytoplasmic signaling.

Methods

Cell lines, cultivation and treatments

U2OS, HeLa and HEK293T cells were maintained in DMEM containing 10% fetal bovine serum, L-glutamine (2 mM), penicillin (100 U/ml), and streptomycin (100 μ g/ml) (Thermo Fisher Scientific). U2OS Flp-In T-REx cell lines were maintained in DMEM containing 10% fetal bovine serum, L-glutamine, penicillin, streptomycin and blasticidin (5 μ g/ml) (Invitrogen). All cell lines were cultured in humidified incubators at 37 °C with 5% CO₂. Treatments were performed with hydroxyurea (4 mM, Merck), the MRE11 inhibitor mirin (25 μ M, Merck) or the DNA2-specific inhibitor C5 (25 μ M, AOBIOUS) for 5 h. For SILAC labeling, HeLa cells were cultured for at least 5 passages in SILAC DMEM (Invitrogen)

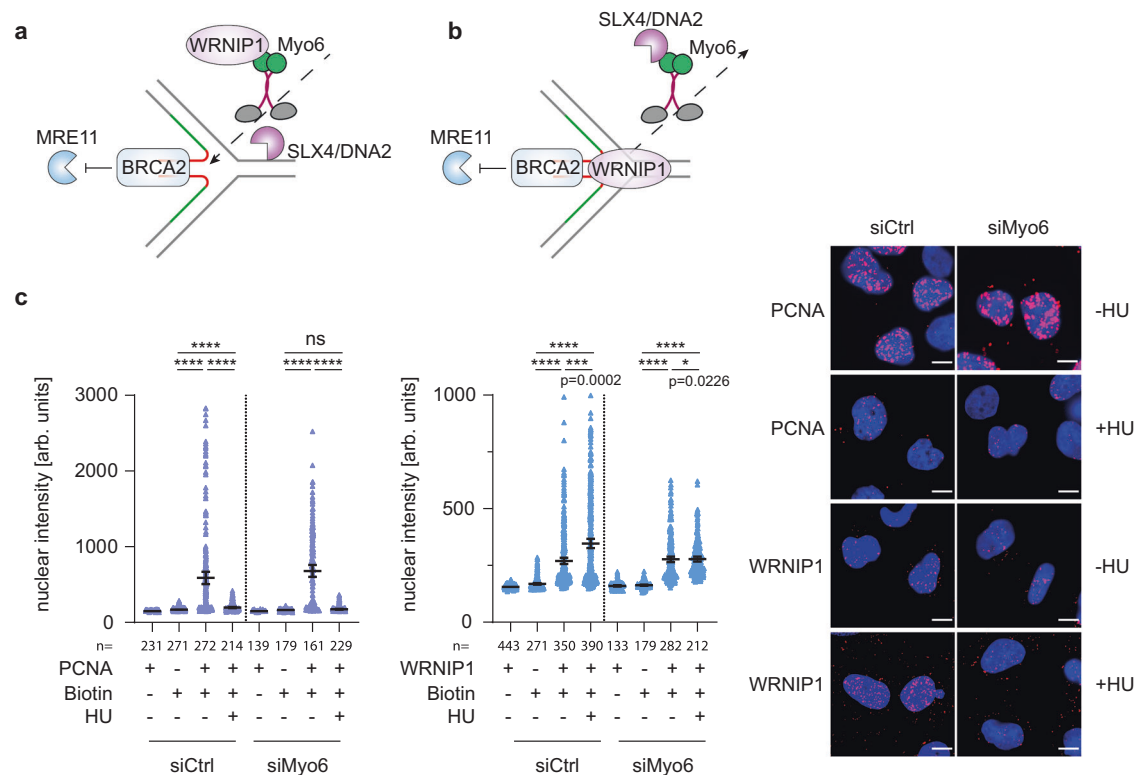


Fig. 5 | Myosin VI is required for efficient localization of WRNIP1 to stalled forks. **a, b** Models of how myosin VI could mediate fork protection in its role as a motor protein. **c** Myosin VI depletion interferes with efficient fork localization of WRNIP1. U2OS cells were siRNA-transfected, followed by SIF assays as indicated. Left: dot plots of PLA signal intensities with mean values \pm 95% confidence intervals. Significance levels were calculated using the two-tailed Mann-Whitney

test from indicated number of nuclei per sample (ns, non-significant, ****: $p < 0.0001$, ***: $p < 0.001$, *: $p < 0.05$) and annotated for $p > 0.0001$. Right: representative images, Hoechst (blue), PLA (magenta), scale bar = 10 μ m. A representative experiment from three independent replicates is shown. Knockdown efficiency is shown in Supplementary Fig. 6. Source data are provided as a Source Data file.

supplemented with dialyzed FBS (Invitrogen) and containing either L-arginine and L-lysine (Merck) or L-arginine [13C6] and L-lysine [2H4] (Cambridge Isotope Laboratories).

Transfections

For overexpression purposes, HEK293T were transfected using polyethyleneimine (PEI) (Polysciences). Other cell types were transfected using Fugene HD (Promega) or Lipofectamine 2000 (Life technologies) according to the manufacturer's instructions. All expression constructs used in this study are listed in Supplementary Table 1.

For knockdowns, cells were transfected with siRNAs using Lipofectamine RNAiMAX (Life Technologies) according to the manufacturer's instructions at a final RNA concentration of 20 nM for 72 h. Knockdown of myosin VI was achieved with a pool of 4 different siRNAs (Hs_MYO6_5 FlexiTube siRNA, Hs_MYO6_7 FlexiTube siRNA, Hs_MYO6_8 FlexiTube siRNA and Hs_MYO6_10 FlexiTube, Qiagen). For rescue experiments in the U2OS Flp-In cell line expressing GFP-myosin VI, a single siRNA targeting the 3'-UTR of the myosin VI transcript (Hs_MYO6_10 FlexiTube siRNA) was used. RAD51 and ZRANB3 knockdowns were performed using a pool of two independent siRNAs each. A list of all siRNAs used in this study can be found in Supplementary Table 3.

Generation of stable cell lines

U2OS Flp-In T-REX cell lines for DOX-inducible expression were generated by co-transfection of the respective pDEST-FRT-TO construct with the pOG44 Flp-Recombinase (Supplementary Table 1). 24 h post-transfection, cells were selected with 100 μ g/ml hygromycin (InvivoGen) for 10 days. Hygromycin-resistant cells were sorted for GFP-positive clones using a BD FACS Aria III SORP instrument. Single-cell

clones were tested for construct expression and myosin VI depletion after DOX treatment by western blotting using GFP- and myosin VI-specific antibodies (Supplementary Table 2).

Generation of plasmids

Fragments were inserted via restriction/ligation cloning or following PCR amplification with specific oligonucleotides, listed in Supplementary Table 4. For Gateway cloning, Gateway[®] LR Clonase[®] II enzyme mix (Thermo Fisher Scientific) was used according to the manufacturer's instructions. Detailed information about individual constructs will be provided upon request.

Site-directed mutagenesis

Site-directed mutagenesis was performed using Pfu Turbo DNA Polymerase (Agilent). The amplification product was digested with DpnI (New England Biolabs), *E. coli* TOP10 cells were transformed with the construct followed by sequence verification. Oligonucleotides for mutagenesis are listed in Supplementary Table 4.

Protein production and purification

GST fusion proteins were produced in *E. coli* BL21 (DE3) cells at 37 $^{\circ}$ C for 4 h after induction with 1 mM IPTG (Generon) at an OD₆₀₀ of 0.8. Cells were pelleted and lysed by sonication in PBS/0.1% Triton X-100 (Merck) supplemented with protease inhibitor cocktail (SIGMAFAST). Clarified supernatants were incubated with 1 ml of GSH-Sepharose beads (Cytiva) per liter of bacterial culture. After 2 h at 4 $^{\circ}$ C, the beads were washed with PBS/0.1% Triton X-100 and maintained in storage buffer (50 mM Tris, pH 7.4, 100 mM NaCl, 1 mM EDTA, 1 mM DTT, and 10% glycerol).

Expression of DARPins with N-terminal MRGS(H)₈ tag, USP2cc with N-terminal MRGS(H)₈ tag, myosin VI (aa 992-1122) with N-terminal

MRGS(H)₈ and C-terminal Avi tag in *E. coli* BL21 (DE3) was induced with 1 mM IPTG for 20 h at 18 °C. Cells were resuspended in buffer A (50 mM Tris-HCl pH 7.4, 250 mM NaCl, 10% glycerol, 1 mM DTT, 20 mM imidazole) and lysed by sonication. The clarified supernatant was subjected to affinity chromatography on Ni-NTA resin (Qiagen), and eluted protein was rebuffed using PD 10 columns (Cytiva) in storage buffer (50 mM Tris, pH 7.4, 100 mM NaCl, 1 mM EDTA, 1 mM DTT, and 10% glycerol).

Myosin VI (aa 992-1122) with N-terminal MRGS(H)₈ and C-terminal Avi tag was biotinylated *in vivo* by co-expressing biotin-ligase BirA (pBirAcm from Avidity) in *E. coli* BL21 (DE3). 50 μM biotin was added to the growth medium (LB) before induction with IPTG.

GST-pulldown assay coupled to mass spectrometry

For SILAC experiments, 8 × 10⁷ HeLa cells were lysed in 2 ml JS buffer (100 mM HEPES pH 7.5, 50 mM NaCl, 5% glycerol, 1% Triton X-100, 2 mM MgCl₂, 5 mM EGTA, 1 mM DTT), supplemented with protease inhibitor cocktail (SIGMAFAST) and Benzomase® (Merck). 50 μg of GST and 70 μg of GST-MyUb fusion protein immobilized on 50 μl GSH-Sepharose beads were incubated with 1 ml of cellular lysate for 2 h at 4 °C. Beads were washed five times in 1 ml JS buffer. Labels were switched in 2 out of 4 biological replicates. SILAC samples were pooled during the last wash. Bound proteins were eluted in 2× NuPAGE LDS Sample Buffer (Life Technologies) supplemented with 1 mM dithiothreitol, heated at 70 °C for 10 min, alkylated by addition of 5.5 mM chloroacetamide for 30 min, and separated by SDS-PAGE on a 4–12% gradient Bis-Tris gel (Invitrogen). Proteins were stained using the Colloidal Blue Staining Kit (Life Technologies) and digested *in-gel* using 0.6 μg of MS-approved trypsin (Serva) per gel fraction. Peptides were extracted from the gel and desalted using reversed-phase C18 StageTips.

Peptide fractions were analyzed on a quadrupole Orbitrap mass spectrometer (Q Exactive Plus, Thermo Fisher Scientific) equipped with a UHPLC system (EASY-nLC 1000, Thermo Fisher Scientific). Peptide samples were loaded onto C18 reversed-phase columns (25 cm length, 75 μm inner diameter, 1.9 μm bead size, packed *in-house*) and eluted with a linear gradient from 1.6 to 52% acetonitrile containing 0.1% formic acid in 90 min. The mass spectrometer was operated in a data-dependent mode, automatically switching between MS and MS2 acquisition. Survey full scan MS spectra (*m/z* 300–1,650, resolution: 70,000, target value: 3e6, maximum injection time: 20 ms) were acquired in the Orbitrap. The 10 most intense ions were sequentially isolated, fragmented by higher energy C-trap dissociation (HCD) and scanned in the Orbitrap mass analyzer (resolution: 35,000, target value: 1e5, maximum injection time: 120 ms, isolation window: 2.6 *m/z*). Precursor ions with unassigned charge states, as well as with charge states of +1 or higher than +7, were excluded from fragmentation. Precursor ions already selected for fragmentation were dynamically excluded for 20 s.

Raw data files were analyzed using MaxQuant (version 1.5.2.8)⁴². Parent ion and MS2 spectra were searched against a reference proteome database containing human protein sequences obtained from UniProtKB (HUMAN_2016_05) using the Andromeda search engine⁴³. Spectra were searched with a mass tolerance of 4.5 ppm in MS mode, 20 ppm in HCD MS2 mode, strict trypsin specificity, and allowing up to two mis-cleavages. Cysteine carbamidomethylation was searched as a fixed modification, whereas protein N-terminal acetylation, methionine oxidation, GlyGly (K), and N-ethylmaleimide modification of cysteines (mass difference to cysteine carbamidomethylation) were searched as variable modifications. The Re-quantify option was turned on. The dataset was filtered based on posterior error probability (PEP) to arrive at a false discovery rate of below 1%, estimated using a target-decoy approach⁴⁴. Statistical analysis and MS data visualization were performed using the R software environment (version 4.2.1). Potential contaminants, reverse hits, hits only identified by site and hits with no unique peptides were excluded from the analysis. Statistical significance was calculated using a moderated *t*-test (limma package)⁴⁵.

GO term analysis (biological process) was performed using EnrichR⁴⁶. Visualized GO terms were selected based on adjusted *p* value, odds ratio and semantic uniqueness. To determine the number of nuclear proteins among MyUb interactors (fold change > 2, FDR < 0.05), GO cellular component annotations were retrieved from the STRING network tool⁴⁷.

Preparation of unanchored K63-linked polyubiquitin chains

Unanchored K63-linked polyubiquitin chains were prepared by incubating 0.05 μM E1 (^{His}Uba1), 2 μM ^{His}Ubc13-Mms2 and 0.5 μM E3 (Pib1RING+100aa)⁴⁸ in a 1 ml reaction containing 40 mM HEPES, pH 7.4, 8 mM magnesium acetate, 50 mM NaCl and 30 μM ATP. *Wildtype* ubiquitin (purified bovine ubiquitin, Sigma) was used at a concentration of 8 μM and 4 μM of ubiquitin mutant K63R was added for capping of the chains. The reaction was incubated for 1.5 h at 30 °C and 1–4 μl of the chain reaction were used in GST-pulldown assays.

GST-pulldown assays

GST-pulldown assays were performed with lysates from 5 × 10⁶ unlabeled HeLa cells, and interactors were detected by western blotting using antibodies against endogenous proteins.

To identify DARPins suitable for pulldown assays, screening was performed by incubating 10 μg GST (as control) or 14 μg GST-MyUb immobilized on 20 μl GSH-Sepharose beads with a final DARPIn concentration of 1 μM in 200 μl PBS/0.1% Triton X-100. Beads were washed three times in 1 ml PBS/0.1% Triton X-100, boiled for 10 min in NuPAGE® LDS Sample Buffer and subjected to SDS-PAGE. Detection was performed using Instant Blue protein stain (Biozol).

To identify direct protein-protein interactions, we performed pulldown assays by incubating 5 μg GST or GST-WRNIP1 immobilized on 20 μl GSH-Sepharose beads with various concentrations of His-MIUMyub domain in 200 μl modified JS buffer (100 mM HEPES pH 7.5, 50 mM NaCl, 5% glycerol, 1% Triton X-100, 2 mM MgCl₂, 5 mM EGTA, 1 mM DTT). Beads were washed three times in 1 ml modified JS-buffer, boiled for 10 min in NuPAGE® LDS Sample Buffer and subjected to SDS-PAGE and subjected to western blotting.

Immunoprecipitation of GFP-tagged proteins

HEK293T cells were PEI-transfected with the respective plasmid (Supplementary Table 1) for 24 h, followed by lysis in JS buffer (100 mM HEPES pH 7.5, 50 mM NaCl, 5% glycerol, 1% Triton X-100, 2 mM MgCl₂, 5 mM EGTA, 1 mM DTT) supplemented with protease inhibitor cocktail (SIGMAFAST) and Benzomase®. Cell lysates were cleared by centrifugation for 30 min at 4 °C and incubated with GFP-trap magnetic agarose beads (Chromotek) for 1 h at 4 °C. After 3 washes with JS buffer, beads were boiled for 10 min in NuPAGE® LDS Sample Buffer and subjected to western blotting.

Proteasome inhibition

U2OS Flp-In T-REx cells harboring DOX-inducible GFP-M6G4-2RING (2R#8) were treated with 5 μM MG-132 (Enzo Life Sciences) for 24 h in the presence of 2 μg/ml DOX.

iPOND

U2OS cells were labeled with 10 μM EdU (Merck) for 30 min. Subsequently, cells were fixed with 1% formaldehyde (Merck) for 10 min, followed by quenching with 125 mM glycine (Merck) for 10 min. After two washing steps with PBS/1% BSA, cells were collected by scraping, followed by permeabilization in PBS/0.1% Triton X-100. Subsequently, cells were washed with PBS/1% BSA and subjected to the Click-iT reaction in a solution containing 10 mM sodium ascorbate (Merck), 0.1 mM azide-PEG₃-biotin conjugate (Merck) and 2 mM copper sulfate (Merck) for 30 min at room temperature. Cells were then washed twice in PBS/1% BSA, lysed in 10 mM Tris-HCl pH 8.0, 140 mM NaCl, 1% Triton X-100, 0.1% sodium deoxycholate, 0.1% SDS, supplemented with

SIGMAFAST protease inhibitor cocktail, and sonicated using a Bioruptor (Diagenode). Lysates were cleared by centrifugation for 45 min at 4 °C in a table-top centrifuge and subjected to streptavidin-agarose beads (Thermo Fisher Scientific) overnight at 4 °C. The next day, beads were washed five times in PBS/1% BSA and de-crosslinking was carried out for 30 min in NuPAGE[®] LDS Sample Buffer at 95 °C. For protein detection, samples were subjected to SDS-PAGE and immunoblotted with relevant antibodies (Supplementary Table 2).

Immunofluorescence

For immunofluorescence analysis, cells were fixed with 4% paraformaldehyde (Merck) for 10 min, permeabilized for 5 min at room temperature with 0.1% Triton X-100 and incubated for 1 h in PBS/3% BSA. Subsequently, cells were incubated with primary antibodies for 1 h (α -myosin VI α -rabbit in a 1:400 dilution), followed by 3 \times 5 min washing steps with PBS/0.1% Triton X-100 and incubation with secondary antibodies for 30 min at room temperature. Coverslips were mounted with ProLong[™] Diamond Antifade Mountant (Thermo Fisher Scientific). Images were acquired using the Leica Application Suite X version 3.7.5.24914 on a Leica AF-7000 widefield microscope and analyzed with ImageJ 153t.

Confocal microscopy

For confocal microscopy, U2OS cells were seeded in μ -Slide 8 Well Chamber Slides (Ibidi) with a confluency of 80% (5×10^4 cells per well). To visualize actin filaments, cells were fixed in 4% paraformaldehyde for 10 min at room temperature and permeabilized using 0.3% Triton-X for 10 min. For F-actin stainings, cells were incubated with Alexa Fluor 647 Phalloidin (1:100) (Fisher Scientific) and Hoechst (1:10,000) (Merck) in PBS for 1 h, followed by three washing steps of 5 min each with PBS. Samples were imaged using the Fusion 1.1.0.1 software on a BC43 Spinning Disk Confocal (Oxford Instruments) microscope using blue (405 nm), green (488 nm) and red (612 nm) excitation wavelengths. A 60 \times oil objective lens was chosen. Z-stack imaging was performed with 30–40 steps in 0.3 μ m (Phalloidin) or 0.4 μ m increments (GFP-myosin VI) and a z-plane between #8 and #17 was chosen for nuclear actin quantification using Fiji ImageJ 153t software.

Immunoblotting

Samples were separated via SDS-PAGE and transferred to nitrocellulose membranes using the Trans-Blot Turbo[®] system (Bio Rad). Membranes were blocked for 1 h at room temperature in 5% milk/PBS/0.1% TWEEN-20 and incubated with primary antibodies in a 1:1000 dilution in PBS/0.1% TWEEN-20/1% BSA; either for 1 h at room temperature or overnight at 4 °C. Afterwards, membranes were washed with PBS/0.1% TWEEN-20 and incubated with secondary antibodies for 1 h at room temperature. Detection was performed by enhanced chemiluminescence using a Fusion FX (Vilber Lourmat) instrument with the Fusion Capt Advance Fx7 17.03 software after incubation with HRP-coupled secondary antibodies or by direct fluorescence using an Odyssey Clx imaging system (LI-COR) with the Image Studio version 3.1 software after incubation with secondary antibodies coupled to a fluorescent dye (Supplementary Table 2). Uncropped images from the main figures can be found in the ‘Source Data’ file provided with this paper.

Fiber assays

U2OS cells were labeled with 50 μ M CldU (Merck) for 20 min and 50 μ M IdU (Merck) for 20 min, respectively. Cells were trypsinized, resuspended in PBS and diluted to 1.75×10^5 cells/ml. Labeled cells were mixed with unlabeled cells at a ratio of 1:1. Lysis of the cells was carried out directly on microscopy slides, where 4 μ l of the cells was mixed with 7.5 μ l of lysis buffer (200 mM Tris-HCl pH 7.4, 50 mM EDTA, 0.5% SDS). After 9 min, the slides were tilted at an angle of 15–45° and the DNA fibers were stretched on the slides. The fibers were fixed in methanol/acetic acid (3:1) overnight at 4 °C. Following fixation,

the DNA fibers were denatured in 2.5 M HCl for 1 h, washed with PBS and blocked with PBS/0.1% TWEEN-20/2% BSA for 40 min. The fibers were incubated with primary antibodies against CldU (Rat monoclonal anti-BrdU (clone BUI/75 (ICR1), Abcam) and IdU (Mouse monoclonal anti-BrdU (clone B44), BD Biosciences) (1:50 dilution) for 2.5 h, washed with PBS/0.1% TWEEN-20 and incubated with secondary antibodies labeled with Alexa Fluor 488 and Alexa Fluor 647 (1:100 dilution). The slides were mounted in ProLong[™] Diamond Antifade Mountant. Images of the DNA fibers were acquired using a Leica Thunder widefield microscope and analysis was carried out using Fiji ImageJ 153t. To assess overall replication speed, only fibers where both tracks had equal length were measured. To assess fork asymmetry (IdU/CldU ratio), also fibers with shorter IdU tracks were analyzed and analyzed using GraphPad Prism 8.4.0 (538).

Proximity ligation assays (PLA)

U2OS cells were seeded on coverslips with a confluency of 80%. Afterwards, cells were fixed in 4% paraformaldehyde for 10 min and permeabilized in 0.3% Triton X-100 for 10 min. PLA was then carried out using the Duolink[®] In Situ Red starter kit (Merck) according to the manufacturer’s instructions. Primary antibodies were used in a 1:100 dilution (α -WRNIP1 α -rabbit, α -Myosin VI α -mouse). In addition, Hoechst staining was included prior to mounting coverslips in ProLong[™] Diamond Antifade Mountant. Images were acquired using a Leica Thunder widefield microscope and analysis was carried out using Fiji ImageJ 153t.

In situ analysis of protein interactions at DNA replication forks (SIRF)

For SIRF, cells were pulsed with 10 μ M EdU for 10 min and then left untreated or treated with 4 mM HU for 5 h. After fixation in 4% paraformaldehyde for 10 min and permeabilization in 0.3% Triton X-100 for 10 min, the Click-iT reaction was performed for 1 h at room temperature in PBS containing 2 mM copper sulfate, 10 μ M azide-PEG₃-biotin conjugate and 100 mM sodium ascorbate. PLA was then carried out as described above. Primary antibodies were used in a 1:100 (α -WRNIP1 α -rabbit, α -Myosin VI α -mouse, α -Biotin α -mouse) or 1:1000 dilution (α -PCNA, α -rabbit).

DARPin selection and initial screening

To generate myosin VI-specific DARPins, biotinylated myosin VI (aa 992-1122) isoform 1 with N-terminal MRGS(H)₈ and C-terminal Avi tag (³⁵myosin VI (aa 992-1122)^{Avi}) was immobilized on either MyOne T1 streptavidin-coated beads (Pierce) or Sera-Mag neutravidin-coated beads (GE Healthcare). The use of the type of beads was alternated during selection rounds. Ribosome display selections were performed essentially as described⁴⁹, using a semi-automatic KingFisher Flex MTP 96-well platform. Although DARPin-screening was performed to isolate isoform 1-specific binders, DARPin (M6G4), which showed a biological effect, was characterized as pan-isoform-specific (Supplementary Fig. 4c).

The library includes N3C DARPins, consisting of three internal and randomized ankyrin repeats as described earlier³⁸. The originally described C-cap was replaced with a C-cap showing better stability toward unfolding implementing mutations in 5 amino acid positions^{36,50,51} to facilitate downstream experiments like protein fusions. Additionally, we introduced a second randomization strategy in the N- and C-cap as described^{36,52} to also allow interaction of the capping repeats with the target. The libraries of DARPins with randomized and non-randomized N- and C- terminal caps, both containing randomized internal repeats and a stabilized C-cap, were mixed in a 1:1 stoichiometry to increase diversity. Successively enriched DARPin pools were cloned as intermediates in a ribosome display vector⁵². Selections were performed over four rounds with decreasing target concentration and increasing washing steps to enrich for binders with

slow off-rates and thus high affinities. The first round accomplished the initial selection against myosin VI at low stringency. The second round included pre-panning with the undesired myosin VI isoforms 2 (aa 992-1099) and 3 (aa 992-1131) immobilized on magnetic beads, with the supernatant transferred to the immobilized desired target myosin VI isoform 1. The third round included this pre-panning and the addition of non-biotinylated myosin VI isoform 1 to enrich for binders with slow off-rates. The fourth and final round included the pre-panning step and selection was performed with low stringency to collect all binders.

The final enriched pool was cloned as fusion construct with an N-terminal MRGS(H)₈ tag and C-terminal FLAG tag via unique BamHI and HindIII sites into a bacterial pQE30 derivative vector containing lacI^q for expression control. After transformation of *E. coli* XLI-blue, 380 single DARPins clones were expressed in 96-well format and cells were lysed by addition of B-Per Direct detergent plus lysozyme and nuclease (Pierce). The resulting bacterial crude extracts of single DARPins clones were subsequently used in a Homogeneous Time Resolved Fluorescence (HTRF)-based screen to identify potential binders. The clone M6G4 that was selected for downstream applications was monoclonalized, by cutting the DARPins ORF, re-ligating it in fresh vector, retransformation and sequence verification. Binding of the FLAG-tagged DARPins to streptavidin-immobilized biotinylated His⁶-Avi¹-myosin VI (aa 992-1122) was measured using FRET (donor: Streptavidin-Tb cryptate (610SATLB, Cisbio), acceptor: mAb anti FLAG M2-d2 (61FG2DLB, Cisbio)). Further HTRF measurement against 'No Target' allowed for discrimination of myosin VI isoform 1-specific hits. Experiments were performed at room temperature in white 384-well Optiplate plates (PerkinElmer) using the Taglite assay buffer (Cisbio) at a final volume of 20 µl per well. FRET signals were recorded after an incubation time of 30 min using a Varioskan LUX Multimode Microplate (Thermo Fisher Scientific). HTRF ratios were obtained by dividing the acceptor signal (665 nm) by the donor signal (620 nm) and multiplying this value by 10,000 to derive the 665/620 ratio. The background signal was determined by using reagents in the absence of DARPins.

Surface plasmon resonance

Surface plasmon resonance (SPR) experiments were performed on a Biacore X100 system, equilibrated at 25 °C in HBS-EP buffer (10 mM HEPES pH 7.4, 150 mM NaCl, 3 mM EDTA, 0.005% v/v Surfactant P20, Cytiva) using a streptavidin-coated sensor chip (CAP) and biotinylated MIUMyUb-domain as immobilized target with a density of 60-80 RU. The Biacore X100 Control Software version 2.0.2 was used for data acquisition and the Biacore X100 Evaluation version 2.0.2 for data analysis. DARPins were injected for 180 s at a flow rate of 30 µl/min in increasing concentrations (factor 1.5) ranging from 6.5 nM to 0.25 µM. Kinetic data (K_D , k_{on} and k_{off}) for the M6G4 DARPins were obtained using the fitting tool (1:1 binding model) of the Biacore X100 evaluation software version 2.0.2 and are reported as the mean of four independent experiments with corresponding standard deviations. The control DARPins (E3_5) did not show any binding to the biotinylated MIUMyUb-domain in our measurements.

Reporting summary

Further information on research design is available in the Nature Portfolio Reporting Summary linked to this article.

Data availability

All reagents used in the paper are listed in Supplementary Table 5. Parent ion and MS2 spectra were searched against a reference proteome database containing human protein sequences obtained from UniProtKB (HUMAN_2016_05) using the Andromeda search engine. The mass spectrometry-based proteomics data have been deposited to the ProteomeXchange consortium via the PRIDE partner repository⁵³ with the data set identifier [PXD035394](https://doi.org/10.1038/s41467-023-39517-y). Source data are provided with this paper.

Code availability

Custom codes used for the preparation of volcano and GO term plots as well as the Image J-based quantifications are available on GitHub [<https://github.com/helle-ulrich-lab/myosinVI-replication-fork-stability>].

References

- Neelsen, K. J. & Lopes, M. Replication fork reversal in eukaryotes: from dead end to dynamic response. *Nat. Rev. Mol. Cell Biol.* **16**, 207–220 (2015).
- Bhat, K. P. & Cortez, D. RPA and RAD51: fork reversal, fork protection, and genome stability. *Nat. Struct. Mol. Biol.* **25**, 446–453 (2018).
- Tagliatala, A. et al. Restoration of Replication Fork Stability in BRCA1- and BRCA2-Deficient Cells by Inactivation of SNF2-Family Fork Remodelers. *Mol. Cell* **68**, 414–430.e418 (2017).
- Vujanovic, M. et al. Replication Fork Slowing and Reversal upon DNA Damage Require PCNA Polyubiquitination and ZRANB3 DNA Translocase Activity. *Mol. Cell* **67**, 882–890.e885 (2017).
- Bai, G. et al. HLTF Promotes Fork Reversal, Limiting Replication Stress Resistance and Preventing Multiple Mechanisms of Unrestrained DNA Synthesis. *Mol. Cell* **78**, 1237–1251.e1237 (2020).
- Lemacon, D. et al. A. MRE11 and EXO1 nucleases degrade reversed forks and elicit MUS81-dependent fork rescue in BRCA2-deficient cells. *Nat. Commun.* **8**, 860 (2017).
- Hurst, V., Shimada, K. & Gasser, S. M. Nuclear Actin and Actin-Binding Proteins in DNA Repair. *Trends Cell Biol.* **29**, 462–476 (2019).
- Caridi, C. P., Plessner, M., Grosse, R. & Chiolo, I. Nuclear actin filaments in DNA repair dynamics. *Nat. Cell Biol.* **21**, 1068–1077 (2019).
- Schrank, B. R. et al. Nuclear ARP2/3 drives DNA break clustering for homology-directed repair. *Nature* **559**, 61–66 (2018).
- Caridi, C. P. et al. Nuclear F-actin and myosins drive relocalization of heterochromatic breaks. *Nature* **559**, 54–60 (2018).
- Baarlink, C. et al. A transient pool of nuclear F-actin at mitotic exit controls chromatin organization. *Nat. Cell Biol.* **19**, 1389–1399 (2017).
- Parisis, N. et al. Initiation of DNA replication requires actin dynamics and formin activity. *EMBO J.* **36**, 3212–3231 (2017).
- Aymard, F. et al. Genome-wide mapping of long-range contacts unveils clustering of DNA double-strand breaks at damaged active genes. *Nat. Struct. Mol. Biol.* **24**, 353–361 (2017).
- Lamm, N. et al. Nuclear F-actin counteracts nuclear deformation and promotes fork repair during replication stress. *Nat. Cell Biol.* **22**, 1460–1470 (2020).
- Maly, I. V. & Hofmann, W. A. Myosins in the Nucleus. *Adv. Exp. Med. Biol.* **1239**, 199–231 (2020).
- Wells, A. L. et al. Myosin VI is an actin-based motor that moves backwards. *Nature* **401**, 505–508 (1999).
- Vreugde, S. et al. Nuclear myosin VI enhances RNA polymerase II-dependent transcription. *Mol. Cell* **23**, 749–755 (2006).
- Fili, N. et al. NDP52 activates nuclear myosin VI to enhance RNA polymerase II transcription. *Nat. Commun.* **8**, 1871 (2017).
- Hari-Gupta, Y. et al. Myosin VI regulates the spatial organisation of mammalian transcription initiation. *Nat. Commun.* **13**, 1346 (2022).
- He, F. et al. Myosin VI Contains a Compact Structural Motif that Binds to Ubiquitin Chains. *Cell Rep.* **14**, 2683–2694 (2016).
- Porebski, B. et al. WRNIP1 Protects Reversed DNA Replication Forks from SLX4-Dependent Nucleolytic Cleavage. *iScience* **21**, 31–41 (2019).
- Leuzzi, G., Marabitti, V., Pichierri, P. & Franchitto, A. WRNIP1 protects stalled forks from degradation and promotes fork restart after replication stress. *EMBO J.* **35**, 1437–1451 (2016).
- Schlacher, K. et al. Double-strand break repair-independent role for BRCA2 in blocking stalled replication fork degradation by MRE11. *Cell* **145**, 529–542 (2011).
- Penengo, L. et al. Crystal structure of the ubiquitin binding domains of rabex-5 reveals two modes of interaction with ubiquitin. *Cell* **124**, 1183–1195 (2006).

25. Spudich, G. et al. Myosin VI targeting to clathrin-coated structures and dimerization is mediated by binding to Disabled-2 and PtdIns(4,5)P₂. *Nat. Cell Biol.* **9**, 176–183 (2007).
26. Dungrawala, H. & Cortez, D. Purification of proteins on newly synthesized DNA using iPOND. *Methods Mol. Biol.* **1228**, 123–131 (2015).
27. Sirbu, B. M. et al. Identification of proteins at active, stalled, and collapsed replication forks using isolation of proteins on nascent DNA (iPOND) coupled with mass spectrometry. *J. Biol. Chem.* **288**, 31458–31467 (2013).
28. Roy, S., Luzwick, J. W. & Schlacher, K. SIRF: Quantitative in situ analysis of protein interactions at DNA replication forks. *J. Cell Biol.* **217**, 1521–1536 (2018).
29. Bish, R. A. & Myers, M. P. Werner helicase-interacting protein 1 binds polyubiquitin via its zinc finger domain. *J. Biol. Chem.* **282**, 23184–23193 (2007).
30. Baker, R. T. et al. Using deubiquitylating enzymes as research tools. *Methods Enzymol.* **398**, 540–554 (2005).
31. Plessner, M., Melak, M., Chinchilla, P., Baarlink, C. & Grosse, R. Nuclear F-actin formation and reorganization upon cell spreading. *J. Biol. Chem.* **290**, 11209–11216 (2015).
32. Olave, I. A., Reck-Peterson, S. L. & Crabtree, G. R. Nuclear actin and actin-related proteins in chromatin remodeling. *Annu. Rev. Biochem.* **71**, 755–781 (2002).
33. Hofmann, W. A. et al. Actin is part of pre-initiation complexes and is necessary for transcription by RNA polymerase II. *Nat. Cell Biol.* **6**, 1094–1101 (2004).
34. Hu, P., Wu, S. & Hernandez, N. A role for beta-actin in RNA polymerase III transcription. *Genes Dev.* **18**, 3010–3015 (2004).
35. Philimonenko, V. V. et al. Nuclear actin and myosin I are required for RNA polymerase I transcription. *Nat. Cell Biol.* **6**, 1165–1172 (2004).
36. Plückthun, A. Designed ankyrin repeat proteins (DARPs): binding proteins for research, diagnostics, and therapy. *Annu. Rev. Pharm. Toxicol.* **55**, 489–511 (2015).
37. Binz, H. K. et al. High-affinity binders selected from designed ankyrin repeat protein libraries. *Nat. Biotechnol.* **22**, 575–582 (2004).
38. Binz, H. K., Stumpp, M. T., Forrer, P., Amstutz, P. & Plückthun, A. Designing repeat proteins: well-expressed, soluble and stable proteins from combinatorial libraries of consensus ankyrin repeat proteins. *J. Mol. Biol.* **332**, 489–503 (2003).
39. Ibrahim, A. F. M. et al. Antibody RING-Mediated Destruction of Endogenous Proteins. *Mol. Cell* **79**, 155–166 e159 (2020).
40. Magistrati, E. & Polo, S. Myomics: myosin VI structural and functional plasticity. *Curr. Opin. Struct. Biol.* **67**, 33–40 (2021).
41. Han, S. S. et al. WASp modulates RPA function on single-stranded DNA in response to replication stress and DNA damage. *Nat. Commun.* **13**, 3743 (2022).
42. Cox, J. & Mann, M. MaxQuant enables high peptide identification rates, individualized p.p.b.-range mass accuracies and proteome-wide protein quantification. *Nat. Biotechnol.* **26**, 1367–1372 (2008).
43. Cox, J. et al. Andromeda: a peptide search engine integrated into the MaxQuant environment. *J. Proteome Res.* **10**, 1794–1805 (2011).
44. Elias, J. E. & Gygi, S. P. Target-decoy search strategy for increased confidence in large-scale protein identifications by mass spectrometry. *Nat. Methods* **4**, 207–214 (2007).
45. Ritchie, M. E. et al. limma powers differential expression analyses for RNA-sequencing and microarray studies. *Nucleic Acids Res.* **43**, e47 (2015).
46. Kuleshov, M. V. et al. Enrichr: a comprehensive gene set enrichment analysis web server 2016 update. *Nucleic Acids Res.* **44**, W90–W97 (2016).
47. Szklarczyk, D. et al. STRING v11: protein-protein association networks with increased coverage, supporting functional discovery in genome-wide experimental datasets. *Nucleic Acids Res.* **47**, D607–D613 (2019).
48. Renz, C. et al. Ubc13-Mms2 cooperates with a family of RING E3 proteins in budding yeast membrane protein sorting. *J. Cell Sci.* **133**, jcs244566 (2020).
49. Dreier, B. & Plückthun, A. Rapid selection of high-affinity binders using ribosome display. *Methods Mol. Biol.* **805**, 261–286 (2012).
50. Kramer, M. A., Wetzel, S. K., Plückthun, A., Mittl, P. R. & Grütter, M. G. Structural determinants for improved stability of designed ankyrin repeat proteins with a redesigned C-capping module. *J. Mol. Biol.* **404**, 381–391 (2010).
51. Brauchle, M. et al. Protein interference applications in cellular and developmental biology using DARPins that recognize GFP and mCherry. *Biol. Open* **3**, 1252–1261 (2014).
52. Schilling, J., Schöppe, J. & Plückthun, A. From DARPins to Loop-DARPins: novel LoopDARPin design allows the selection of low picomolar binders in a single round of ribosome display. *J. Mol. Biol.* **426**, 691–721 (2014).
53. Vizcaino, J. A. et al. The PRoteomics IDentifications (PRIDE) database and associated tools: status in 2013. *Nucleic Acids Res.* **41**, D1063–D1069 (2013).

Acknowledgements

We thank Ronald Wong and Kirill Petriukov for scientific discussions and Katharina Schlacher, Lorenza Penengo and Massimo Lopes for help with setting up the fiber assay. We thank Ron Hay, Simona Polo, Lorenza Penengo and Christian Renz for sharing constructs, cell lines or recombinant proteins. We thank Thomas Reinberg, Sven Furler and Joana Marinho from HT-BSF UZH for their assistance in performing the ribosome display DARPin selection and screening. The IMB Core Facilities for Proteomics, Flow Cytometry, Microscopy and Protein Production are acknowledged for technical support and reagents. This work was funded by the Deutsche Forschungsgemeinschaft (DFG, German Research Foundation)—Project-ID 393547839—SFB 1361 awarded to H.D.U. and P.B., Project-ID BE 5342/2-1—FOR 2800 awarded to P.B. and Project-ID 408799149 awarded to H.P.W.

Author contributions

J.Sh., H.D.U., and H.P.W. conceived the study, J.Sh., V.A., K.H., S.M., T.S., and H.P.W. performed experiments and data analysis in cell and molecular biology, I.M., J.B.H., and P.B. performed mass spectrometry experiments and data analysis, J.Sc., B.D., and A.P. designed and supervised the DARPin selections, H.D.U. and H.P.W. wrote the paper and created the figures, and all authors discussed the data and provided input during paper preparation.

Competing interests

The authors declare no competing interests.

Additional information

Supplementary information The online version contains supplementary material available at <https://doi.org/10.1038/s41467-023-39517-y>.

Correspondence and requests for materials should be addressed to Helle D. Ulrich or Hans-Peter Wollscheid.

Peer review information *Nature Communications* thanks Said Salehe, Christopher Toseland and the other, anonymous, reviewer(s) for their contribution to the peer review of this work. A peer review file is available.

Reprints and permissions information is available at <http://www.nature.com/reprints>

Publisher's note Springer Nature remains neutral with regard to jurisdictional claims in published maps and institutional affiliations.

Open Access This article is licensed under a Creative Commons Attribution 4.0 International License, which permits use, sharing, adaptation, distribution and reproduction in any medium or format, as long as you give appropriate credit to the original author(s) and the source, provide a link to the Creative Commons license, and indicate if changes were made. The images or other third party material in this article are included in the article's Creative Commons license, unless indicated otherwise in a credit line to the material. If material is not included in the article's Creative Commons license and your intended use is not permitted by statutory regulation or exceeds the permitted use, you will need to obtain permission directly from the copyright holder. To view a copy of this license, visit <http://creativecommons.org/licenses/by/4.0/>.

© The Author(s) 2023